Chapter 3 – MAPPING

3.1 CREATING MAPS OF IONOSPHERIC ELECTRON DENSITY TO SUPPORT COMMUNICATION, SURVEILLANCE AND NAVIGATION SYSTEMS

(Cathryn Mitchell, Department of Electronic and Electrical Engineering, University of Bath, Bath, UK)

3.1.1 Introduction

Currently there are a number of different methods to produce estimates of the electron density in the ionosphere. Model-based approaches range from empirical models (e.g. IRI, Bilitza, 2001), through to methods that combine such models with real-time data (e.g. Bust et al., 2004) and finally approaches that constrain a physical model with measurements (e.g. Hajj et al., 2004). For well-instrumented regions of the Earth it is possible to design algorithms that use mathematical constraints and measurements to produce electron-density images without including ionospheric models (Spencer and Mitchell, 2001; Mitchell and Spencer, 2003). For global solutions of the electron density either model-assisted approaches or interpolation methods (e.g. solar-fixed persistence) are required to fill in large data-sparse regions of the Southern Hemisphere, in particular over the oceans.

This paper focuses on the development of the Multi-Instrument Data Analysis System (MIDAS) algorithm. Of all the approaches summarised above MIDAS is probably the most 'mathematical and data driven' and least 'model reliant'. This approach was taken in the development of MIDAS for a number of reasons. Firstly, it was apparent an early stage in the development (1999) that the number of available data sources for the ionosphere was increasing, mainly because of the increased use of GPS for scientific studies in other fields (mainly geodesy). In addition, it was also clear that much of the available data already being recorded was not being systematically utilized for ionospheric imaging (e.g. navigation data on low Earth orbit, LEO, satellites; Superdarn; ad-hoc HF links), either because of a lack of central collation or because of the required nonlinear inversion techniques had not yet been developed. Finally, the strength of minimising the model-reliance in the MIDAS approach is that in data-rich regions images that can show actual behaviour of the ionosphere at a given instant and not a 'merged' model-data solution. This also makes MIDAS a suitable technique for producing statistical results that could be used to produce new ionospheric models with improved ability match actual events.

In this paper the development of MIDAS is described. Examples of results for global and local ionospheric specification are given. Finally the future directions and required modifications to the technique for specific systems uses are discussed.

3.1.2 MIDAS Development

The MIDAS algorithms are based upon the oceanographic imaging techniques of Munk and Wunsch (1979); first applied to imaging 2D slices of the ionosphere by Fremouw et al. (1992). This was conventional tomographic imaging where the line integral data were approximated into a plane and inverted to reveal the electron density. MIDAS (version 1.0) is a linear inversion algorithm that can ingest any line-integral data such as GPS-ground or GPS-LEO differential-phase data (Yin et al. 2005) or inverted ionograms.

The development of the MIDAS algorithms was driven by the success of two-dimensional ionospheric tomography for both scientific and applications work (e.g. Mitchell et al., 1995; Mitchell et al., 1998 and Rogers et al., 2001). Initially it was thought that GPS data could only be used for simple constant altitude shell mapping and early work concentrated in this area. Comparisons between shell mapping and full 3-D imaging can be found in Meggs et al., 2004. In fact, the step from 2-D shell mapping to full 3-D imaging

is a matter of including mathematical concepts from tomography (Mitchell, 2002; Mitchell and Spencer, 2003). It was apparent that the differential phase-technique could only work with a time dependent algorithm, because the ionosphere changes while the satellite moves. Alternatively, pre-calibration of the differential code data could allow a time independent approach. Extensive simulation studies were used in the development of the techniques for the equatorial region (Materassi et al., 2005) and the mid-latitudes (Meggs et al., 2004). The imaging has recently been applied to the sparse-data region of South Africa (Cilliers et al., 2004).

The first stage of the MIDAS algorithm (Mitchell and Spencer, 2003) inversion is to set up a three-dimensional grid of voxels, each bounded in latitude, longitude and altitude, and to compute the length of each element of a satellite-to-receiver signal propagation path though each intersected voxel. The unknown electron concentration, $\mathbf{x_a}$, is defined to be constant within each voxel and contained in the column vector. The problem may now be expressed as:

$$\mathbf{y} = \tilde{\mathbf{H}}\mathbf{x_a}$$

where the matrix **H** transforms the electron density to the form and location of the observations and **y** are the observed TECs. It should be noted that the inversion uses relative differential phase observations. Thus appropriate lines of the matrix are differenced such that measurements along continuous satellite-receiver arcs are taken relative to a certain reference measurement within that arc.

The inversion cannot be performed directly so a mapping matrix, **X**, is used to transform the problem. This results in a situation where the unknowns are coefficients of orthonormal basis functions, the combination of which will give the final image of electron concentration. The basis functions (**X**) can be generated using a spherical harmonic expansion to represent the horizontal variation and empirical ortho-normal functions (EOFs) for the radial variation in electron concentration. The spherical harmonics provide a flexible basis to determine the horizontal distribution of ionization, which should be well defined by the measurements. The EOFs form a constraint to the vertical profile, only allowing a certain range of possible solutions. This is now expressed mathematically as:

$$\mathbf{y} = \tilde{\mathbf{H}}\tilde{\mathbf{X}}\tilde{\mathbf{W}}$$

where the matrix **X** contains the basis functions. **HX** now represents the set of TEC data that are formed by integration through the set of models. Applying singular value decomposition the inversion can be performed such that:

$$\tilde{\mathbf{W}} = (\tilde{\mathbf{H}}\tilde{\mathbf{X}})^{-1}\mathbf{y}$$

and the solution to the inverse problem is then given by:

$$\mathbf{x_a} = \tilde{\mathbf{W}}\tilde{\mathbf{X}}$$

The algorithm can be extended into a time-dependent inversion by incorporating a priori information about the evolution of the electron concentration during a specified period of time. Assuming that the change in electron concentration within a voxel with time is linear, then it is possible to write the same system of equations to solve for the change in the relative contributions of each basis function.

Recent developments to MIDAS have improved the ability to image in the data-sparse regions of the polar cap by incorporating a motion model into the imaging there. Specifically, a Kalman-filter approach is used to incorporate the Weimer model of the plasma convection into the imaging, thus allowing for the continuity of features as they move across data gaps (Spencer and Mitchell, 2007). It has also incorporated a new grid-rotation has been implemented that provides a solution to the problems caused to the imaging by convergence of the spherical coordinates at the pole.

3.1.3 Example Results from MIDAS

The date of the 30th October 2003 has been chosen to illustrate the imaging. All of the images are at 1800 UT. In the demonstrations here only ground-based GPS data are used, although other measurements from ionosondes and LEO satellites were available and could be incorporated into the MIDAS images if required. This major storm exhibited unusual features in the ionosphere and serves well to demonstrate the need for measurements rather than reliance on statistical models. In order to demonstrate this further the IRI model has been used to provide a comparison to the MIDAS images.

Figure 3-1 shows the locations of the receivers used for the example images. Figure 3-1a is for the Arctic region, Figure 3-1b and 3-1c for the whole Earth.

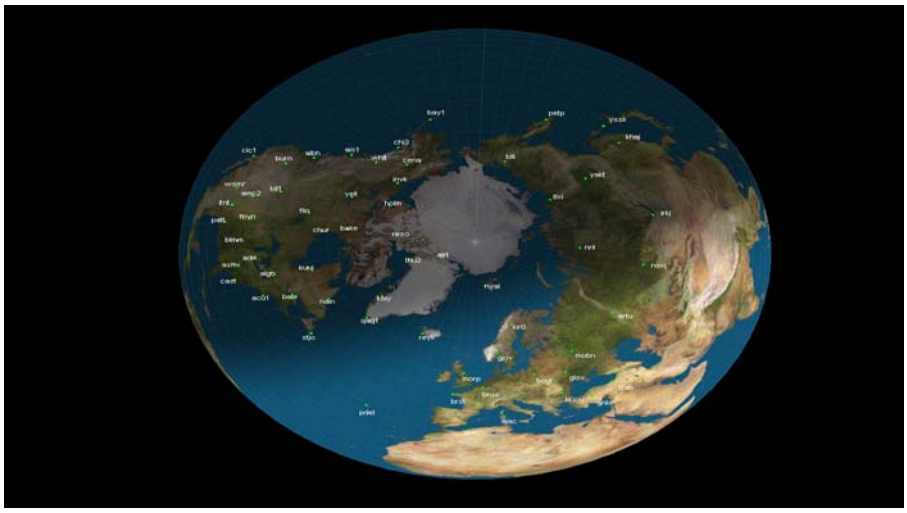

a

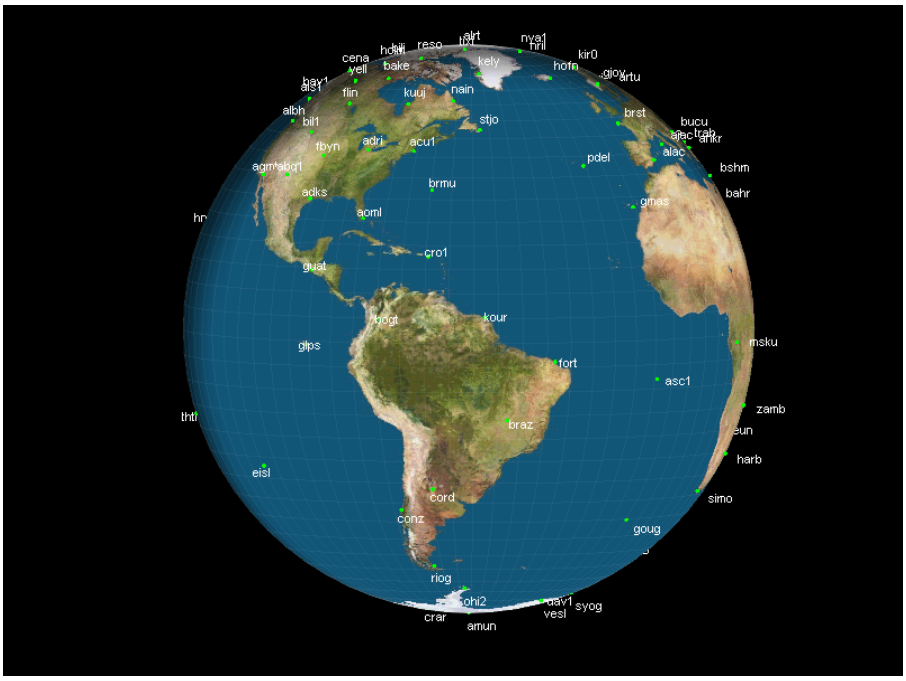

b

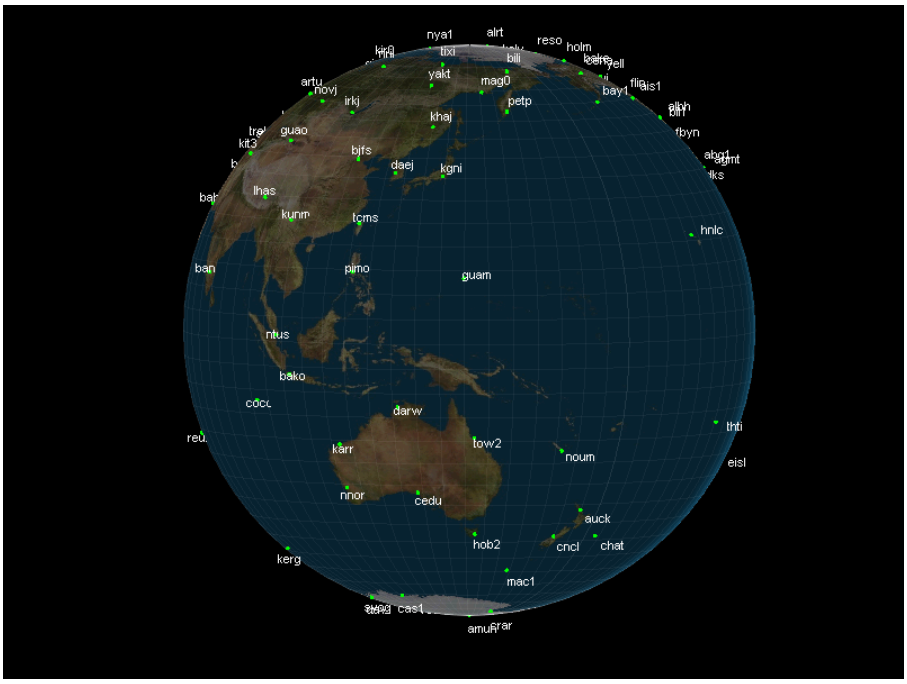

c

Figure 3-1: The Locations of the GPS Receivers Used for the Example Images.

Figure 3-2 shows the MIDAS images from the data coverage in Figure 3-1. The plots show isocontours of electron density (in contours from 2 to 12 $\times 10^{11}$ electrons per cubic metre) which allow a '3D' view of the ionosphere, revealing the altitude uplift and density enhancement regions simultaneously. Figure 3-3 shows a global view of the ionosphere from MIDAS (where the maximum TEC value is scaled to 70 TECu). Figure 3-4 shows the corresponding IRI model results, showing that, as expected, the statistical model cannot replicate such extreme events.

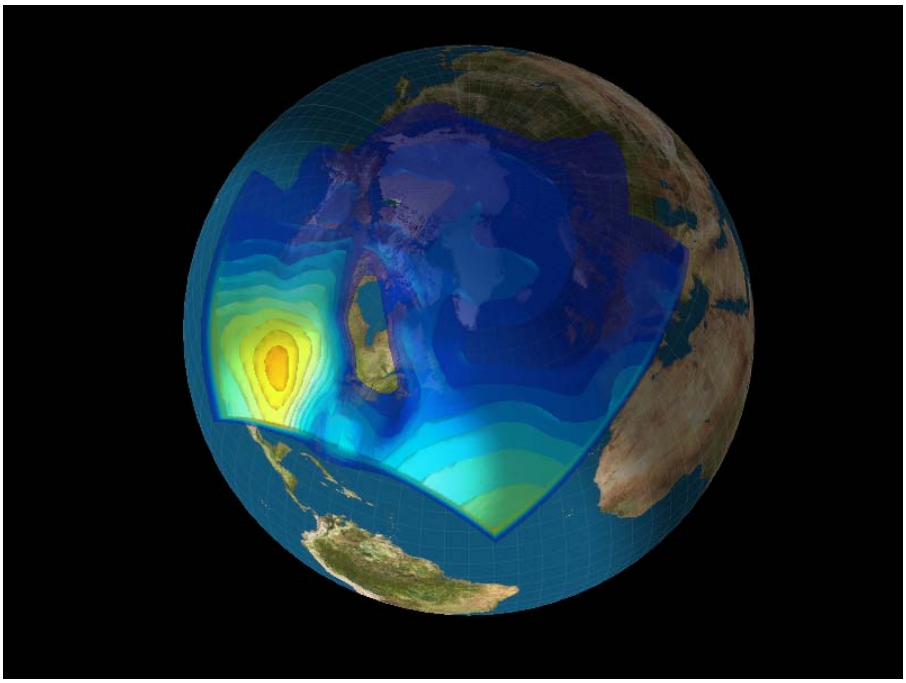

Figure 3-2: Contours of TEC Over the Polar Region from MIDAS.

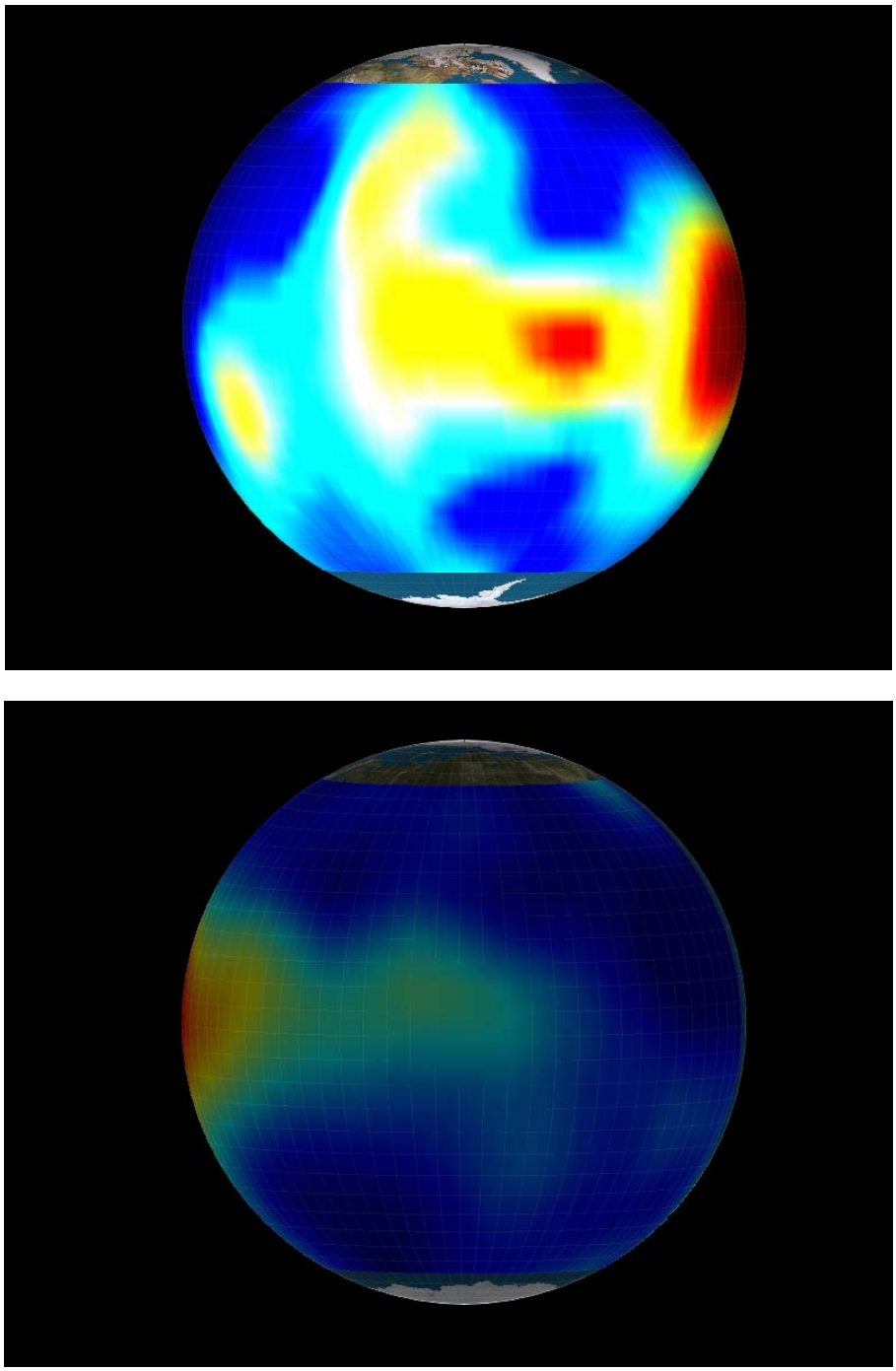

Figure 3-3: Contours of TEC Over Low-Auroral Latitudes from MIDAS.

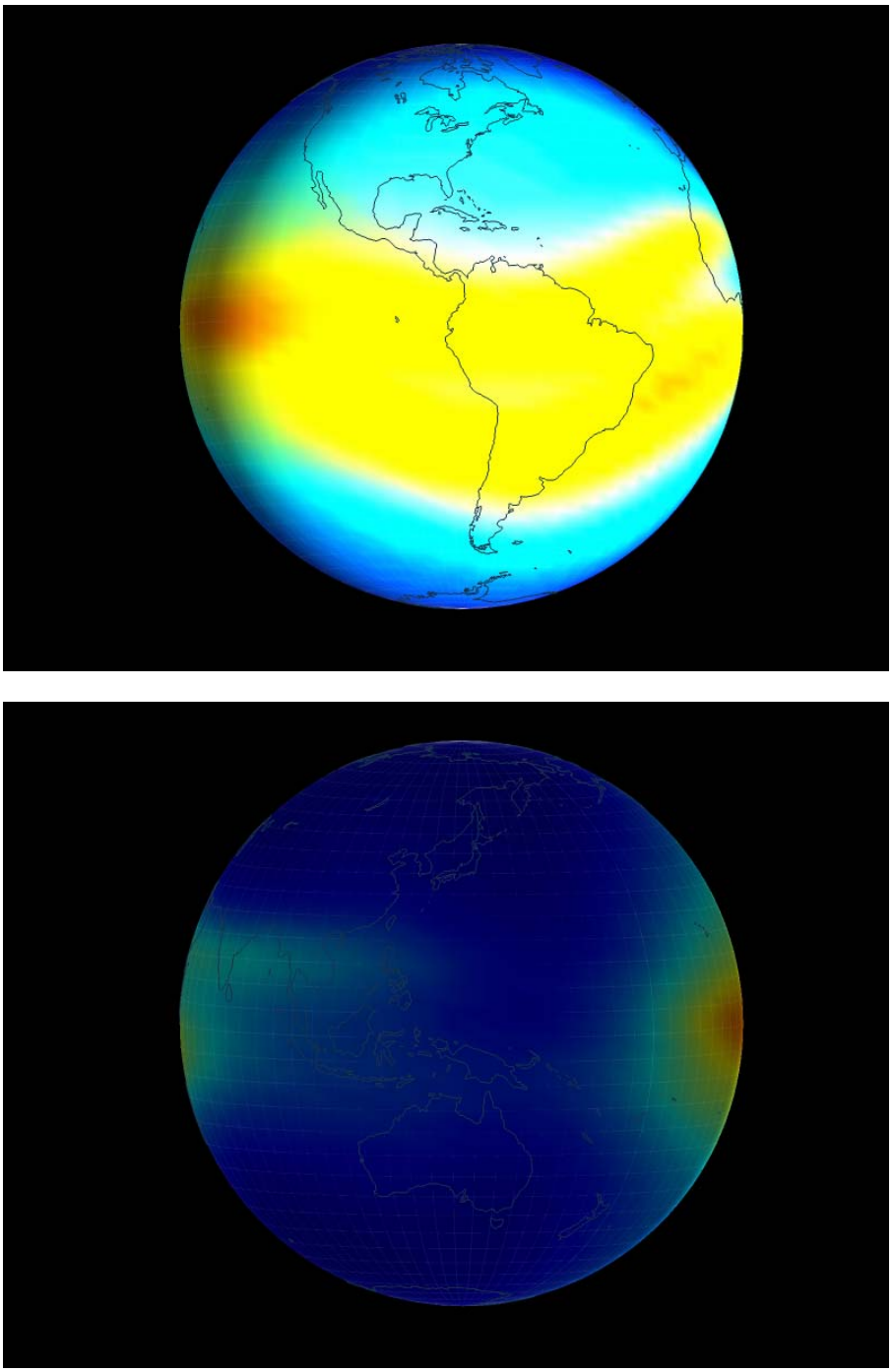

Figure 3-4: Contours of TEC Over Low-Auroral Latitudes from IRI.

3.1.4 Short-Term Forecasting and Verifications

The accuracy of the imaging technique has been examined thorough a series of simulation studies. GPS provides two different quantities that relate to the ionospheric total electron content (TEC) – the differential phase advance and the differential group delay. The phase of the signal is a highly-accurate measurement that gives a relative change in the TEC whereas the group delay is subject to stable biases that are in the largest component of their values specific to a given receiver or satellite. This dual measurement system

allows the assessment of imaging accuracy, by using only the phase data to make the images the code delay data can be reserved for image accuracy assessment. Thus through both simulation and experiment the accuracy of the imaging technique in terms of TEC mapping has been assessed (Dear et al., 2006).

The vertical profile of electron density obtained from ionospheric imaging using only ground-based data has also been assessed. A new approach was developed whereby the peak density and scale heights from ionosonde data were used to assist the reconstruction. This is particularly applicable to HF applications where the vertical profile is critical to the outcome.

Case study verifications of MIDAS have also been performed, for example in comparisons with incoherent scatter data the trough has been imaged (Meggs et al., 2005) verifications have been made showing the uplift of the ionosphere during a storm (Yin et al., 2004).

MIDAS has a short-term forecasting capability built in (up to 12 hours ahead). The forecasting algorithms are based on pattern recognition approaches. Various methods for forecasting the daytime TEC over large-regions were explored. It was found that methods that worked well for isolated locations did not translate to wide-area mapping and could produce spurious artefacts. The preferred approach involved the use of a climatological model coupled to the imaging. This was shown to be applicable even during disturbed conditions. For the night-time, the main trough was the dominant feature and its movement and density changes necessitated the use of feature recognition coupled into the forecasting (Dear et al., 2007).

MIDAS is currently being run in a real-time and forecasting mode both over the UK and over Southern Europe, and is being tested for single-frequency GPS ionospheric delay corrections.

3.1.5 Summary and Discussion

One method to produce maps of the electron density, MIDAS, has been described here. The method is the least model-reliant of a family of techniques that range from tomographic imaging to data assimilation into a physical model.

MIDAS can be used to image the ionosphere either on a low-resolution global scale (2 degree voxels) or locally at higher resolutions (typically 0.25 degree voxels). The vertical size of the voxels ranges from 5 km to 50 km. The decisions about which mode to run in depend on many factors that are outlined below.

For applications where the bulk electron density and TEC (large-scale greater than 100km structures) are the main interest the technique performs equally well in high or low-resolution mode and there is not need to operate at high resolution. Nearly all of the testing of MIDAS that has been done is essentially for this type of imaging. Examples for this application include Faraday rotation estimates for SAR and single-frequency GPS delay mapping.

For higher resolution imaging, for example to examine localised gradients in the ionosphere, there is little chance to find independent instruments to compare with. Case study comparisons with ISRs show that the gradient on the southern wall of the main trough are well replicated (Meggs et al., 2005). Larger sample (1 year) statistical studies of the trough have been done with MIDAS (Mitchell 2004, USAF EOARD report) and verified using Langmuir probe measurements where available. These results are of interest for in-beam synthetic aperture radar studies and relate to features on length scales some km to tens of km.

For applications requiring accurate representations of vertical gradients in the ionosphere (e.g. HF communications coverage maps) data or models containing good information about the bottomside gradients must be used into the MIDAS imaging. Examples of such data sources include oblique sounders, ionosondes and radio-occultations.

Future developments to MIDAS include a statistical tomography mode for imaging regions causing ionospheric scintillations likely to be responsible for communication and navigation outages in the equatorial region.

3.1.6 Acknowledgements

MIDAS was originally conceived by the author and developed under an EPSRC new investigator grant (Mitchell and Watson, 2000).

MIDAS has since benefited from a variety of funding sources, including the UK research councils EPSRC and PPARC, and the USAF and BAE Systems. The author acknowledges the contributions of all of the team at the University of Bath: in particular Peter Watson for the support and encouragement during the early phases of the work; Paul Spencer for the programming and mathematical innovation; Ping Yin, Robert Meggs, Bettina Zapfe and Richard Dear for the testing and application of MIDAS to both science and engineering problems. We also gratefully extend our thanks to the IGS and the creators of IRI.

3.1.7 References

[1] Bilitza, D., International Reference Ionosphere 2000, Radio Science, 36 (2): 261-275 Mar-Apr 2001.

[2] Bust, G. S., T. W. Garner, T. L. Gaussiran II, Ionospheric data assimilation three-dimensional (IDA3D): A global, multisensor, electron density specification algorithm, Journal of geophysical research-space physics 109 (a11): art. No. A11312 Nov 27 2004.

[3] Cilliers, P. J., Opperman, B. D. L., Mitchell, C. N., Spencer, P. S. J., Electron density profiles determined from tomographic reconstruction of total electron content obtained from GPS dual frequency data: First results from the South African network of dual frequency GPS receiver stations, IRI: Quantifying Ionospheric Variability Advances In Space Research 34 (9)2049-2055 2004.

[4] Dear, R. M., Mitchell C.N., GPS interfrequency biases and total electron content errors in ionospheric imaging over Europe, RADIO SCIENCE 41 (6): Art. No. RS6007 Dec 19 2006.

[5] Dear, R. M., Wide-area mapping and forecasting of TEC, PhD Thesis, University of Bath, 2007.

[6] Fremouw, E.J., J.A. Secan and B.M. Howe, 1992, Application of stochastic inverse theory to ionospheric tomography, *Radio Science*, **17**, 721.

[7] Hajj, G.A., Wilson, B.D., Wang, C., Pi X., Rosen, I.G., Data assimilation of ground GPS total electron content into a physics-based ionospheric model by use of the Kalman filter, Radio Science 39 (1), art. no. rs1s05 Feb 24 2004.

[8] Materassi, M. and Mitchell, C.N., Imaging of the equatorial ionosphere, Annals of Geophysics 48 (3): 477-482 Jun 2005.

[9] Meggs, R. W., Mitchell, C.N., Spencer, P. S. J., A comparison of techniques for mapping total electron content over Europe using GPS signals Radio Science 39 (1): Art. No. RS1S10 Feb 25 2004.

[10] Meggs, R.W., Mitchell, C.N., Howells, V.SC., Simultaneous observations of the main trough using GPS imaging and the EISCAT radar Annales Geophysicae 23 (3): 753-757 2005.

[11] Mitchell, C.N., Spencer, P.S.J. A three-dimensional time-dependent algorithm for ionospheric imaging using GPS ANNALS OF GEOPHYSICS 46 (4): 687-696 Aug 2003.

[12] Mitchell, C.N., D.G. Jones, L. Kersley, S.E. Pryse and I.K. Walker, Imaging of field-aligned structures in the auroral ionosphere, Ann. Geophysicae, **13**, 1311-1319, 1995.

[13] Mitchell, C.N., Walker, I.K., Pryse, S.E., Kersley, L., McCrea, I.W., Jones, T.B., First complementary observations by ionospheric tomography, the EISCAT Svalbard radar and the CUTLASS HF radar, Annales Geophysicae-Atmospheres Hydrospheres And Space Sciences 16 (11): 1519-1522 Nov 1998.

[14] Mitchell, C.N. Imaging of near-Earth space plasma Philosophical Transactions of the Royal Society of London Series A-Mathematical Physical And Engineering Sciences 360 (1801): 2805-2818 Dec 15 2002.

[15] Munk, W., and C. Wunsch, Ocean acoustic tomography: A scheme for large scale monitoring, Deep Sea Res., **26A**, 123, 1979.

[16] Rogers, N.C., Mitchell, C.N., Heaton, J.A.T., Cannon, P.S., Kersley, L., Application of radio tomographic imaging to HF oblique incidence ray tracing, RADIO SCI 36 (6): 1591-1598 Nov-Dec 2001.

[17] Spencer, P. S. J. and C. N. Mitchell, 2001, Multi-instrument Data Analysis System, Proc. Beacon Satellite Symposium, Boston.

[18] Yin, P., Mitchell, C.N., Spencer, P.S.J., Foster, J.C. Ionospheric electron concentration imaging using GPS over the USA during the storm of July 2000, Geophysical Research Letters 31 (12): Art. No. L12806 Jun 22 2004.

[19] Yin, P., Mitchell, C.N. Use of radio-occultation data for ionospheric imaging during the April 2002 disturbances Source: GPS SOLUTIONS 9 (2): 156-163 Jul 2005.

3.2 RADIO TOMOGRAPHIC INVESTIGATIONS OF PLASMA STRUCTURE IN THE HIGH-LATITUDE IONOSPHERE: CURRENT KNOWLEDGE AND OPEN QUESTIONS

(S. Eleri Pryse and Helen R. Middleton University of Wales Aberystwyth, UK)

3.2.1 Introduction

The high-latitude ionosphere is a highly structured medium, comprising electron density irregularities over a large range of scale sizes. Of particular relevance to this report are enhancements and depletions on horizontal spatial scales of tens to hundreds of kilometres. Such structures include the tongue of ionisation and patches in the polar cap, boundary blobs in the evening auroral region and the main ionisation trough. The steep density gradients associated with the features and accompanying small-scale irregularities are of particular concern to the performance of practical navigation and communications radio systems. The basic physical processes underlying the formation of the structures are reasonably well established although the relative contributions resulting from photo- and impact-ionisation, chemical loss and plasma transport in any given situation and at any particular time remain open to debate. There is a need to establish this balance before there can be a proper understanding of the complex morphology of the spatial distribution of electron density at high latitudes. The variability in the occurrence, structure and location of the observed features means that it is not yet possible to represent them accurately in physical or parameterised models of the ionosphere at high latitudes. In addition, knowledge of the effects of space-weather disturbances is inadequate and their mitigation presents particular problems to current and planned applications of navigation satellite technology.

Radio tomographic imaging has proved to be a technique that is particularly adept for the study of large-scale spatial structures in ionospheric electron density. Recent results are summarised here, derived in the main from experimental studies using the method. Some studies relate to investigations aimed at validation and development of models of the ionosphere at high latitudes that are required for the mitigation of propagation effects on applied radio systems.

3.2.2 High-Latitude Convection and Plasma Distribution

Interaction between the interplanetary magnetic field (IMF) carried by the solar wind and the geomagnetic field is the key to the convection that drives the plasma in the polar cap. Magnetic reconnection occurs when the IMF impinges on the Earth's magnetic field, with the location of reconnection being dependent on the orientation of the IMF (Dungey, 1961; Lockwood, 1998). This in turn controls the convection flow pattern of the plasma in the high-latitude ionosphere. When the IMF is directed southwards, that is with a negative B_z component, the reconnection occurs near the equatorial plane, with the resultant evolution of the flux tubes driving the familiar two-cell ionospheric convection pattern at high latitudes. There is an anti-sunward plasma drift across the polar cap, with the return flow at lower latitudes on the dawn and dusk sides. The flow patterns under other orientations of IMF become increasingly more complicated (Reiff and Burch, 1985; Cowley, 1998). A positive B_z component drives polar lobe cells, which have a flow initially sunward in the cusp region and are flanked by viscous driven convection cells on the dusk and dawn sides at lower latitudes. A B_y component results in asymmetry of the pattern around the noon-midnight meridian. In practice, the constantly changing magnitude and direction of the IMF gives rise to substantial variations in the flow pattern and consequently in the structure of the plasma that is transported through the polar cap. If the ionisation is at high altitude the chemical loss rate is slow so that long-lived structures can be transported from the dayside through the polar cap to be deposited into the auroral zone on the nightside.

Several experimental techniques have been used to measure the electron density and electron content in the polar region. The methods and results are reviewed by Crowley (1996). Complete understanding of the mechanisms responsible for the increased density in the region is still open, with both soft-particle precipitation (Weber et al., 1984) and photoionisation (Buchau et al., 1985) from sub-polar latitudes being cited. Experimental evidence suggests that dayside photoionisation from lower latitudes can be entrained into the polar convection pattern in what has become known as a tongue of ionisation (TOI) (Valladares et al.,1994). Pryse et al. (2004) proposed that the high densities originate from the equatorward side of the afternoon cell of the high-latitude convection, and supportive evidence for a latitudinally-extended feature near magnetic noon was presented by Sims et al. (2005). Several methods have been proposed for breaking up the TOI into the discrete patches that are found in the cross-polar anti-sunward flow when the B_z component of the IMF is negative (McEwen and Harris, 1996). Possible mechanisms include temporal variations in the high-latitude convection pattern in response to changes in B_y (Sojka et al., 1993), expansion and contraction in the size of the polar cap region (Anderson et al., 1988), and an increase in the rate of ionisation recombination in flow channel events (Rodger et al., 1994). Recent observations have suggested that the ionisation may be formed into patches before it enters the polar cap (Moen et al., 2006). The balance of the contributions from the different mechanisms remains an open question. An early modelling study by Robinson et al. (1985) suggested that the structures with enhanced density found in the polar cap may exit from the polar flow into the nightside sector where they become extended in longitude but restricted in latitude to form features known as boundary blobs. However, another study by Jones et al. (1997) provided convincing evidence that such localised structures in the auroral ionosphere can be produced *in situ* by soft particle precipitation.

Recent collaborative studies led by the University of Wales Aberystwyth (UWA) have investigated aspects of the effects of convection on the distribution of plasma at the high latitudes. These have been mainly case studies, but also include statistical investigations.

3.2.3 Experimental Systems

The radio tomography experiment of the University of Wales Aberystwyth is central in the investigations. It comprises a chain of ground-based satellite receivers at Ny-Ålesund (78.91ºN, 11.94ºE) and Longyearbyen (78.22ºN, 15.83ºE) on Svalbard, Bjørnøya (74.52ºN, 19.05ºE) and Tromsø (69.58ºN, 19.22ºE) on mainland Norway (Figure 3-5). The receivers monitor the phase coherent signals at 150 MHz and 400 MHz, transmitted by the satellites of the NIMS (Navy Ionospheric Monitoring System) constellation in polar orbits at altitudes of about 1100 km. The receiving systems measure the total electron content (TEC) along a large number of intersecting satellite-to-receiver ray-paths. Tomographic inversion of the TEC yields the electron density over a latitude-versus-altitude plane through the ionosphere (Pryse, 2003).

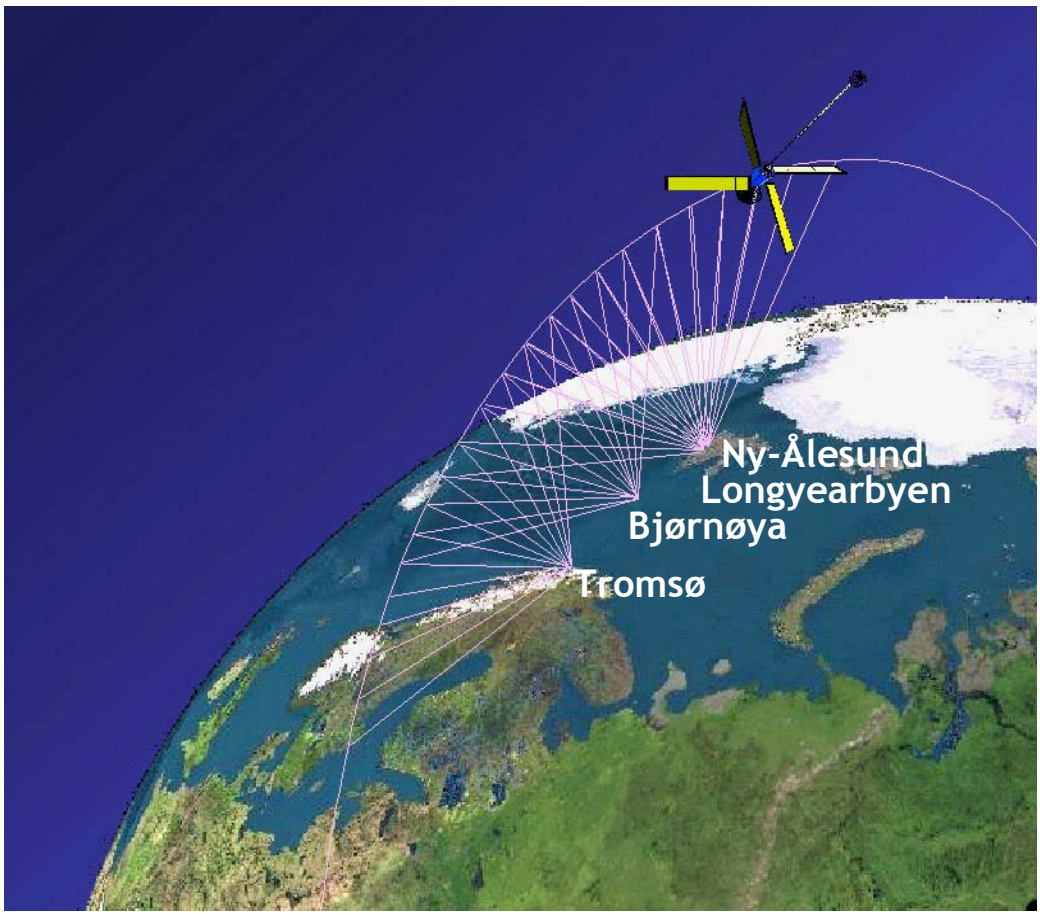

Figure 3-5: Schematic Showing the Geometry of the Radio Tomography Experiment of the University of Wales Aberystwyth in Northern Scandinavia.

The radio tomography chain forms part of the network of the International Ionospheric Tomography Community (IITC) with other high-latitude receiver chains in Alaska, Greenland, Scandinavia and Russia being operated by collaborating researchers in several countries (Figure 3-6).

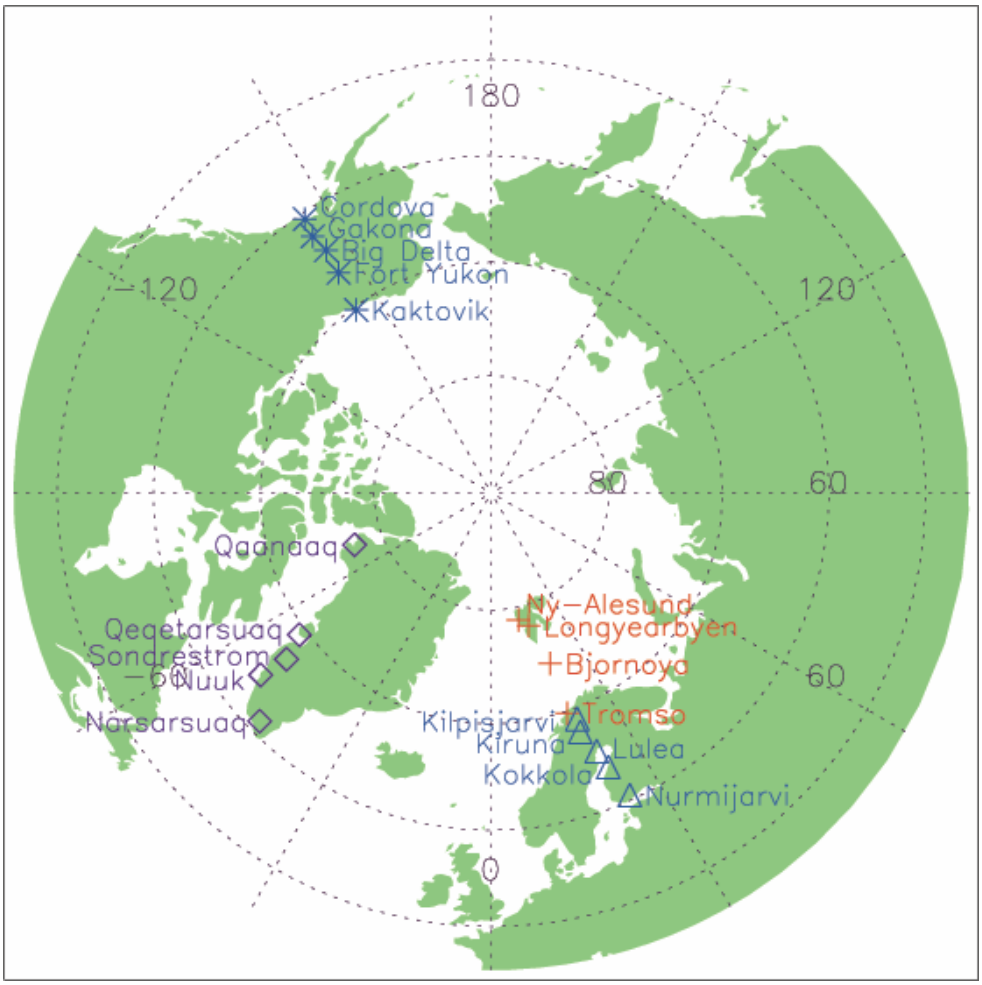

Figure 3-6: Receiver Locations of High-Latitude Radio Tomography Chains of the International Ionospheric Tomography Community.

Other experimental observations used in the studies come from the European Incoherent Scatter radar facility (EISCAT) (Rishbeth and Williams, 1985) and the Super Dual Auroral Radar Network (SuperDARN) (Greenwald et al., 1995). These measurements are instrumental in efforts to identify the plasma source, to resolve spatial and temporal changes in the ionisation distribution, and to estimate the plasma flow patterns. The EISCAT facility, with radars near Tromsø on mainland Norway and Longyearbyen on Svalbard, measures a number of plasma parameters, including electron density and electron and ion temperatures, while the SuperDARN radars give the line-of-sight velocity of the F-region convection flows. These flow observations are then inverted by a spherical harmonic fitting technique, described by Ruohoniemi and Baker (1998), to produce polar-projection maps of the high-latitude electric potential that are representative of the ionospheric convection patterns.

3.2.4 Summaries of Recent Case Studies

The main results from recent collaborative multi-instrument studies, led by the University of Wales Aberystwyth, are summarised here. The first two cases relate to the dayside and nightside sectors respectively when the plasma was drawn antisunward by the convective flow through the polar region. The third presents observations of the plasma distribution in the afternoon sector when IMF B_z was positive. It provides for the first time evidence of a tongue of enhanced plasma density circulating the polar cap, which is closed to the inflow of plasma under conditions of B_z northwards.

3.2.4.1 Dayside Polar Ionosphere: Source Region of the Tongue of Ionisation

A region of enhanced F-region ionospheric densities was observed by the EISCAT Svalbard radar (ESR) at high latitudes near local magnetic noon under conditions of IMF B_z negative (Pryse et al., 2004). The source of the plasma was investigated using optical, spacecraft, radar and tomographic instrumentation. In this instance it was possible to rule out *in situ* soft-particle precipitation as the production mechanism. The equivalent vertical total electron content (TEC) measured at the four sites of the UWA Scandinavian tomography chain (Figure 3-7) show a latitudinally-restricted region of enhanced ionisation with maximum at about 73ºN-74ºN, superimposed on the gradient of the dayside ionosphere created by photo-production. The study demonstrated that this region of increased ionisation at sub-auroral latitudes, seen during three consecutive satellite passes, was the likely source of the plasma enhancement observed by the ESR at polar latitudes, with the flux tubes being drawn poleward by the convective flow. The build-up of densities at the lower latitudes was proposed to occur at the equatorward edge of the afternoon high-latitude convection cell, where plasma is exposed to sunlight for an extended period as it flows slowly sunward toward magnetic noon under the influence of the combined effects of high-latitude convection and co-rotation.

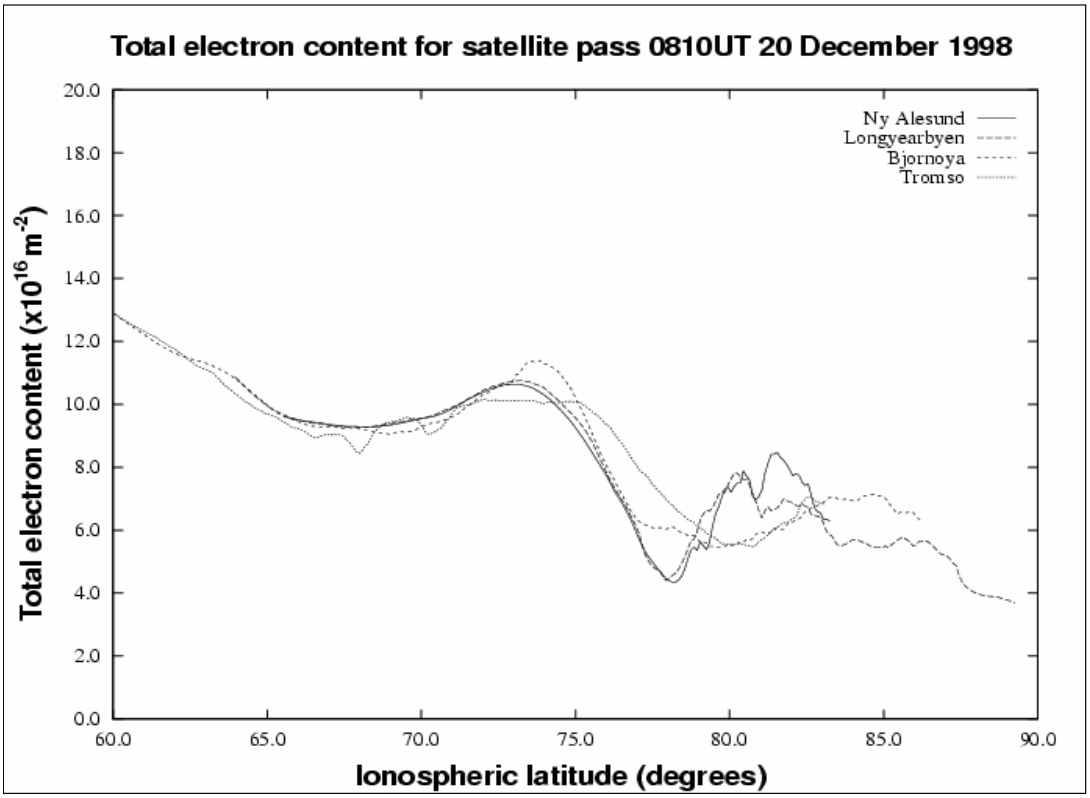

Figure 3-7: Equivalent Vertical Total Electron Content Measured at the Four Receiving Sites of the Scandinavian Tomography Chain During a NIMS Satellite Pass that Crossed Latitude 75ºN at 0810UT on 20 December 1998. (Pryse et al., 2004)

3.2.4.2 Nightside Ionosphere: Reconfiguration of a Polar Patch into a Boundary Blob

A long-lived, high-altitude, cold plasma enhancement observed in the anti-sunward convective flow across the polar cap was studied using measurements from the tomography experiment and the SuperDARN and EISCAT radar facilities (Pryse et al., 2006a). A projection of the feature to later times suggested that it was reconfigured in the Harang discontinuity to form an enhancement that was elongated in longitude in the evening sunward return flow of the high-latitude convection. This was supported by a second tomography image, some 45 min later, which showed a boundary blob almost coincident with the

projection. The tomographic reconstruction supporting the interpretation also showed another enhancement equatorward of the reconfigured blob, likely to have been produced by soft precipitation. Taken together, the observations (Figure 3-8) indicated that the two mechanisms proposed previously in the literature for the production of boundary blobs, were operating simultaneously to form two distinct density features separated slightly in latitude. The finding is of relevance to radio propagation applications as boundary blobs often form the poleward boundary of the main ionisation trough in this time sector.

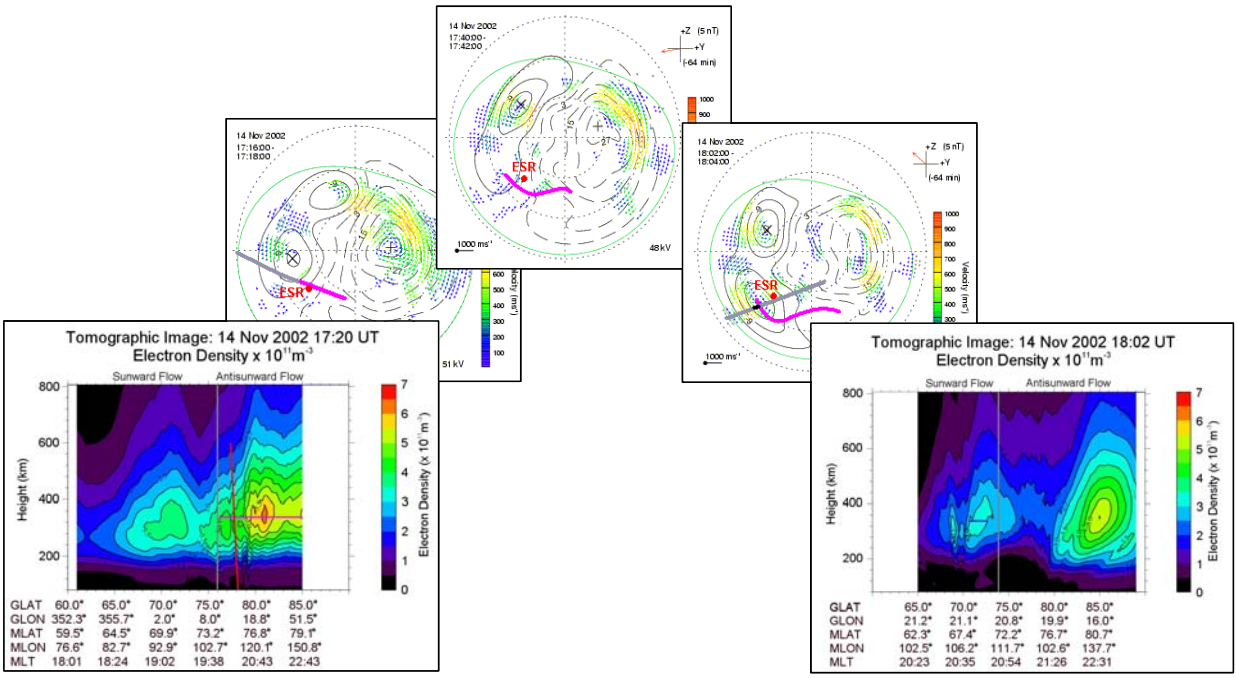

Figure 3-8: A Polar Patch can be Seen in the Tomography Image from a Satellite Pass at 1720UT on 14 November 2002 (left).

The pink line marks its latitudinal extent which maps into the antisunward plasma flow shown on the SuperDARN electric potential patterns. Projection of the feature through successive SuperDARN observations (centre) shows that the line is reconfigured by the flow, becoming elongated in longitude in the sunward return flows of the dusk and dawn cells. A second tomography image at 1802UT (right) shows that the pink projection is essentially collocated with a boundary blob centred ~72ºN. A second distinct boundary blob is also seen in the image at slightly lower latitudes. (Pryse et al., 2006a)

3.2.4.3 A Tongue of Ionisation with IMF B_z Positive

A series of twelve consecutive satellite passes, under conditions of stable IMF B_z>0, from the tomography chain of the Applied Research Laboratories (ARL), University of Texas at Austin, in Greenland and the UWA chain in Scandinavia showed a persistent high-latitude density enhancement that was investigated by Middleton et al., 2005a. The images (samples of which are given in Figure 3-9) were interpreted as evidence for a tongue of ionisation when IMF B_z was positive. Even though the polar cap was closed to plasma inflow from lower latitudes, the dayside photoionisation drawn poleward by viscous convection cells was shown to flow around the periphery of the polar cap. This formed a band of enhanced densities that decreased with increasing time displacement from magnetic noon, due to chemical recombination.

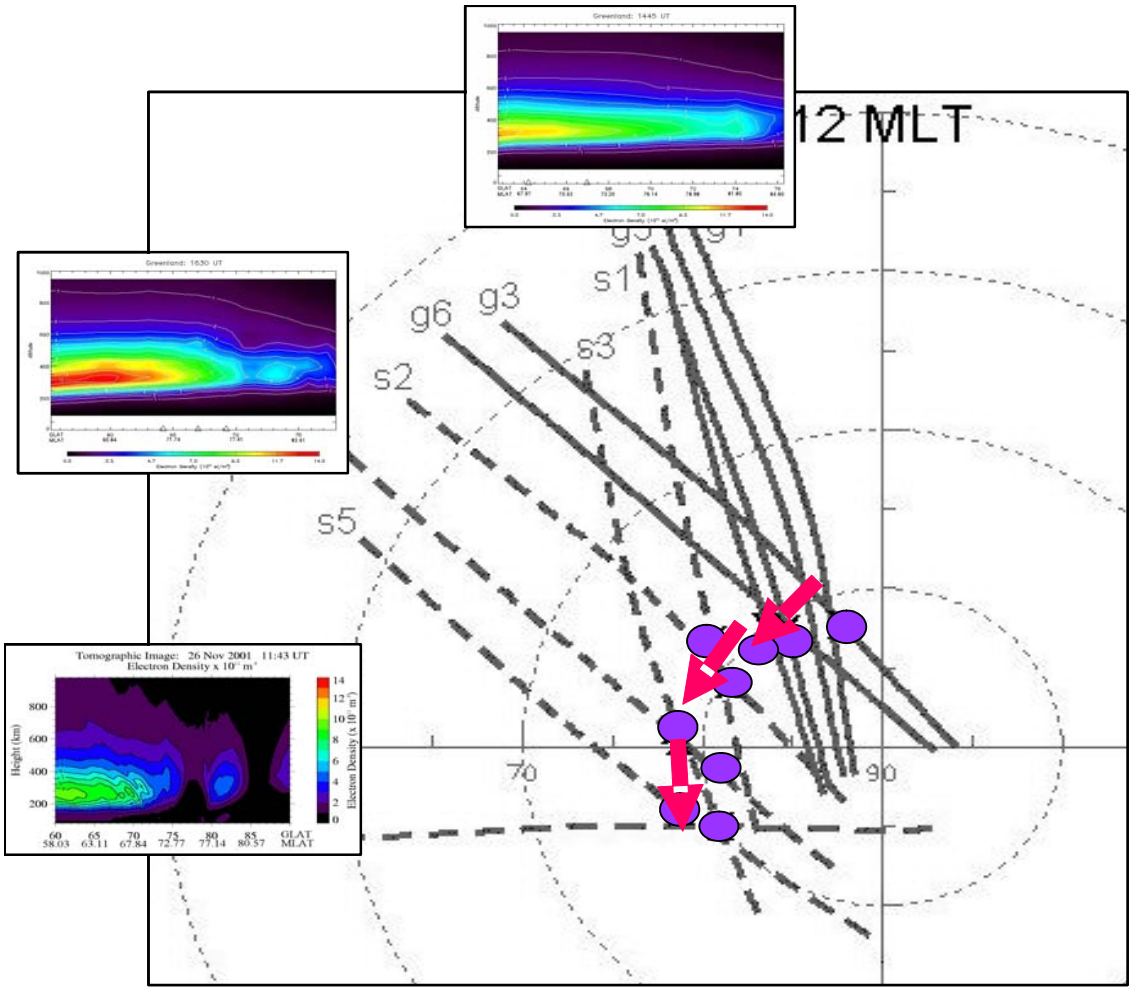

Figure 3-9: Sample Tomography Images from the Greenland and Northern Scandinavian Tomography Receiver Chains for 26 November 2001 Showing Cross-Sections Through a Tongue of Ionisation Drawn around the Dusk-Side Periphery of the Polar Cap under Conditions of Stable IMF B_z>0.

The purple dots on the satellite trajectories show the locations of the density enhancements observed in the series of satellite passes and the pink arrows show the antisunward plasma drift implied from DMSP horizontal drift measurements. (Middleton et al., 2005a)

3.2.5 Tomography and the CTIP Model: A Case Study

Physical models have an important role to play in aiding understanding of the relative contributions of the various physical processes underlying the complex plasma structure of the ionised atmosphere. The Coupled Thermosphere Ionosphere Plasmasphere (CTIP) model was developed over many years, by the University of Sheffield and University College London integrating a thermospheric model (Fuller-Rowell and Rees, 1980) with models of the plasmasphere and high-latitude ionospheres (Quegan et al., 1982).

A tomography reconstruction from a study relating observations and modelling (Middleton et al., 2005b) is shown in Figure 3-10. The image, for a satellite pass that crossed 75ºN latitude at 0007UT on 13 December 2001, clearly reveals a structured nighttime ionosphere with a large enhancement between 62°MLAT and 70.5°MLAT where the electron density exceeds $7x10^{11}m^{-3}$. The darkened winter nighttime conditions at these latitudes rule out direct production by solar EUV as a source mechanism for the increased densities.

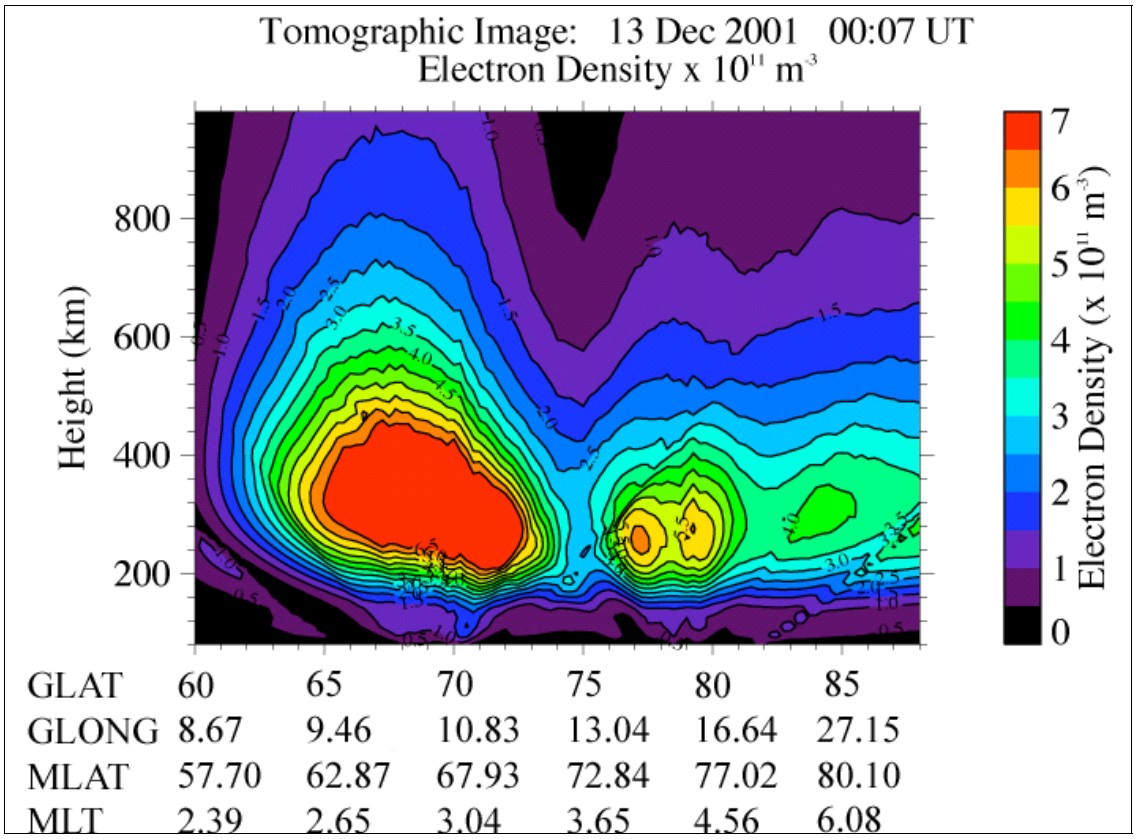

Figure 3-10: Tomographic Image for a Satellite Pass at 0007UT on 13 December 2001. A large density enhancement can be seen in the equatorward section of the field-of-view.

The feature was observed in five consecutive tomography images between 2305UT on 12 December and 0243UT on 13 December, three from the UWA tomography chain in Scandinavia and the other two by stations in the UK also operated at the time by UWA. The trajectories of the five satellite passes are shown in Figure 3-11, mapped on a SuperDARN electric potential pattern that was representative of the convection flow during the time of interest. The mapping of the maximum density in the enhancement for each image is indicated by a coloured dot. The dots lie mainly in the return flow of the dawn cell, indicating that the flux tubes are likely to have convected from the polar cap. Simultaneous observations by the EISCAT incoherent scatter radar on mainland Norway confirmed the high densities, but the corresponding cold electron temperatures ruled out in situ precipitation as the production mechanism. Understanding the origins of such enhancements is of interest, not only to the interpretation of the physical processes operating in the high-latitude ionosphere, but also to radio propagation applications, as this large ionisation feature forms the poleward wall of the main ionisation trough in the post-midnight sector.

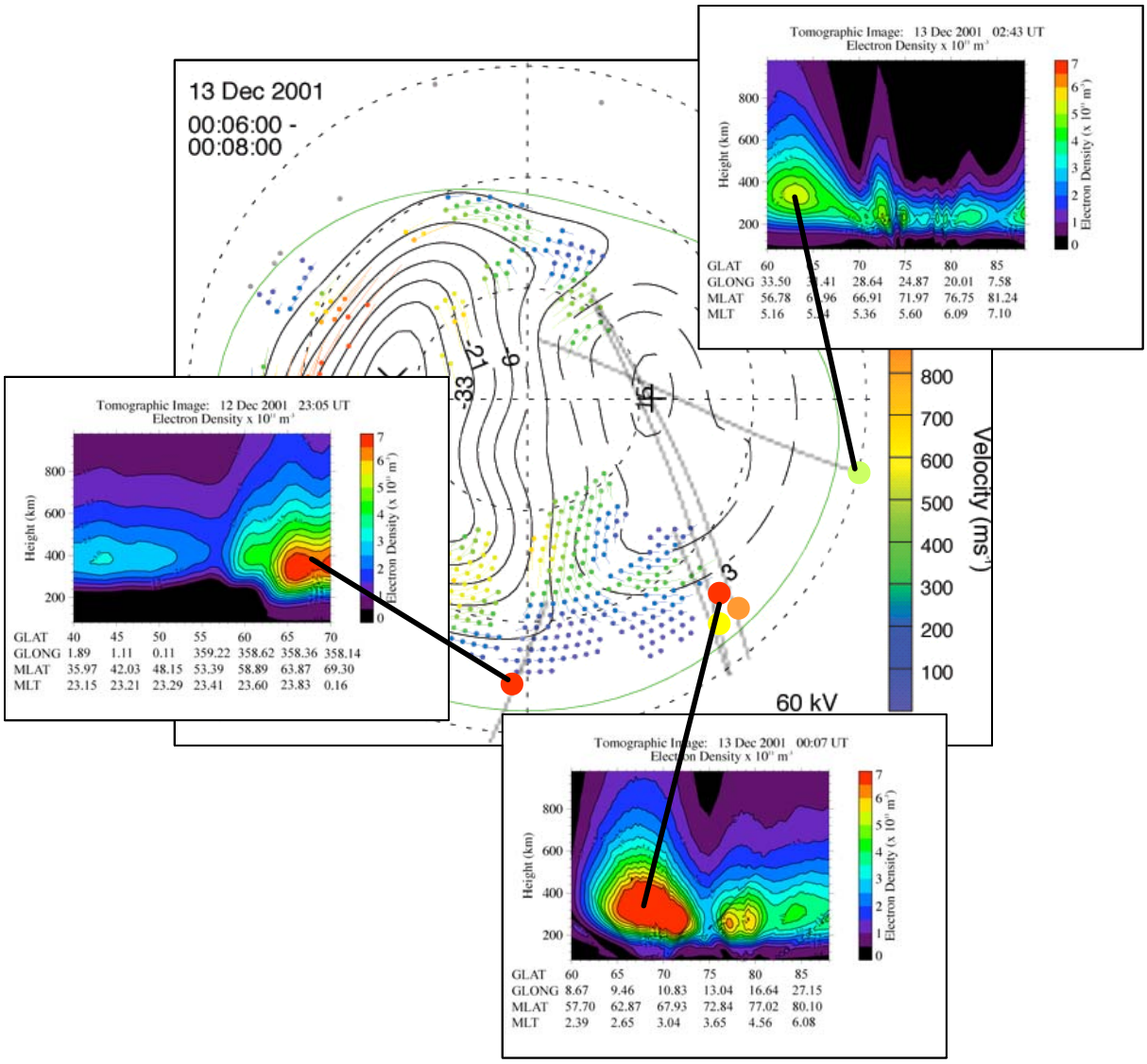

Figure 3-11: Sample Tomography Images between 2305UT on 12 December 2001 and 0243UT on 13 December 2001. The locations of the maximum electron density and mapped trajectories for all five satellite passes are shown superimposed on a representative electric potential (plasma flow) pattern measured by the SuperDARN radars.

The CTIP model provides support for the interpretation. Figure 3-12 shows a sequence of output plots of F_2-layer electron density, at 3-hourly intervals, from a model run with input parameters appropriate to the geophysical conditions at the time of observations. Magnetic noon is at the top of each panel, with magnetic midnight at the bottom, dawn is on the right-hand-side and dusk on the left. The latitude scale extends from 50ºMLAT on the outer circumference to the magnetic pole at the centre. The small white region near the centre of each panel indicates the location of the geographic pole. The white line on each panel shows the approximate location of the Scandinavian tomography receiver chain. Panels f) and g) for the UT intervals of relevance to the study show a TOI originating on the dayside and being drawn into the nightside, and then around into the dawn side at lower latitudes. It can be seen that at 0UT to 03UT the observations are clearly sampling a region of plasma drawn over the polar cap in a TOI.

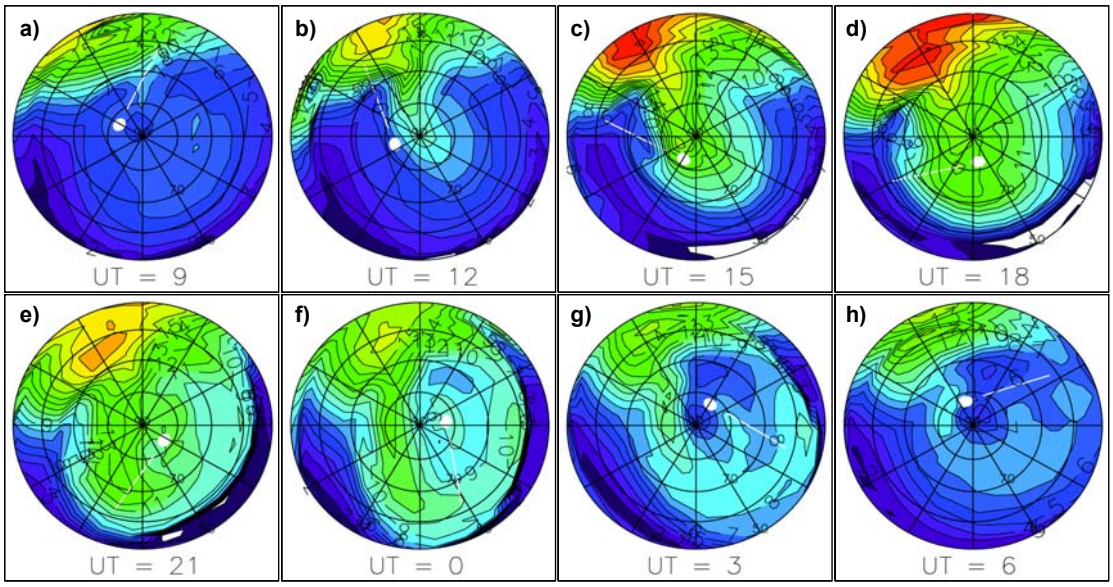

Figure 3-12: Electron Densities in the Polar F_2-Layer from the CTIP Model Plotted as a Function of MLT and MLAT. The latitude scale extends from 50º to the geomagnetic pole, geomagnetic noon is at the top of each circle and the panels are at 3-hourly intervals of UT.

The panels of Figure 3-12 throughout the day show that the TOI maximises near 18-21UT when Europe is entering the evening/nightside but the feature is much less marked around 06-09 UT when the European sector is on the dayside. This variation is a consequence of the offset between the geographic and geomagnetic reference frames; the photo-production is controlled by solar processes in the geographic frame while the high-latitude convection is driven in the geomagnetic frame. A larger proportion of the convection pattern is therefore in sunlight during the 18-21UT interval than in the earlier interval. The modelling thus suggests that the effect of the TOI in the evening sector is likely to be more prominent at European longitudes than in the US sector, whilst the converse is true for the 06-09UT interval. The results are consistent with previous work by Bowline et al. (1996) where three locations in different longitude sectors were considered, and which indicated that the TOI was expected to be prominent at Ny-Ålesund in the evening with B_y negative.

3.2.6 Statistical Analysis for Model Verification and Development

Physical models provide a valuable resource for interpretation of ionospheric observations, although measurements are also crucial for the verification and development of both physical, parameterised and empirical models. Preliminary steps have been made in the analysis of statistical results from tomographic observations for comparisons with models.

3.2.6.1 Dayside High-Latitude Trough

The dayside high-latitude trough is believed to be the extension of the main or mid-latitude nighttime trough into the earlier time sector of magnetic afternoon. It is a persistent feature of the wintertime auroral ionosphere at latitudes of about 70ºN to 75ºN. Radio tomography observations from December 2001 were used to map the location and latitudinal structure of this trough under quiet geomagnetic conditions (Kp≤2) near winter solstice (Pryse et al., 2005). The red curves and error bars respectively in Figure 3-13 show the median latitudinal distributions and associated inter-quartile ranges for N_mF_2. The CTIP model was run with input parameters representative of the observing conditions to examine the influences of both precipitation and convection on the model. The curves of Figure 3-13 correspond to four different combinations as follows: both precipitation energy input and high-latitude convection switched-on (DecCP), precipitation off

but convection on (DecC), precipitation on but convection off (DecP), and both precipitation and convection switched off (Dec).

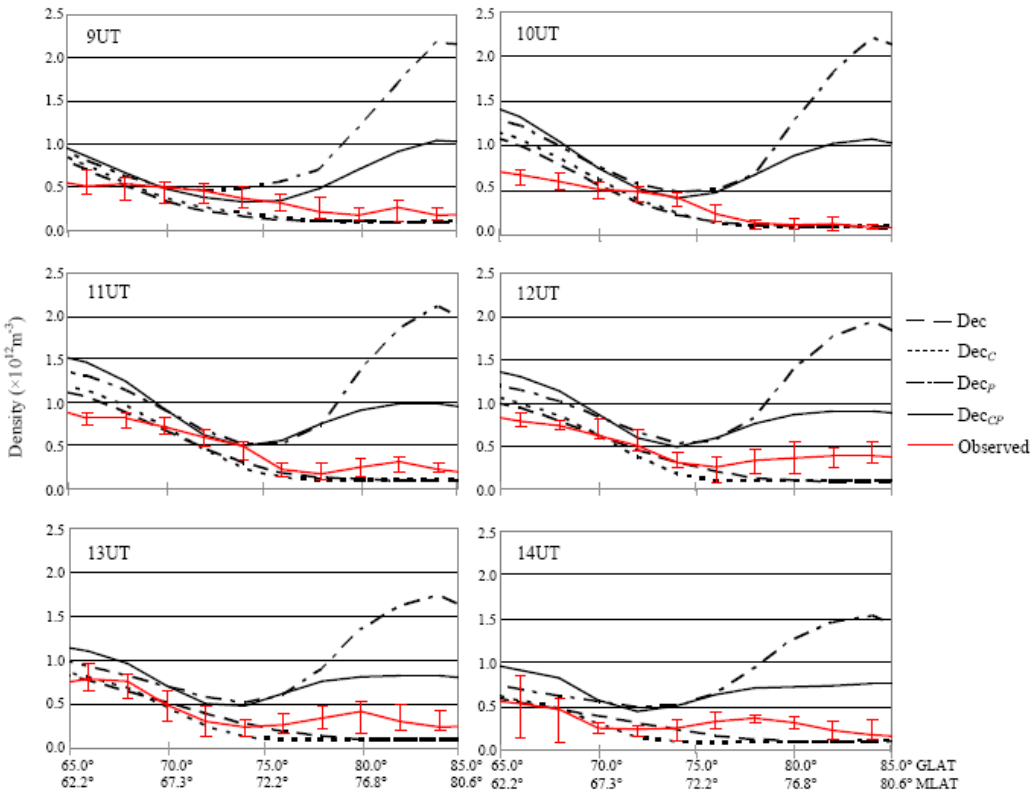

Figure 3-13: Latitudinal Variation of N_mF_2 in 1-hour Bins of UT Obtained from Tomography Observations in Scandinavia During December 2001 with Kp≤2. Corresponding outputs from the CTIP model are also shown with the explanations for the curves given in the text.

It can be seen that the model reproduces the general behaviour of the observed troughs, with photoionisation responsible for the equatorward wall, precipitation ionisation on the poleward wall, and a general decrease in trough latitude with increasing time. However, closer inspection reveals that the auroral ionisation is substantially overestimated in the model, the latitude of the trough minimum is generally displaced from that observed, and the equatorward migration of the trough with UT spans a greater latitudinal range in the observations than in the model. A further discrepancy arises from the shape of the equatorward trough wall, with the observed densities being maintained at a higher level than those predicted from photoionisation and a steeper decrease into the trough minimum.

3.2.6.2 Parameterisation of the Main Ionospheric Trough in the European Sector

Another investigation (Pryse et al., 2006b) was directed towards representing the latitudinal position and shape of the main or mid-latitude trough, observed during the evening and nighttime at UK latitudes, in such a way that the observations could be used for direct comparison and validation of ionospheric models. Satellite transmissions from the NIMS constellation were monitored at three tomography stations in the UK for a year between September 2002 and August 2003. The vertical total electron content as a function of latitude was determined for the passes by integration through the tomographic images. The TEC measurements were then used to characterise the structure and dynamics of the main ionospheric trough in terms of a set of defined parameters. The observations confirmed the well-established equatorwards movement of the trough throughout the night and with increased geomagnetic activity.

The TEC values in the trough minimum were generally consistent at about 2 to 3 TECU, while the depth of the trough was much more dependent on Kp in the evening hours than after midnight. The trough half-width on the equatorward side of the minimum showed greater variability than the corresponding parameter on the poleward side. Figure 3-14 gives a sample of the results showing the median trough profiles plotted from the defined parameters for conditions appropriate to a mid-range of geomagnetic activity, with Kp between 3- and 4-. Corresponding plots were also obtained for low and high Kp (Pryse et al., 2006b). It can be seen from Figure 3-14 that the trough retains a notch-like shape throughout most of the night for geomagnetic activity in the mid-Kp range. The gradient of the equatorward wall becomes less steep at later times with the ionisation at the mid-latitudes decreasing during the night. The poleward wall is often steeper than that on the equatorward side of the minimum and is usually surmounted by a boundary blob maximum. The parameters used in this study have been defined in such a way that the experimental results from the study can be compared directly with the output of models. Validation of empirical and parameterised models of the ionosphere, developed for the mitigation of propagation effects in radio systems applications is of importance in the vicinity of the main trough. Few current models attempt to replicate the trough and, for those that do, getting the trough in the wrong place or with the wrong shape may simply confound the problem.

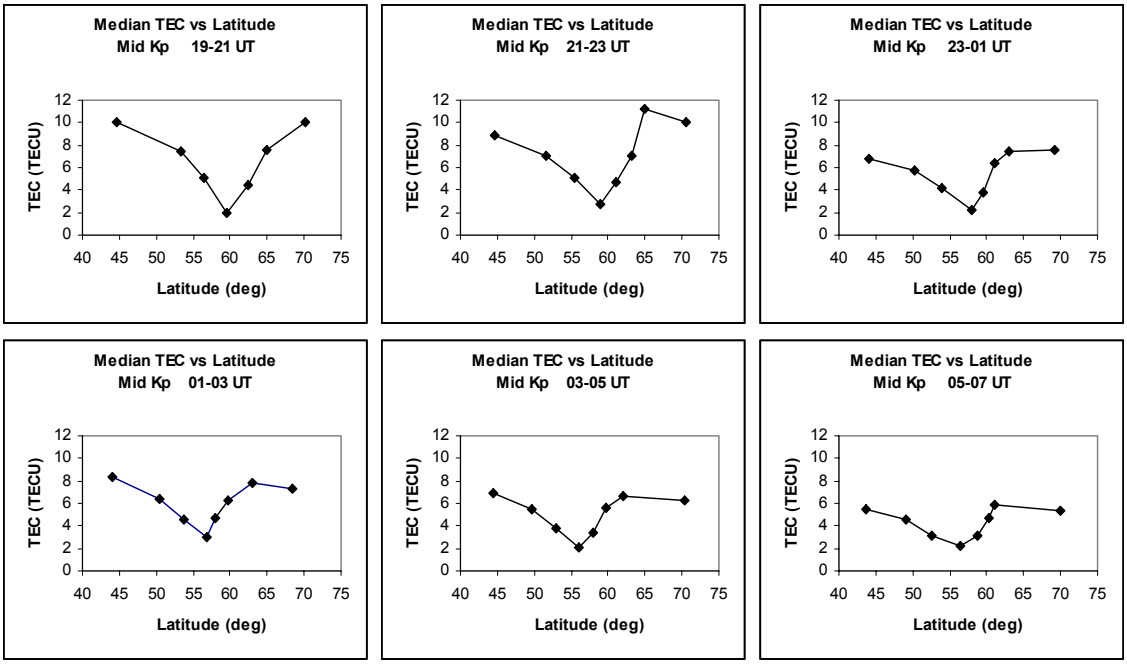

Figure 3-14: Median TEC versus Median Latitude of the Trough Parameters for Mid-Range Kp, Obtained from Tomographic Observations in the UK between September 2002 and August 2003 (Pryse et al., 2006b).

3.2.7 Summary and Open Issues

Results have been summarised here from collaborative studies led by the University of Wales Aberystwyth into the spatial distribution of the ionospheric plasma at high latitudes. Observational evidence has been discussed in support of dayside ionisation being drawn by the convective flow into the polar cap. It was shown that with IMF B_z positive the dayside ionisation can be drawn around the periphery of a polar cap that is closed to the inflow of plasma. In addition, observations and modelling studies have demonstrated that polar cap plasma may be reconfigured on the nightside to form the poleward wall of the main ionisation trough. The ongoing experimental programme forms a basis for longer-term statistical studies of the polar and auroral ionospheres, of relevance to the development and

validation of physical and parameterised models of the regions. Definitive studies have been made in this respect on the form and location of the latitudinal structure of the main trough.

With the International Polar Year (IPY) imminent, it is now timely to consider the studies within a broader framework. The International Ionospheric Tomography Community has submitted an Expression of Intent that now forms part of the "Heliosphere impact on geospace" programme. The radio tomography programme comprises receiver chains in Alaska, Greenland, Scandinavia (polar and auroral) and Russia. A preliminary study reported by Kersley et al. (2005), using observations from the receiver chains in Alaska, Greenland and Scandinavia, illustrated the potential of multi-chain tomography for near-simultaneous observations in different longitude sectors opening the way for longer term studies.

Several specific issues that remain to be addressed include:

- ***Origin of enhanced plasma on the dayside***

Where does the plasma build-up? What is the role of the combined effects of the high-latitude convection and co-rotation flow in retaining plasma in sunlight for an extended time period?

- ***Mechanisms of entrainment of plasma into the high-latitude convection pattern***

Does this form a continuous tongue of ionisation? Alternatively, is it influenced by magnetic reconnection that creates a succession of patches at sub-polar latitudes as proposed by Moen et al. (2006)?

- ***Effect of nightside reconnection***

What is the effect of the closure of the geomagnetic field on the structure of the plasma flowing out of the polar cap on the nightside?

- ***Offset of the geomagnetic and geographic reference frame***

Do observational data support plasma of dayside origin being more prominent at nighttime in the European sector than the US sector? Is this the reason for most of the large SED events reported to date, of concern to GPS applications, originating in the US sector?

- ***Influence of plasma flow patterns under conditions of stable IMF B_z positive***

How does the flow pattern affect the spatial distribution of plasma at high latitudes? Can the flow pattern and the plasma distribution be modelled?

- ***Main ionisation trough***

What are the mechanisms that form and sustain the poleward wall of the trough on the nightside? Are these the same in different longitude sectors?

- ***Particle precipitation***

How does *in situ* electron density production by particle precipitation modulate the spatial distribution of the ionospheric plasma at auroral and polar latitudes?

3.2.8 Acknowledgements

Thanks are recorded to many past and present members of the Solar System Physics group at the University of Wales Aberystwyth (UWA), including Prof. L. Kersley, Dr. R W. Sims, D. Malan, K.L. Dewis and A.G. Wood, and acknowledgement is given for the contributions from co-workers world-wide in the collaborative investigations. The assistance of the University of Tromsø and the Norwegian Polar Research Institute in the experimental tomographic measurements is gratefully acknowledged. Funding

for the studies has come from the UK Particle Physics and Astronomy Research Council, the UK Radiocommunications Agency and NorthWest Research Associates Inc., USA.

3.2.9 References

Anderson, D.N., Buchau, J., and Heelis, R.A.: Origin of density enhancements in the winter polar cap ionosphere, Radio Sci., 23, 513-519, 1988.

Bowline, M.D., Sojka, J.J., and Schunk, R.W.: Relationship of theoretical patch climatology to polar cap patch observations, Radio Sci., 31, 635-644, 1996.

Buchau, J., Weber, E.J., Anderson, D.N., Carlson, Jr., H.C., Moore, J.G., Reinisch, B.W., and Livingston, R.C.: Ionospheric structures in the polar cap: their origin in relation to 250-MHz scintillation, Radio Sci., 20, 325-338, 1985.

Crowley, G.: Critical review of ionospheric patches and blobs, URSI Review of Radio Science 1993-1996, edited by: Stone, W. R., 619-648, 1996.

Cowley, S.W.H.: Excitation of flow in the Earth's magnetosphere-ionosphere system: observations by incoherent scatter radar, in Polar Cap Boundary Phenomena, eds. J. Moen et al., NATO Advanced Study Institute Series, Kluwer Academic Press, Dordrecht, The Netherlands, 509, 127-140, 1998.

Dungey, J.W.: Interplanetary magnetic field and auroral zones, Phys. Rev. Lett., 6 (2), 47-48, 1961.

Fuller-Rowell, T.J. and Rees, D.: A three-dimensional, time-dependent, global model of the thermosphere, J. Atmos. Sci., 37, 2545-2567, 1980.

Greenwald, R.A., Baker, K.B., Dudeney, J.R., Pinnock, M., Jones, T.B., Thomas, E.C., Villain, J.-P., Cerisier, J.-C., Senior, C., Hanuise, C., Hunsucker, R.D., Sofko, G., Koehler, J., Nielsen, E., Pellinen, R., Walker, A.D.M., Sato, N., and Yamagishi, H.: Darn/Superdarn: A global view of the dynamics of high-latitude convection, Space Sci. Rev., 71, 761-796, 1995.

Jones, D,G., Walker, I.K., and Kersley, L.: Structure of the poleward wall of the trough and the inclination of the geomagnetic field above the EISCAT radar, Ann. Geophysicae, 15, 740-746, 1997.

Kersley, L., Pryse, S.E., Denton, M.H., Bust, G., Fremouw, E., Secan, J., Jakowski, N., and Bailey, G.J.: Radio tomographic imaging of the northern high-latitude ionosphere on a wide geographic scale, Radio Sci., 40, RS5003, doi: 10.1029/2004RS003103, 2005.

Lockwood, M.: Identifying the open-closed field line boundary, in Polar Cap Boundary Phenomena, eds. J. Moen et al., NATO Advanced Study Institute Series, Kluwer Academic Press, Dordrecht, The Netherlands, 509, 73-90, 1998.

McEwen, D.J., and Harris, D.P.: Occurrence patterns of F layer patches over the north magnetic pole, Radio Sci., 31, 619-628, 1996.

Middleton, H.R., Pryse, S.E., Dewis, K.L., Wood, A.G., and Balthazor, R.: Signatures of space weather processes in the northern polar ionosphere: Radio Tomography and the CTIP model, 2nd European Space Weather Week: ESWW-II, ESA-ESTEC, Noordwijk, The Netherlands, November 2005a (poster).

Middleton, H.R., Pryse, S.E., Kersley, L., Bust, G.S., Fremouw, E.J., Secan, J.A., and Denig, W.F.: Evidence for the tongue of ionisation under northward IMF conditions, J. Geophys. Res., 110(A7), A07301 10.1029/2004JA010800, 2005b.

Moen, J., Carlson, H.C., Oksavik, K., Nielsen, C.P., Pryse, S.E., Middleton, H.R., McCrea, I.W., and Gallop, P.: EISCAT observations of plasma patches at sub-auroral cusp latitudes, Ann. Geophysicae, 24(9), 2363-2374, 2006.

Pryse, S.E.: Radio tomography: A new experimental technique, Surveys in Geophysics, 24, 1-38, 2003.

Pryse, S.E., Sims, R.W., Moen, J., Kersley, L., Lorentzen, D., and Denig, W.F.: Evidence for solar-production as a source of polar-cap plasma, Ann. Geophsyicae, 22, 1093-1102, 2004.

Pryse, S.E., Dewis, K.L., Balthazor, R.L., Middleton, H.R., and Denton, M.H.: The dayside high-latitude trough under quiet geomagnetic conditions: Radio tomography and the CTIP model, Ann. Geophysicae, 23(4), 1199-1206, 2005.

Pryse, S.E., Wood, A.G., Middleton, H.R., McCrea, I.W., and Lester, M.: Reconfiguration of polar-cap plasma in the magnetic midnight sector, Ann. Geophysicae, 24(8), 2201-2208, 2006a.

Pryse, S.E., Kersley, L., Malan, D., and Bishop, G.J.: Parameterization of the main ionospheric trough in the European sector, Radio Sci., 41, RS5S14, doi:10.1029/2005RS003364, 2006b.

Quegan, S., Bailey, G.J., Moffett, R.J., Heelis, R.A., Fuller-Rowell, T.J., Rees, D. and Sprio, R.W.: A theoretical study of the distribution of ionisation in the high-latitude ionosphere and the plasmasphere: first results on the mid-latitude trough and the light-ion trough, J. Atmos. Terr. Phys., 44, 619-640, 1982.

Reiff, P.H., and J.L. Burch, IMF By-dependent plasma flow and Birkeland currents in the dayside magnetosphere: 2. A global model for northward and southward IMF, J. Geophys. Res., 90 (NA2), 1595-1609, 1985.

Rishbeth, H., and Williams, P.J.S.: The EISCAT ionospheric radar: the system and early results, Q. J. R. Astr. Soc., 26, 478-512, 1985.

Robinson, R.M., Tsunoda, R.T., and Vickrey, J.F.: Sources of F-region ionisation enhancements in the nighttime auroral zone, J. Geophys. Res., 90, 7533-7546, 1985.

Rodger, A.S., Pinnock, M., Dudeney, J.R., Baker, K.B., and Greenwald, R.A.: A new mechanism for polar patch formation, J. Geophys. Res., 99, 6425-6436, 1994.

Ruohoniemi, J.M., and Baker, K.B.: Large-scale imaging of high-latitude convection with Super Dual Auroral radar Network HF radar observations, J. Geophys. Res., 103, 20797-20806, 1998.

Sims, R.W., Pryse, S.E., and Denig, W.F.: Spatial structure of summertime ionospheric plasma near magnetic noon, Ann. Geophysicae, 23, 25-37, 2005.

Sojka, J.J., Bowline, M.D., Schunk, R.W., Decker, D.T., Valladares, C.E., Sheehan, R., Anderson, D.N., and Heelis, R.A.: Modelling polar-cap F-region patches using time-varying convection, Geophys. Res. Lett., 20, 1783-1786, 1993.

Valladares, C.E., Basu, S., Buchau, J., and Friis-Christensen, E.: Experimental evidence for the formation and entry of patches into the polar cap, Radio Sci., 29, 167-194, 1994.

Weber, E.J., Buchau, J., Moore, J.G., Sharber, J.R., Livingston, R.C., Winningham, J.D., and Reinisch, B.W.: F-layer ionization patches in the polar cap, J. Geophys. Res., 89, 1683-1694, 1984.

3.3 THE ELECTRON DENSITY ASSIMILATIVE MODEL (EDAM)

(M. J. Angling, QinetiQ, St. Andrew's Road, Malvern, Worcs, WR14 3PS, UK.)

3.3.1 Introduction

The last 15 years have seen a rapid growth in the development and use of ionospheric imaging systems. Traditional tomographic imaging techniques represent the ionosphere by means of a grid of pixels. Then, in the case of an integrated measurement, such as GPS TEC, the ith observation can be modelled by the sum of the electron density in the jth pixel (x_j) multiplied by the ray length within the jth pixel (H_{ij}) (Figure 3-15):

$$y_i = \sum_{j=1}^{n} H_{ij} x_j \tag{1}$$

or, in matrix notation:

$$\mathbf{y} = \mathbf{H}\mathbf{x} \tag{2}$$

where **H** is known as the observation operator, **x** is the rasterised representation of the ionosphere and **y** is the TEC.

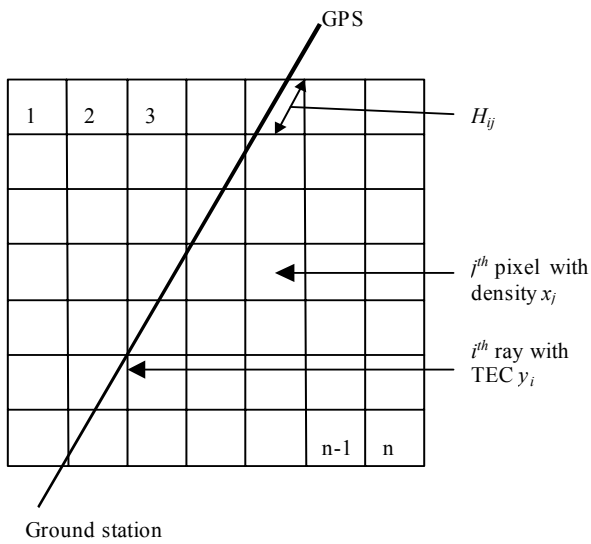

Figure 3-15: Diagram Illustrating the Construction of the Observation Operator that Relates a Slant TEC Measurement to a Pixel Representation of the Ionosphere.

It can be seen that this formulation of the imaging problem is entirely general and can, therefore, be easily extended to a 3D grid of voxels. Furthermore, there is no requirement that the slant TEC must be measured by a ground station, and consequently it is also simple to directly include measurements of TEC made in low earth orbit. The disadvantage of moving from 2D to 3D imaging is that a very large amount of data is required to be able to operate the traditional tomographical methods. In practice, and especially for GPS data (where the satellites are slow moving), the required quantity of data is not available, and other, more sophisticated, methods must be used. These methods must use *a priori* data to constrain the inversion from slant TEC to the electron density image. This *a priori* data may be a model of the ionosphere, or may take the form of assumptions about how the ionosphere can be decomposed into a set of basis functions.

Ideally, a 3D imaging system will use data provided by a range of ionospheric measurement techniques. Of particular note is data from the International GNSS Service (IGS) receiver network (Beutler et al., 1999). Many IGS stations provide data in hourly files with low latency (~90 minutes), which can be used to calculate slant total electron content (TEC). Radio occultation (RO) methods are also being increasingly investigated. RO measurements are made by monitoring transmissions from GPS satellites using receivers on Low Earth Orbiting (LEO) satellites and provide the potential of measuring refractivity profiles in regions where ground based sensors cannot easily be located, such as deep sea waters. The recent launch of RO instruments on the Constellation Observing System for Meteorology, Ionosphere & Climate (COSMIC) six satellite constellation has the potential to provide a large amount of ionospheric data (Hajj et al., 2000); again this will be available with a low latency (115 minutes). For both ground and space based data, data assimilation provides an optimal way of combining slant TEC measurements with an ionospheric model to provide a full 3D representation of the ionospheric electron density.

3.3.2 The Electron Density Assimilative Model

The Electron Density Assimilative Model (EDAM) has been developed (Angling and Cannon, 2004; Angling and Khattatov, 2006) to assimilate measurements into a background ionospheric model. This model is provided by PIM (Daniell et al., 1995) and the majority of the input data is GPS TEC derived from IGS stations. The assimilation is based on a weighted, damped least mean squares estimation. This is a form of minimum variance optimal estimation (also referred to as best linear unbiased estimation, BLUE) that provides an expression for an updated estimation of the state (known as the analysis) that is dependent upon an initial estimate of the state (the background model), and the differences between the background model and the observations (Menke, 1989). The error covariance matrices of the background model and the observations are also included to control the relative contributions of the background and the observations to the analysis:

$$\mathbf{x_a} = \mathbf{x_b} + \mathbf{K}(\mathbf{y} - \mathbf{H}\mathbf{x_b}) \tag{3}$$

$$\mathbf{K} = \mathbf{B}\mathbf{H}^{\mathbf{T}}\left(\mathbf{H}\mathbf{B}\mathbf{H}^{\mathbf{T}} + \mathbf{R}\right)^{-1} \tag{4}$$

where $\mathbf{x_a}$ is the analysis, $\mathbf{x_b}$ is the background model, **K** is the weight matrix, **y** is the observation vector, **B** is the background error covariance matrix, and **R** is the error covariance matrix of the observations (Rodgers, 2000). **H** is the observation operator that relates the measurements to the state:

$$\mathbf{y} = \mathbf{H}\mathbf{x} + \boldsymbol{\varepsilon} \tag{5}$$

where $\boldsymbol{\varepsilon}$ is the observation error. The analysis error covariance matrix (**S**) may also be calculated thus:

$$\begin{aligned} \mathbf{S} &= \mathbf{B} - \mathbf{B}\mathbf{H}^{\mathbf{T}}\left(\mathbf{H}\mathbf{B}\mathbf{H}^{\mathbf{T}} + \mathbf{R}\right)^{-1}\mathbf{H}\mathbf{B} \\ \mathbf{S} &= \mathbf{B} - \mathbf{K}\mathbf{H}\mathbf{B} \end{aligned} \tag{6}$$

The assimilation is conducted using a magnetic coordinate system that remains fixed in space with respect to the sun. An assimilation time step of 15 minutes has been used and the electron density differences between the voxels of the analysis and the background model are propagated from one time step to the next by assuming persistence combined with an exponential decay. The time constant for this decay is set at 4 hours. Thus if the data feed is interrupted, the analysis will decay back to the background model.

A typical set of input data sites is shown in Figure 3-16. IGS stations are represented by dots, whilst USAF ionosondes are shown as triangles.

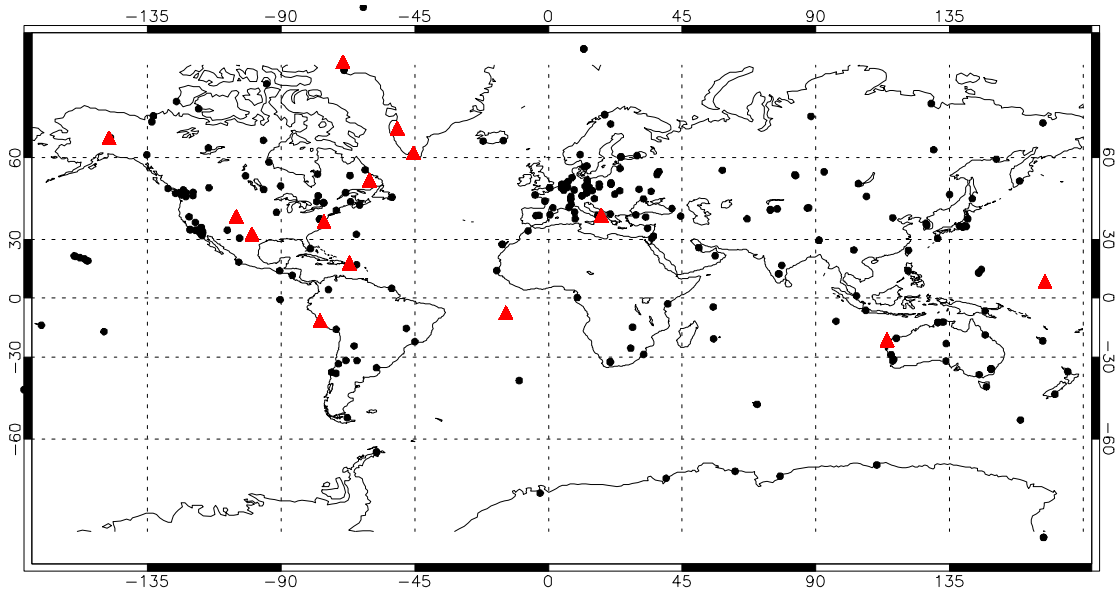

Figure 3-16: Map Showing Locations of IGS Stations (dots) and Vertical Ionosondes (triangles).

3.3.3 Testing

Testing has shown that, whilst the RMS errors in f_oF_2 may be reduced by the assimilative model (Figure 3-17), it is difficult to modify the vertical structure of the electron density grid using ground based TEC data alone (Figure 3-18) – this is a problem common to all assimilative approaches (Angling and Khattatov, 2006). It is anticipated that the introduction of RO data will provide much better vertical information and, therefore, improve the vertical representation of the ionosphere.

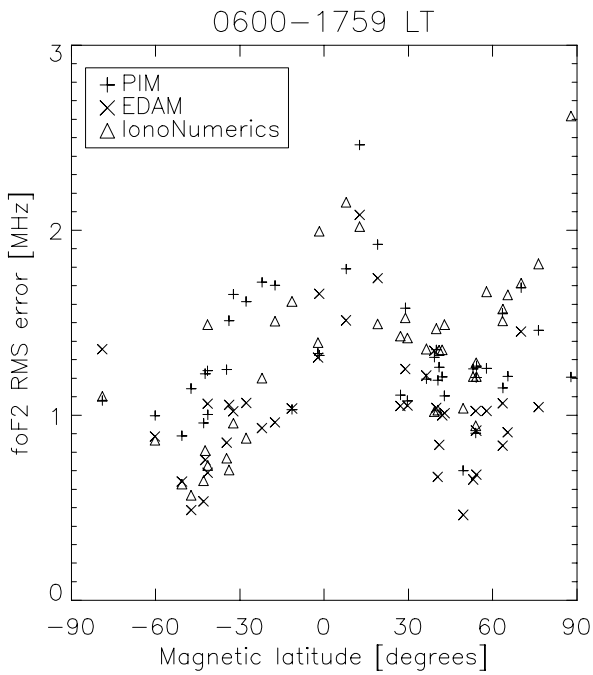

Figure 3-17: Daytime f_oF_2 RMS Error as a Function of Magnetic Latitude – from Angling and Khattatov, 2006.

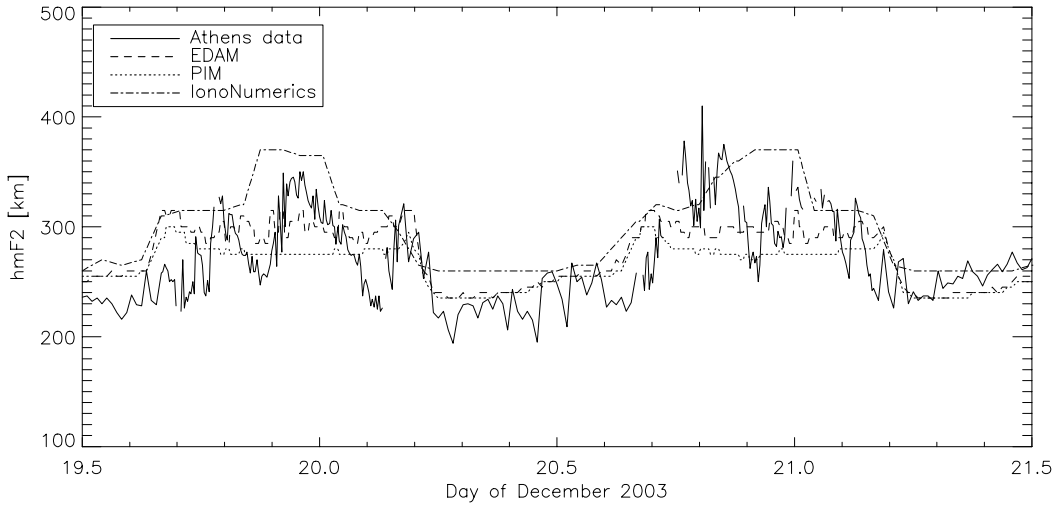

Figure 3-18: Example h_mF_2 Results for the Athens Ionosonde – from Angling and Khattatov, 2006.

Further testing has been undertaken using both ground based IGS data and space based data from COSMIC. For moderate (4/9/2006, Figure 3-19) and disturbed conditions (19-20/8/2006, Figure 3-20), EDAM generally performs better than PIM. As expected, the assimilation of the RO slant TEC data has the greatest impact on the assimilation results, though the improved RMS exhibited by EDAM ingesting just ground based IGS data does demonstrate that it is possible to reduce errors in the vertical structure of the ionospheric model using this data.

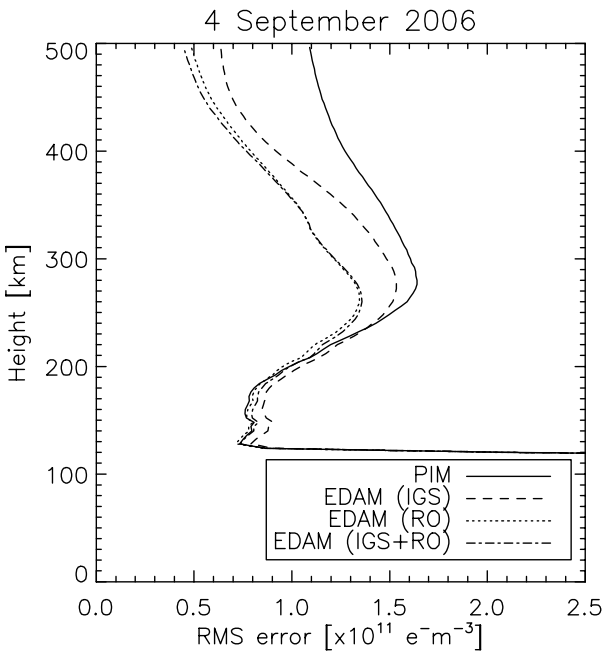

Figure 3-19: RMS Error between Ionospheric Models and Abel Transform Vertical Profiles at 5 km Height Steps on 4 September 2006. The models are: PIM (solid line); EDAM assimilating IGS data only (dashed line); EDAM assimilating COSMIC RO data only (dotted line); and EDAM assimilating IGS and COSMIC RO data (dot-dash line) – from Angling, 2007.

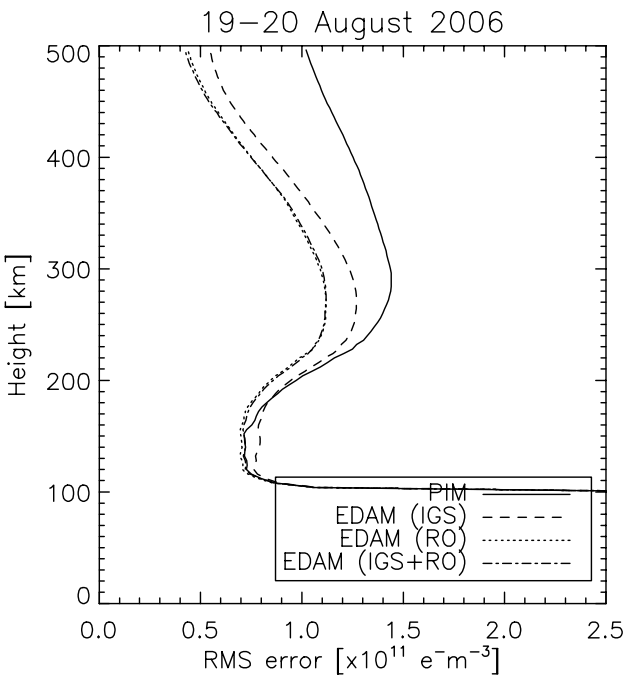

Figure 3-20: RMS Error between Ionospheric Models and Abel Transform Vertical Profiles at 5 km Height Steps on 19-20 August 2006. The models are: PIM (solid line); EDAM assimilating IGS data only (dashed line); EDAM assimilating COSMIC RO data only (dotted line); and EDAM assimilating IGS and COSMIC RO data (dot-dash line) – from Angling, 2007.

3.3.4 Conclusions

EDAM has been developed to provide an effective means for assimilating a range of difference ionospheric data types. Testing has demonstrated that EDAM can provide a better representation of the ionosphere than median models and that both ground and space based data are capable of improving the representation of the vertical structure of the ionosphere.

A number of other data assimilation models are in development or use. It would be greatly beneficial to have agreed data sets (i.e. of manually scaled ionograms) available to the community to facilitate comparative testing of these assimilative models.

3.3.5 Acknowledgements

EDAM has been developed under funding from the Operating Environment domain of the United Kingdom Ministry of Defence Corporate Science and Technology programme. IGS data was obtained from the IGS JPL and SOPAC Data Centres. Differential code biases were obtained from the Centre for Orbit Determination in Europe. Vertical ionosonde data was provided by the Air Force Research Laboratory and COSMIC data was provided by the COSMIC Data Analysis and Archive Centre.

3.3.6 References

Angling, M.J., First assimilations of COSMIC radio occultation data into the Electron Density Assimilative Model (EDAM), Submitted to Annales Geophysicae, 2007.

Angling, M.J., and P.S. Cannon, Assimilation of radio occultation measurements into background ionospheric models, Radio Science, 39 (RS1S08, doi: 10.1029/2002RS002819), 2004.

Angling, M.J. and B. Khattatov, Comparative study of two assimilative models of the ionosphere, Radio Science, 41, (RS5S20, doi: 10.1029/2005RS003372), 2006.

Belehaki, A. and L. Kersley, Statistical validation of a technique for estimating total electron content from bottomside ionospheric profiles, Radio Science, 41, (RS5003, doi: 10.1029/2005RS003433), 2006.

Beutler, G., M. Rothacher, S. Schaer, T.A. Springer, J. Kouba, and R.E. Neilan, The International GPS Service (IGS): An Interdisciplinary Service in Support of Earth Sciences, Adv. Space Res. Vol. 23, No. 4, pp. 631-635, 1999.

Daniell, R. E. Jr., L. D. Brown, D. N. Anderson, M. W. Fox, P. H. Doherty, D. T. Decker, J. J. Sojka, R. W. Schunk, Parameterized ionospheric model: A global ionospheric parameterization based on first principles models, Radio Sci., 30(5), 1499-1510, 10.1029/95RS01826, 1995.

Hajj, G.A., L.C. Lee, X. Pi, L.J. Romans, W.S. Schreiner. P.R. Straus and C. Wang, COSMIC GPS Ionospheric Sensing and Space Weather, Special Issue of Terrestrial Atmos. Oceanic Sci., 11, 235-272, 2000.

Menke, W., Geophysical data analysis: discrete inverse theory, International Geophysics Series, San Diego, Academic Press, 1989.

Reinisch, B. W. and Huang, X.: Deducing topside profiles and total electron content from bottomside ionograms, Adv. Space Res., 27, 1, 23-30, 2001.

B.W. Reinisch, X. Huang, A. Belehaki, and R. Ilma, Using scale heights derived from bottomside ionograms for modelling the IRI topside profile, Advances in Radio Science, 2, 293-297, 2004.

Rodgers, C. D., Inverse methods for atmospheric sounding: theory and practice, Series on Atmospheric, Oceanic and Planetary Physics – Vol 2, World Scientific Publishing, 2000.

3.4 GPS SOUNDING OF THE IONOSPHERE ONBOARD CHAMP

(N. Jakowski, C. Mayer, V. Wilken, Deutsches Zentrum für Luft- und Raumfahrt (DLR) / Institut für Kommunikation und Navigation, Kalkhorstweg 53, Neustrelitz, Germany)

Abstract

Space based GPS measurements onboard Low Earth Orbiting (LEO) satellites provide a unique possibility for exploring the ionosphere on a global scale. Both the radio occultation measurements in the limb sounding mode and the navigation measurements using a zenith viewing GPS antenna provide the Total Electron Content (TEC) along numerous ray paths. TEC may effectively be used for reconstructing the spatial and temporal distribution of the electron density in the ionosphere and plasmasphere.

Reported are results obtained from radio occultation measurements on CHAMP which have provided more than 200,000 vertical electron density profiles so far. These observations contribute to a better understanding of the regular behaviour of the global ionosphere. Furthermore, the radio occultation measurements indicate irregular and/or wavelike structures in the ionosphere which may have severe impact on the functionality of radio systems.

A three-dimensional imaging of the electron density distribution near the CHAMP orbit plane between CHAMP and GPS orbit height is performed by using link related TEC data derived from dual frequency

navigation measurements onboard CHAMP. This type of measurements provides a good measure of the interaction of the solar wind with the global Earth's atmosphere, thus providing a good opportunity for studying this interaction via the magnetosphere.

Key words: GPS, Ionosphere, Plasmasphere, Radio Occultation, CHAMP.

3.4.1 Introduction

Innovative GPS based sounding techniques of the ionosphere have been established during the last decade. GPS receiver installed onboard Low Earth Orbiting (LEO) satellites have the capability to probe the ionosphere in the limb sounding mode (GPS radio occultation) and by using the navigation data for sounding the topside ionosphere / plasmasphere (see Figure 3-21).

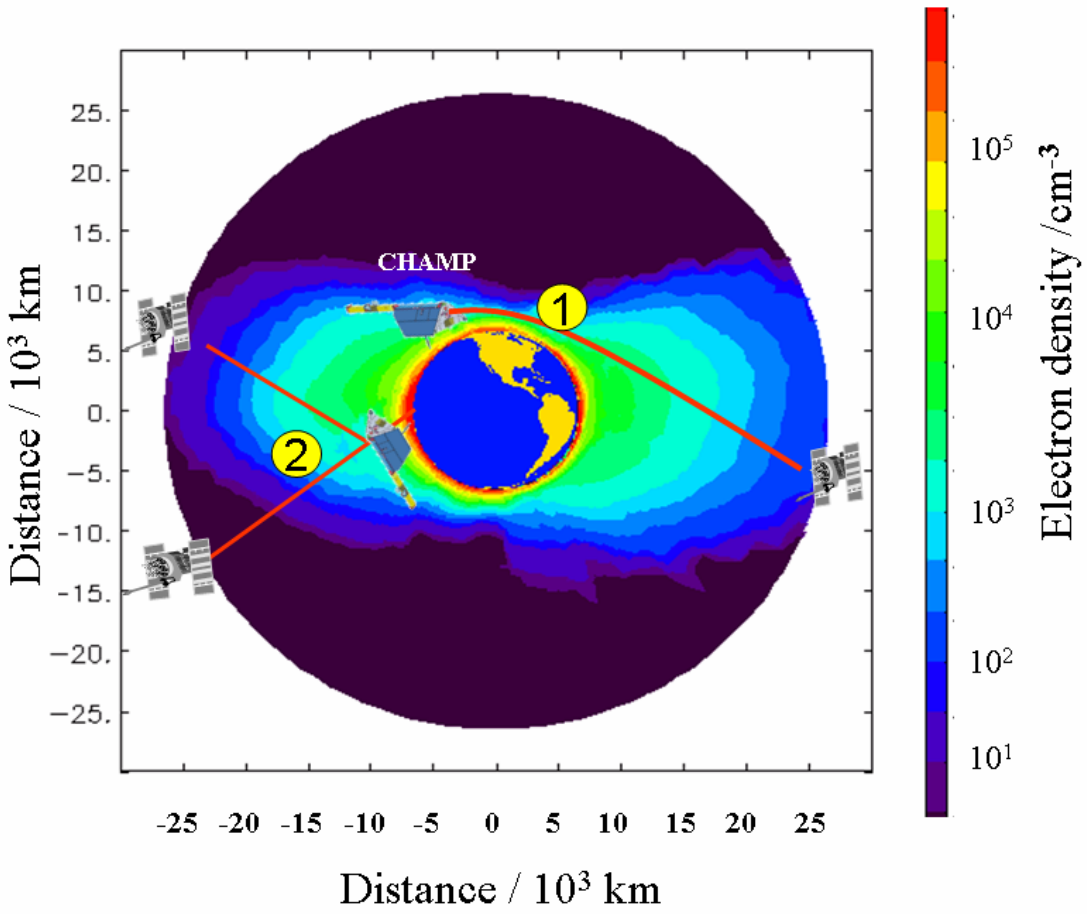

Figure 3-21: Illustration of GPS Measurement Techniques Used Onboard CHAMP for Sounding the Ionosphere – (1): Ionospheric radio occultation (IRO) measurements in the limb sounding mode; (2): Use of 0.1 Hz sampled GPS navigation data from the zenith viewing antenna.

The radio occultation technique enables the retrieval of the vertical refractivity profile of a planetary atmosphere travelled by an electromagnetic wave in the limb sounding geometry. Measured is the change of ray path bending, phase or signal strength of the radio wave while approaching the planetary surface until it is completely occulted by the planet (Eshleman, 1975).

Thus, planetary atmospheres from Mars and Venus were explored by radio communication link occultations of Mariner sondes IV (*Kliore et al., 1965*) and Venera 4, respectively.

VIKING and Voyager 1 tracking and telemetry signal occultations were used to explore the ionospheres of Mars (Breus et al., 1998) and Titan (Bird et al., 1997).

In the late 1980's, when the occultation science possibilities of GPS were recognized, it was proposed to apply the radio occultation technique also to the Earth's atmosphere sounding using the L-band signals of the global positioning system GPS that was just established (*e.g. Yunck et al., 1988*). To proof this concept, the GPS/MET experiment onboard the Microlab 1 satellite mission led by the University Corporation of Atmospheric Research (UCAR) was launched in April 1994 (*e.g. Ware et al., 1996*). The GPS/MET results have demonstrated that the GPS radio occultation technique is a powerful tool for remote sensing of the Earth's neutral atmosphere and ionosphere (e.g. Kursinski et al., 1997, Hajj and Romans, 1998, Hocke and Igarashi, 2002). Consequently, several satellite missions have flown with GPS radio occultation receivers such as OERSTEDT (Escudero et al., 2001), CHAMP [Reigber et al, 2000, Jakowski et al., 2002, Garcia-Fernandez et al., 2003], and SAC-C. Since future missions will also use the signals from other Global Navigation Satellite Systems (GNSS) such as GLONASS and GALILEO, the following text refers to GNSS only.

If a GNSS receiver is installed onboard a LEO satellite, the received signals are usually used for orbit positioning and for deriving a precise board time to which the measurements are referenced. The reception of dual frequency signals from GNSS satellites at another satellite principally enables determining the total electron content between both satellites for estimating the ionosphere/plasmasphere state (e.g. Jakowski and Bettac**,** 1994). If the receiver is flying on a LEO satellite, the sounding covers the volume between the satellite orbit and the GNSS orbit height at about 20000 km. Using CHAMP navigation data this innovative technique has been at first applied by Heise et al. (2002). The 0.1 Hz sampled navigation data, measured with the zenith viewing antenna were effectively used for reconstructing the topside ionosphere in the vicinity of the satellite orbit plane.

For demonstrating the capabilities of both techniques as illustrated in Figure 3-21, results of the ionosphere monitoring obtained onboard the current geo-research satellite mission CHAMP (Reigber et al., 2000) are discussed. The German CHAMP (CHAllenging Minisatellite Payload) satellite was successfully launched on 15 July 2000 into a near polar orbit (inclination 87°, altitude 450 km).The satellite is equipped with a dual frequency «Black Jack» GPS receiver which enables not only the use of GPS radio occultation measurements in the limb sounding mode, but also the analysis of the 0.1 Hz sampled navigation data.

The GPS data measured onboard CHAMP are received at the DLR Remote Sensing Data Center in Neustrelitz and subsequently processed at DLR by an operational data processing system (Wehrenpfennig et al., 2001).

3.4.2 GPS Measurement Techniques

3.4.2.1 Ionospheric Radio Occultation Measurements

The radio occultation measurements rely principally on accurate measurements of the GNSS signal phases onboard a Low Earth Orbiting (LEO) satellite. The so-called phase path excess can then be used to derive the bending angle of the ray path or to determine the Total Electron Content (TEC) along the measured radio link. This measurement is the basis for retrieving the vertical refractivity profile from the LEO orbit height down to the Earth surface. Since the index of refractivity of the ionosphere depends mainly on the number of free electrons, the inversion of the measured signals can provide the vertical electron density profile (e.g. Hajj and Romans, 1998, Schreiner et al., 1999, Jakowski et al., 2002a).

The well known scheme of radio occultation is shown in Figure 3-22. The refraction angle α, between the ray path asymptotes can be derived from the GNSS carrier phase measurements onboard the LEO satellite with high accuracy. Since the bending angle is principally less than one degree, the orbit data are required with high precision (centimeter range) and clock drifts have precisely to be removed.

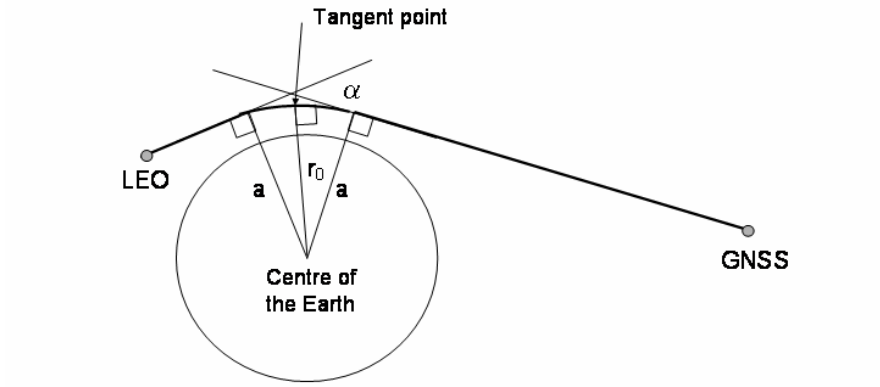

Figure 3-22: Principal GNSS Radio Occultation Geometry for Retrieving the Vertical Electron Density Profile of the Ionosphere.

Introducing the impact or approaching parameter $a = n \cdot r$ that describes the refractive distance of the asymptotic ray path from the centre of the Earth, the refraction angle α can be expressed by the refraction index n via the integral equation

$$\alpha(a) = -2a \int_{r_0}^{\infty} \frac{1}{\sqrt{r^2 n^2 - a^2}} \frac{d\ln(n)}{dr} dr \,. \tag{1}$$

This integral equation can then be inverted by the Abel integral transform providing the vertical profile of the refractive index in terms of α and a (cf. Fjeldbo et al. 1971).

Thus, measuring the bending angle α at the refractive distance a from the satellite orbit height down to the bottom of the ionosphere, one can retrieve the vertical refractivity profile.

Taking into account L-band signal frequencies of GNSS, the refractive index can be approximated by:

$$n^2 = 1 - K \frac{n_e}{f^2} \tag{2}$$

with K= 80.6 m^3s^{-2}, where n_e is the local electron density and f is the radio wave frequency (Davies, 1990).

Thus, inverting the integral equation (1), the vertical electron density profile below the satellite orbit height may be derived.

Oppositely to the radio occultation sounding of the neutral atmosphere, the Ionospheric Radio Occultation (IRO) measurements can take advantage of the dispersive nature of the ionosphere. Thus, differential GNSS phases derived from dual frequency GNSS measurements can effectively be used to compute the integral of the electron density along the ray path which is commonly well known as the slant Total Electron Content (TEC) of the ionosphere.

The dual frequency measurement principle is the same as applied to ground based GNSS measurements for ionospheric monitoring (e.g. Wilson et al. 1995, Jakowski, 1996).

The GPS receiver onboard CHAMP measures carrier phases in the radio occultation or limb sounding mode starting at CHAMP orbit tangential heights down to the Earth surface with a sampling rate of 1 Hz.

The dual frequency based IRO retrieval method uses only the carrier phase measurements at L_1 and L_2 GPS frequencies which are described by the observation equation:

$$\phi = \rho + c(dt - dT) - d_I + d_{MP} + dq + dQ + N\lambda + \varepsilon \tag{3}$$

where ρ is the true geometrical range between GPS satellite and receiver, c is the vacuum speed of light, dt and dT are the satellite and receiver clock errors, d_I is the ionospheric delay along the ray path s, d_{MP} is the multipath error, dq and dQ are the instrumental satellite and receiver biases, λ is the radio wave length, N is the phase ambiguity number (integer) and ε is the residual error. The space weather sensitive ionospheric propagation term d_I is a function of the refraction index and can be written as:

$$d_I = \frac{K}{2f^2}\int_S^R n_e ds \tag{4}$$

Here the integral of the local electron density n_e along the ray path between satellite S and receiver R is the Total Electron Content already mentioned above. Ignoring the multipath term, instrumental delays and integer ambiguities N in eq. (3), the differential carrier phases $\Delta\phi = \phi_1 - \phi_2$ computed from carrier phase measurements at L1 and L2 frequencies provide low noise TEC values as a function of the tangential height. Applying this method, dispersive ray path bending effects can be commonly ignored because these effects are small compared with the first-order-effects (Schreiner et al., 1999). The 1 Hz sampled relative TEC is measured along the radio occultation ray path which continuously approaches to the Earth surface measured by the tangential height.

The obtained measurements form a set of equations which are successively solved from top to down, to provide the electron density while assumed spherically stratified ionosphere (Jakowski et al., 2002).

Since CHAMP has a rather low, even further decreasing orbit height of less than 450 km, the upper boundary condition is ill posed. This is due to a rather high plasma density above the occultation entry. To overcome this upper boundary problem, a specific model assisted technique has been developed. The solution starts with the first measurement at the greatest tangential height by using an adaptive model for the topside ionosphere and plasmasphere above the CHAMP orbit height. The model is based on a Chapman layer function and an exponentially decaying term representing the plasmasphere. Model parameters such as the plasma scale height at the upper boundary are determined in a few iterations in order to ensure a smooth transition between model values and measurements (Jakowski et al., 2002).

To fulfill space weather monitoring requirements, i.e. to come up with retrieval products within a latency of less than 3 hours as it is required by the traditional weather service, no further data are included in the retrieval procedure and for reasons of simplicity a spherically layered ionosphere is assumed (Abel inversion assumption). The retrieval can be improved if additional information, e.g. on horizontal gradients or local densities, as may be provided by TEC maps (e.g. http://www.kn.nz.dlr.de/daily/tec-eu). On average, from about 200 IRO measurements per day, about 150 electron density profiles are successfully retrieved (Figure 3-23) now adding up to the huge number of more than 200,000 profiles.

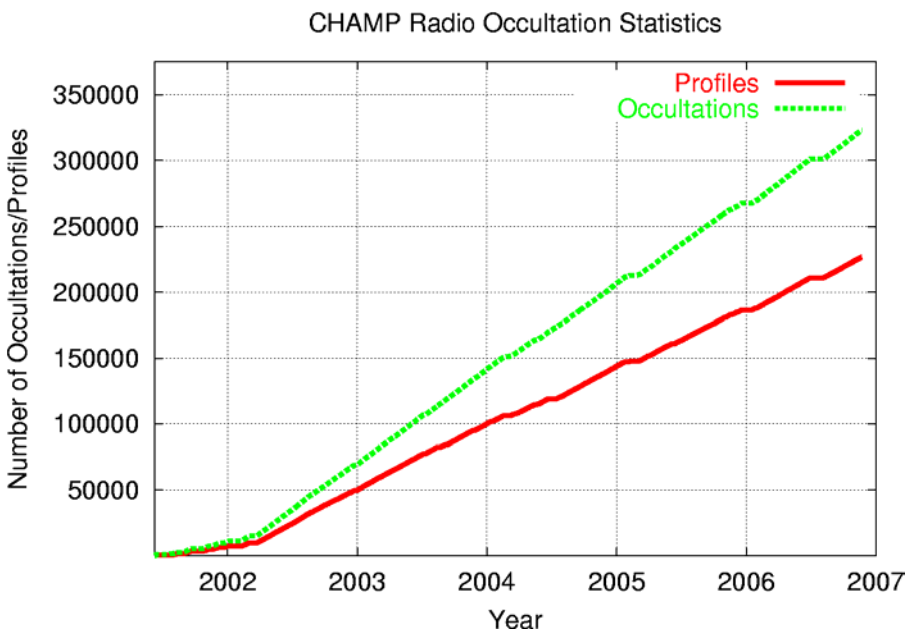

Figure 3-23: Number of IRO Measurements and Retrieved Vertical Electron Density Profiles from 11 April 2001 until November 2006.

Because the processing system works automatically (Wehrenpfennig et al., 2002), the occurrence of outliers in the derived profiles cannot be avoided; however, the number of such outliers is less than 1%.

As Figure 3-24 shows, the measurements are obtained from all geographic zones, thus well suited to get global information on the actual state of the ionosphere in the context of the space weather development. Due to the nearly sun synchronized orbit of CHAMP the local time sector is slowly shifting from day to day within a repetition period of about 130 days.

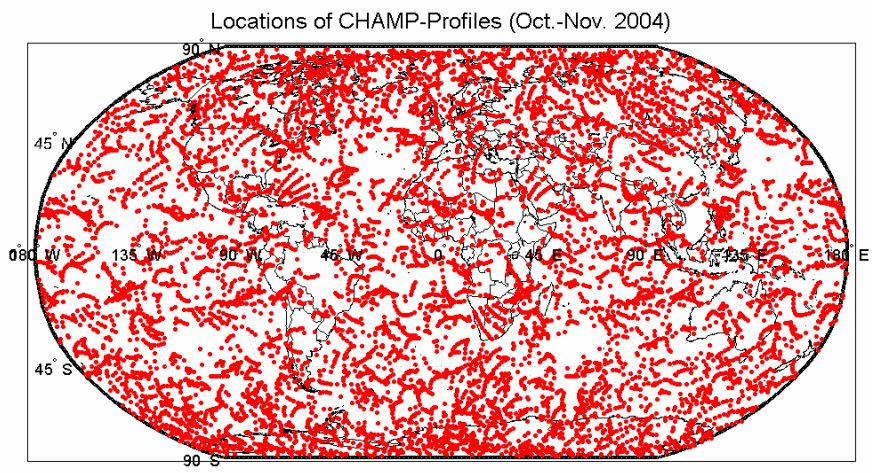

Figure 3-24: Locations of Retrieved Radio Occultation Profiles during Two Months (October – November 2004).

A typical product obtained after automatic retrieval of IRO measurements onboard CHAMP at 48.93 °S; 128.76°E over the Pacific Ocean around local noon is shown in Figure 3-25. The corresponding data files can be downloaded via the DLR space weather service (http://w3swaci.dlr.de).

To estimate the quality of the derived electron density profiles, a number of validation efforts were undertaken including ionosonde data from the European vertical sounding stations Juliusruh (54.6°N; 13.4°E), Athens (38.0°N; 23.5°E), Rome (41.9°N; 12.5°E), Tortosa (40.8°N; 0.5°E) and Dourbes (50.1°N; 4.6°E) (Jakowski et al., 2005a).

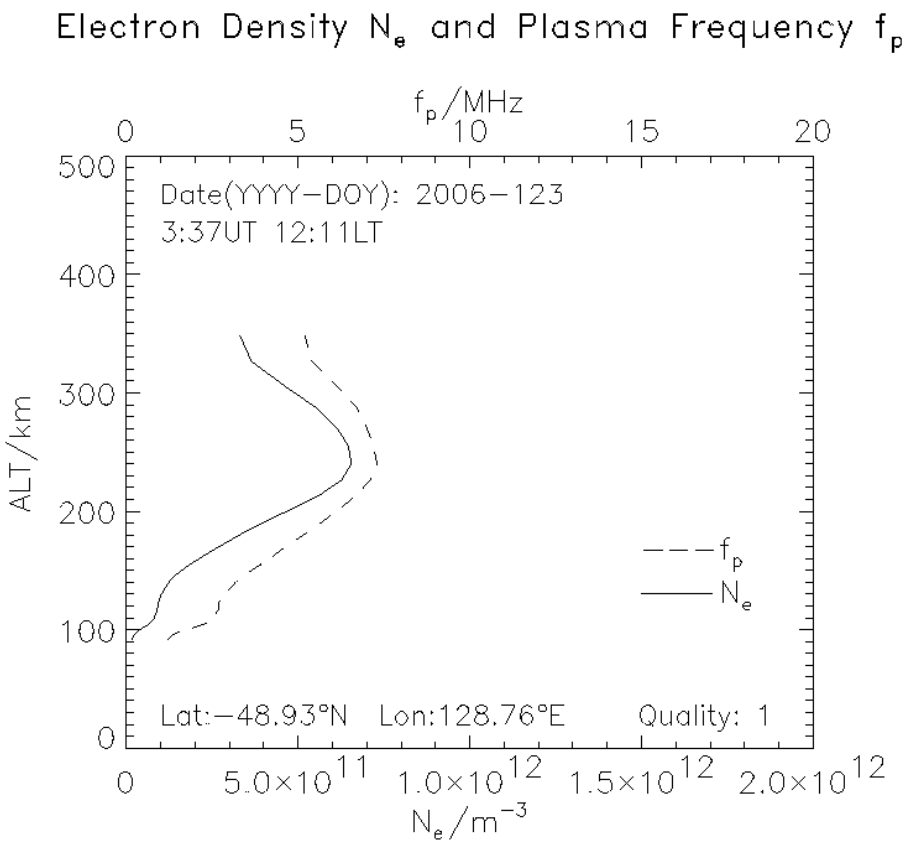

Figure 3-25: Data Product Sample Showing the IRO Retrieval of Vertical Electron Density Profiles Provided by the SWACI Service.

To give an impression of the achieved accuracy, the validation with ionograms of the Juliusruh ionosonde station has indicated a bias of up to 0.5 MHz and a RMS error of about 1 MHz in the plasma frequency (Jakowski et al., 2004, 2005a). More validation work is required in particular for low latitude data. Principally, it has to be stated that the IRO derived electron density profiles provide a unique measure describing the mean vertical electron density structure in comparably large areas with characteristic lengths of about 1000 km.

3.4.2.2 Topside Ionosphere / Plasmasphere Measurements

Whereas the IRO retrieval technique can work with non-calibrated carrier phase derived TEC data (Jakowski et al. 2002), the topside assimilation reconstruction technique requires calibrated TEC data along the numerous radio links between the GPS satellites and the topside GPS antenna onboard CHAMP (Figure 3-26). Depending on the relative CHAMP-GPS satellite constellation the data coverage changes permanently. Usually the data are not homogeneously distributed as Figure 3-26 demonstrates. To overcome this problem, the reconstruction is made via data assimilation into a reliable background electron density model.

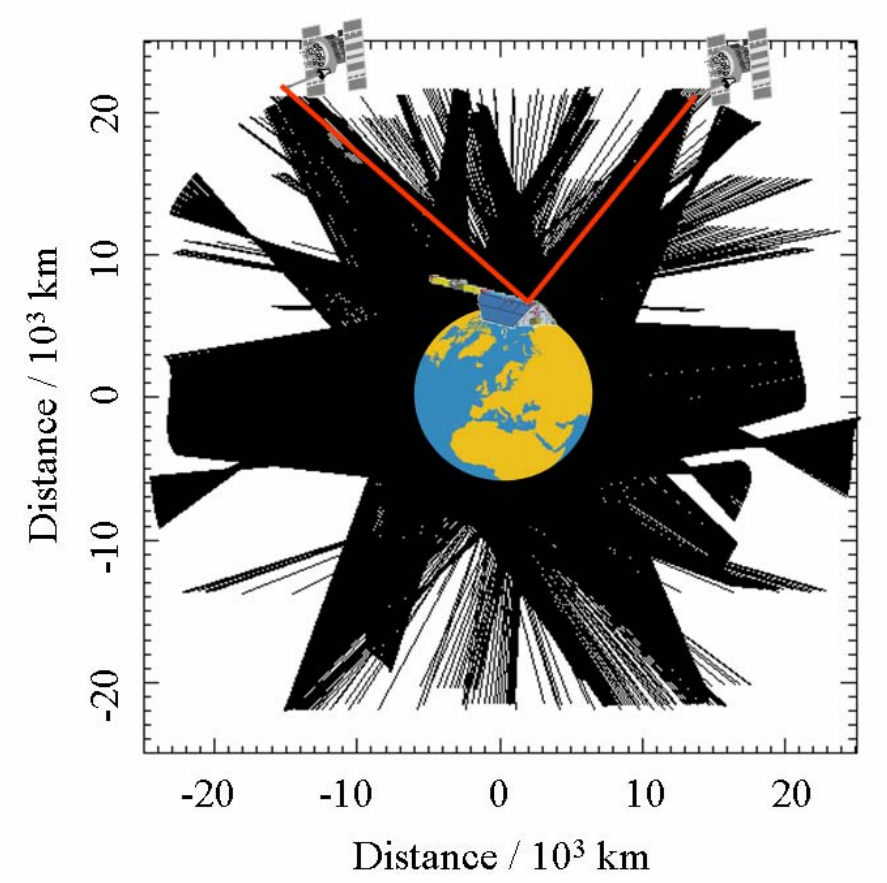

Figure 3-26: Illustration of the Topside Radio Link Distribution in the CHAMP Orbit Plane to the Visible GPS Satellites during One Satellite Revolution.

Before starting the reconstruction, the corresponding satellite and receiver biases (eq. 1) have to be estimated properly before the assimilation procedure can be started.

During the pre-processing stage, detected outliers are being removed and cycle slips are corrected. For reconstructing the topside ionosphere/plasmasphere electron density the Parameterized Ionospheric Model PIM (Daniell et al., 1995) has been selected to act as the background model. After calibrating the differential phases, the absolute TEC data are assimilated into the PIM model by a method described by Heise et al. (2002). The assimilation results provide a 3D reconstruction of the electron density for each CHAMP revolution in the vicinity of the CHAMP orbit plane.

Validation of the derived electron density distribution was made with in situ plasma density measurements of the Planar Langmuir Probe installed onboard CHAMP and incoherent scatter measurements at different sites. Compared with the Langmuir Probe data the assimilation results have no significant bias and agree within a standard deviation of $2 \times 10^{11} m^{-3}$ (Heise et al., 2002). Good agreement was also found with topside profiles deduced from incoherent scatter measurements.

As Figure 3-27 demonstrates, the global view on the Earth's plasma environment enables the study of magnetospheric-ionospheric coupling processes. Here, the compression of the plasmasphere at the day-side and the enlarged extension of the plasmasphere at the night-side are clearly visible. Thus, it becomes evident that this type of space based GPS measurements can provide essential contributions to a space weather monitoring of the ionosphere.

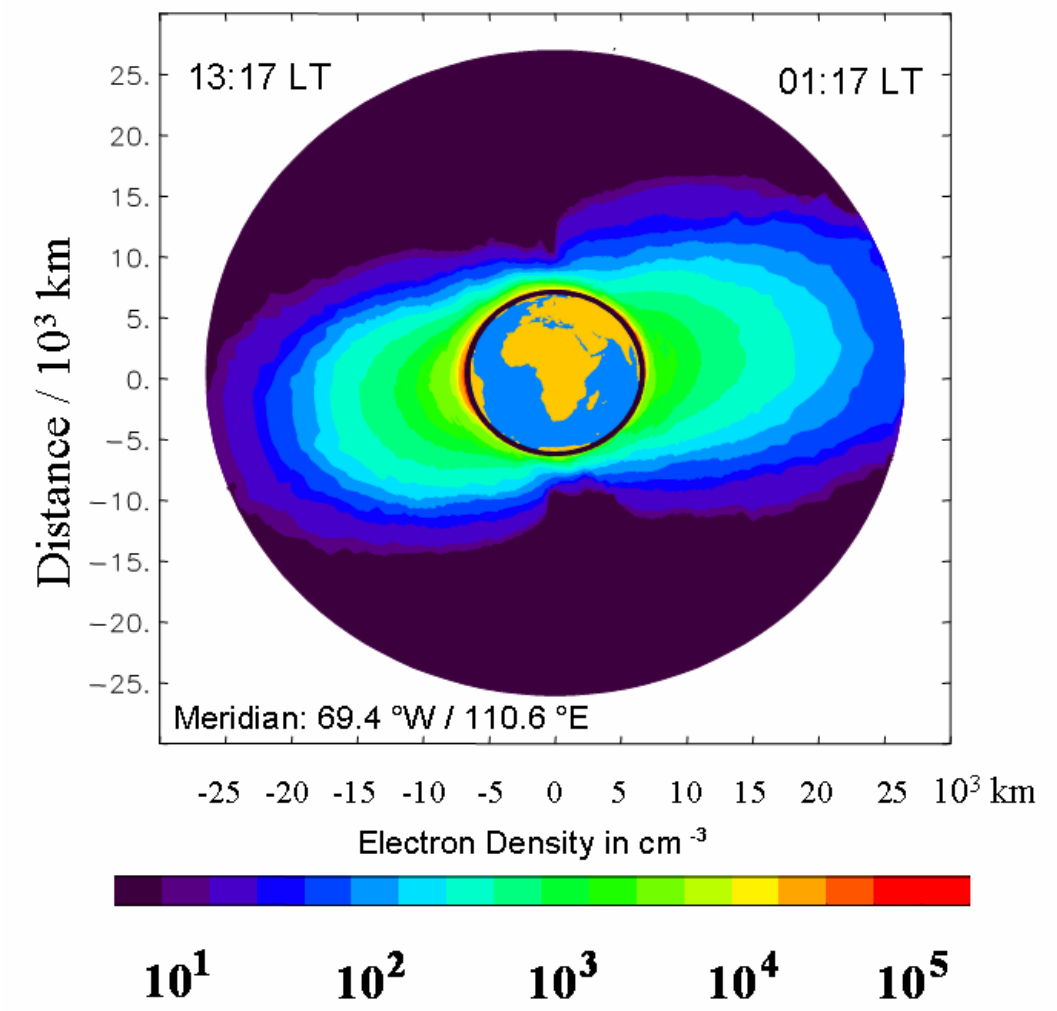

Figure 3-27: Reconstruction of the Electron Density Distribution of the Topside Ionosphere Based on GPS Data Received Onboard CHAMP.

The reconstruction is based on medians obtained for 21:00 UT over 10 consecutive days in August 2005. Thus, the right side shows the ionosphere/plasmasphere shortly after midnight whereas the left side represents ionosphere shortly after noon.

3.4.3 Observation Results and Discussion

Global data coverage and the huge amount of more than 200000 electron density profiles allow efficiently studying global large scale ionospheric processes. Because the first data were obtained in 2001 solar activity dependent effects can be studied.

As for the terrestrial weather at the Earth's troposphere, also the ionosphere is mainly controlled by the intensity of the solar radiation and its angle of incidence. Since the ionization is essentially produced by the solar ultraviolet radiation of wavelengths shorter than 130 nm, there is a strong solar cycle variation of the ionospheric peak density and other parameters related to the structure of the thermosphere/ionosphere. The solar activity control of the ionization level, well-known from TEC-measurements (e.g. Jakowski et al., 1991) is clearly visible in the peak electron density and the peak density height derived from IRO measurements onboard CHAMP (Figure 3-28).

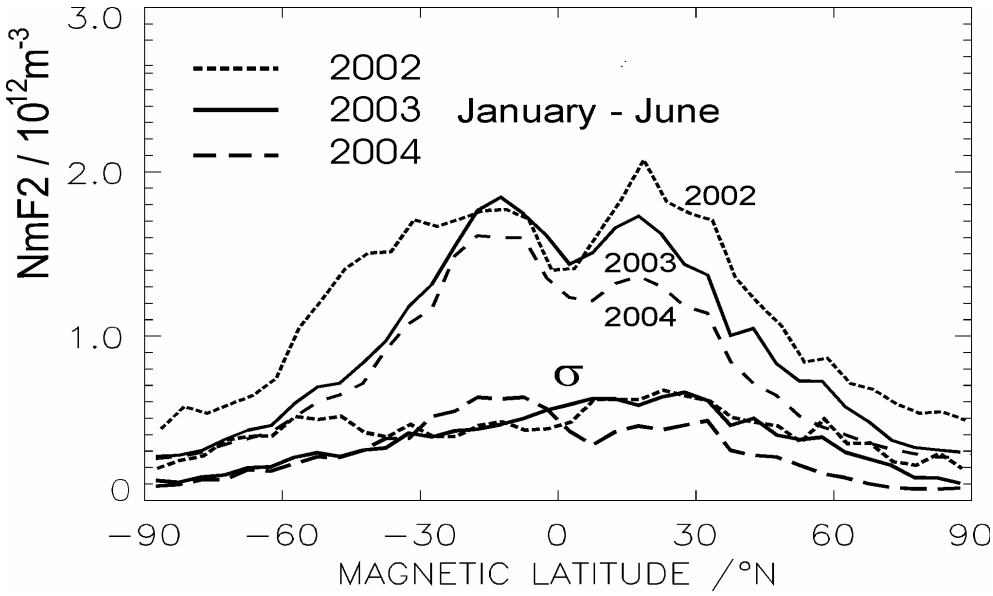

Figure 3-28: Latitudinal Dependency of the Day-Time (08:00-16:00 LT) F_2 Layer Peak Electron Density N_mF_2 as Seen in the CHAMP IRO Data at Three Years 2002-2004 for All Longitudes. The corresponding standard deviation σ is given at the bottom of the figure.

It is obvious that the photo ionization of the Earth's atmosphere due to solar radiation depends on the incidence angle of the irradiation. Thus, the latitudinal variation of the total ionization can easily be explained. Figure 3-28 shows that the F_2 layer ionization reduces up to 30 % at daytime from 2002 to 2004, when the average solar radio flux F10.7 cm decreases from about 180 down to 107 by about 40%. However, since the plasma motion is strongly influenced by magnetic und electric fields, the latitudinal dependence of the peak electron density demonstrates a more complex relationship with the solar activity. The well-known equatorial anomaly, characterized by enhanced ionization at about 15° at both sides of the geomagnetic equator is due to electric fields generated near the geomagnetic equator. The ionospheric plasma is uplifted at the geomagnetic equator via $\mathbf{E} \times \mathbf{B}$ drift and, while returning back, enhances the topside electron density at both sides of the geomagnetic equator, thus forming the so-called equatorial crest. This can nicely be seen also in the latitudinal dependence of the day-time peak density height h_mF_2 in Figure 3-29 where h_mF_2 reaches an absolute maximum of about 375 km near the geomagnetic equator. The northward shift of the maximum is due to seasonal effects because the northern summer hemisphere is stronger heated than the southern winter hemisphere.

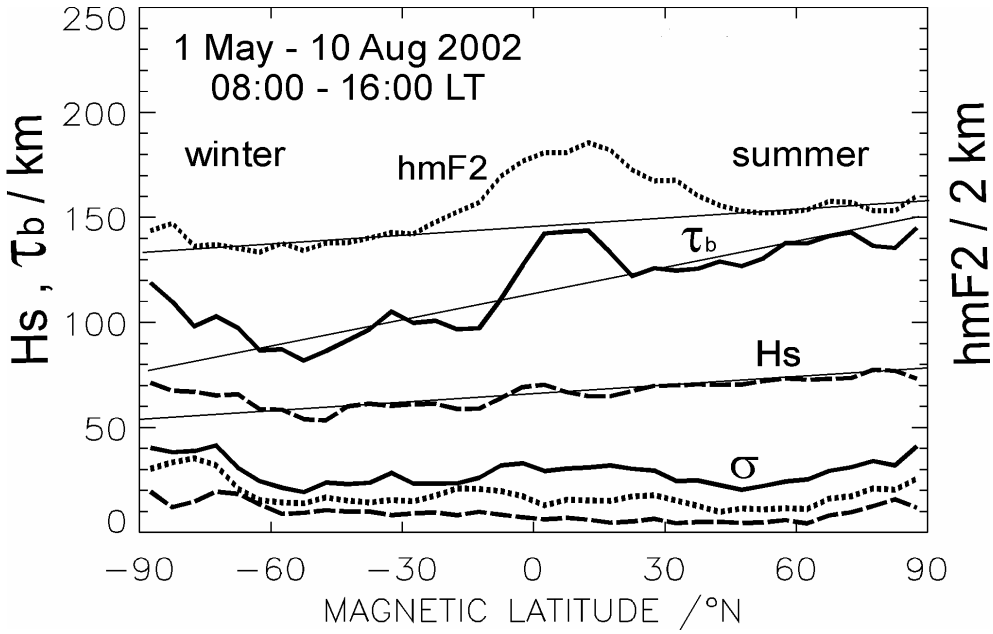

Figure 3-29: Latitudinal Dependence of the Peak Density Height h_mF_2 and Shape Parameters such as Bottomside Slab Thickness τ_b and the Topside Scale Height Hs at 425 km Height Measured at Daytime in Northern Summer. The corresponding standard deviation σ of all three parameters is given at the bottom of the figure.

Enhanced thermospheric heating during summer leads to an expansion of the thermospheric density distribution resulting in an increased peak density height and increased shape parameters slab thickness and topside scale height of the electron density profiles. This explanation is also confirmed when looking to the solar cycle dependence of these parameters showing biggest values at high solar activity conditions. If high latitudes > 65° are excluded, the general behavior indicates positive linear trends directed to the warmer summer hemisphere for h_mF_2, the scale height Hs and the bottomside equivalent slab thickness τb as well.

The following gradients may roughly be estimated: The peak density height h_mF_2 and scale height Hs grow up with about 280 m/deg and 140 m/deg, respectively, whereas the bottomside slab thickness grows up in the average by a rate of approximately 410 m/deg.

Compared with 2001, the peak density height decreases in average by about 75 km throughout all latitudes within in 2004.

The observed high latitude enhancement of all three parameters at the winter hemisphere is probably due to thermospheric heating as a consequence of particle precipitation and the action of the auroral electrojet. During night-time the polar ionosphere is separated from the mid-latitude ionosphere by the so-called trough region which is characterized by very low electron densities. As Figure 3-30 shows, IRO profiles reflect this phenomenon very well in their average plot.

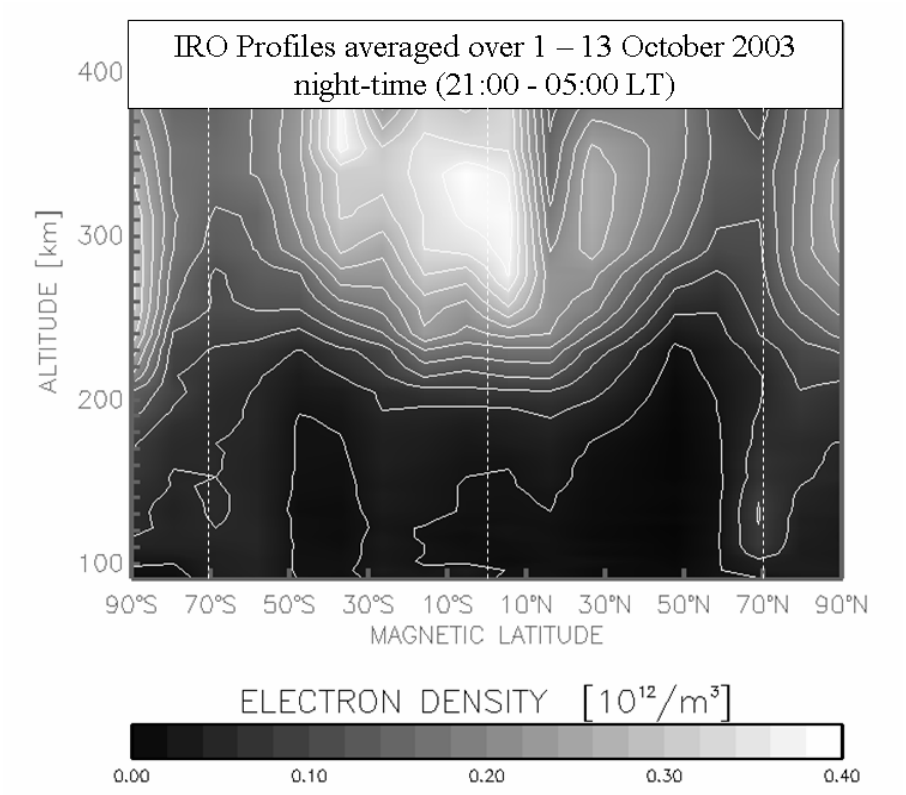

Figure 3-30: Imaging of the Average Vertical Ionization Structure Constructed from all IRO Profiles Obtained During the First 13 Days in October 2003 between 21:00 and 05:00 LT. Marked are geomagnetic latitudes at 70° and at 0°.

Although the limb sounding mode principally leads to a strong averaging of the observational data, the IRO measurements document the existence of numerous irregularities in the ionosphere (Tsybulya and Jakowski, 2005). As Figure 3-31 shows, relative irregularities of TEC with characteristic scale lengths of 15-30 km appear mainly in the nighttime sector. Here the irregularities occur just before sunrise with higher probability than near sunset. It has been shown that the disturbance pattern completely rotates with the terminator during a full day, underlining the strong relationship of the irregularity occurrence with the nighttime. Further studies are needed to explore the interaction of thermospheric conditions, e.g. atmospheric gravity waves, and related ionospheric effects well reflected in the plasma density, here measured by the relative total electron content variations along the occultation path (cf. Tsybulya and Jakowski, 2005).

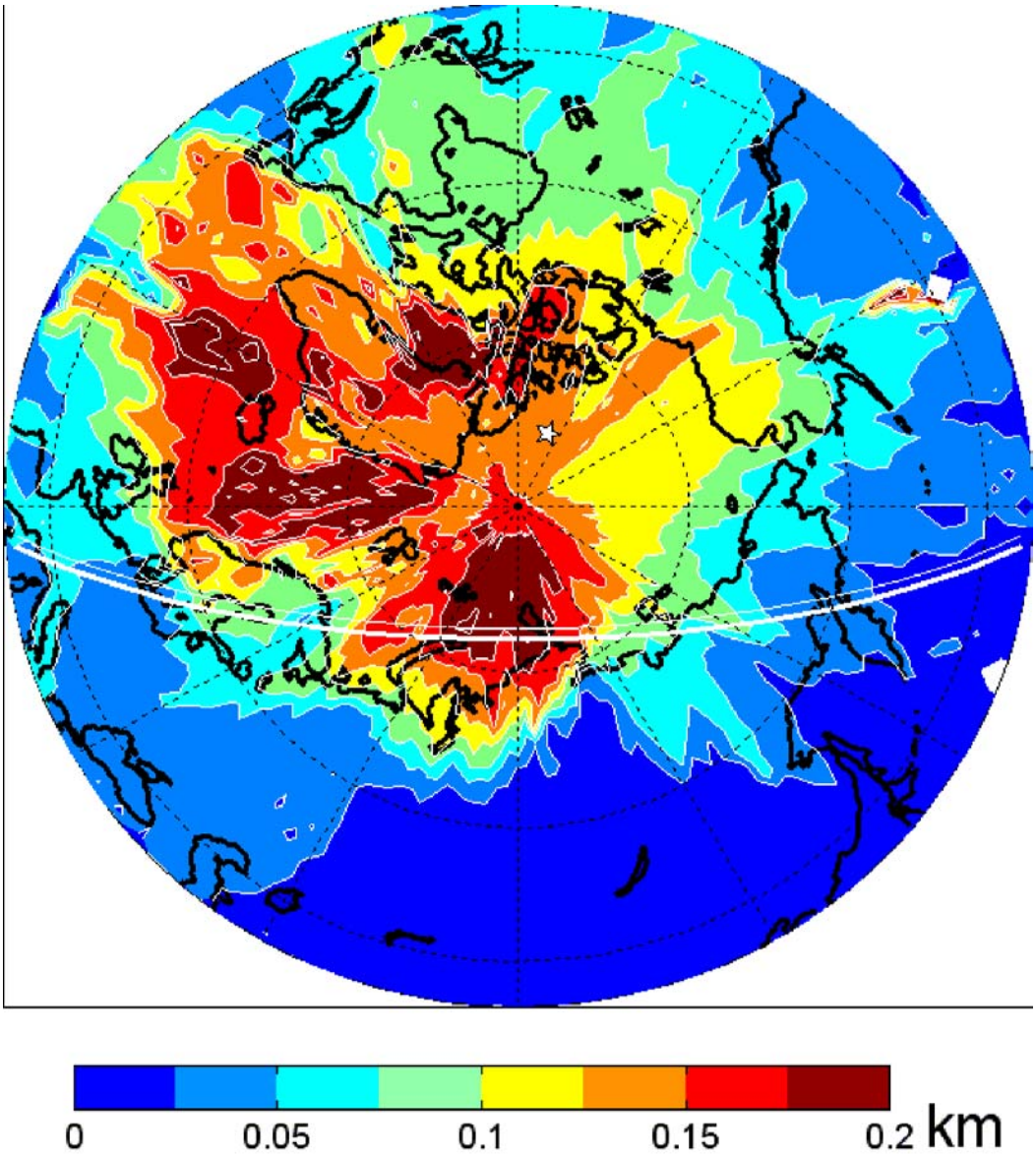

Figure 3-31: Distribution of Small Scale Irregularities of Relative TEC Measured by the IRO Technique Onboard CHAMP over the North Pole in the Winter Season (October 2003 – February 2004) Within the Time Interval 04:00-08:00 UT. The white lines mark the terminator (thick line towards the day time sector).

Severe space weather events modify the magnetosphere/ionosphere and thermosphere systems at quite different spatial and temporal scales. The zenith viewing GNSS measurements onboard CHAMP are well suited to monitor in particular large scale effects in time and space. Thus, storm induced changes of the ionospheric plasma developing at characteristic times of a few days and scale lengths of up to several thousand kilometers can be monitored effectively by analyzing the topside electron density reconstructions (e.g. Jakowski et al., 2005b).

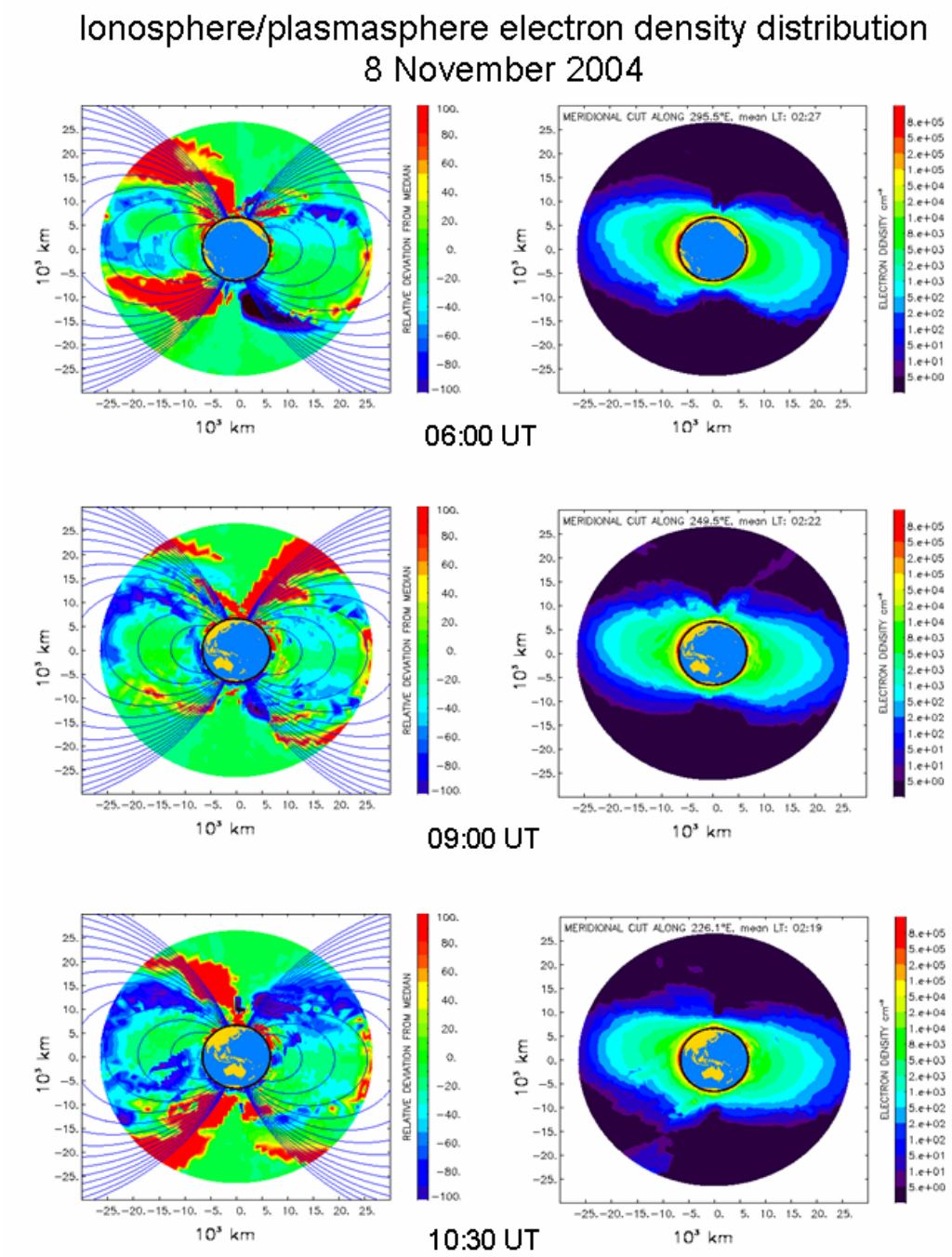

Figure 3-32: Comparison of Subsequent Reconstructions of the 3D Electron Density Structure in the CHAMP Orbit Plane during the Ionospheric Storm on 8 November 2004 in Comparison with Percentage Deviations from Corresponding Medians (Δn_e / n_e • 100%). Day-/night- sectors are on the left/right side of the figures.

During the storm on 7/8 November 2004 the electron density reconstructions in the CHAMP orbit plane indicate strong irregular behavior in particular close to the plasma pause region. The time period covered by the plots in Figure 3-32 corresponds with the time of Dst minimum value at 08:00 UT on November 8, 2004. Strong enhancements of the electron density are seen at high latitudes indicating plasma upflow in the auroral ionosphere at both hemispheres. Whereas such a plasma flow is more pronounced at the day-time polar zones at 6:00 UT and 10:30 UT, the outflow is focused at the Northern pole both at the day-

and night-time sectors around 9:00 UT. This observation agrees with the enhanced ion upflow at the polar cap boundary reported by Semeter et al. (2003) after analyzing incoherent scatter radar and IMAGE data. The cause of the upward ion velocities, which may exceed 800 m/s, remained uncertain in that study.

We are aware of the fact that the reconstructions are derived from a limited TEC data base and simplified assumptions. Nevertheless, the analysis of several storms indicates strong enhancements and also suppressions of the electron density. To avoid misinterpretation, we have counted only strong perturbation induced electron density deviations which exceed corresponding median values by 50% or are less than half of the median. The result, obtained for the storm on 20/21 November 2003, is shown in Figure 3-33.

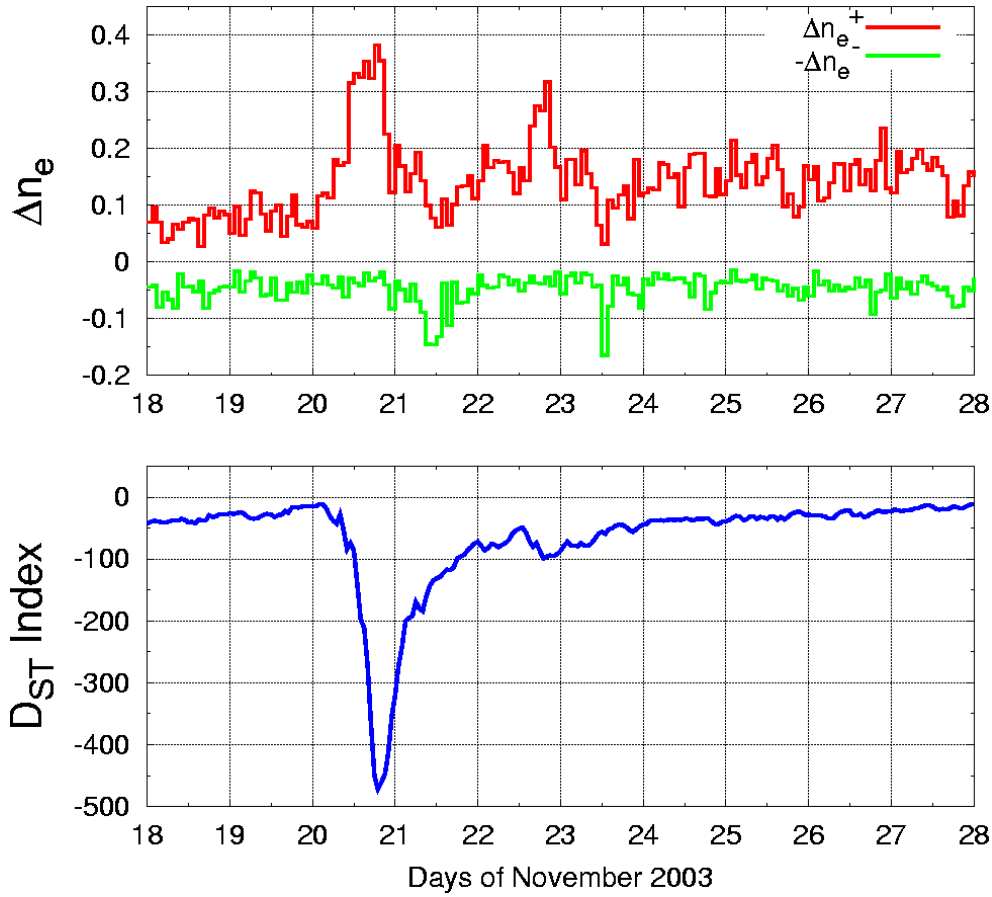

Figure 3-33: Comparison of Positive and Negative Deviation Counts of the Electron Density Values that Exceed a Certain Threshold Value ($|\Delta n_e| > 50\%$) from Corresponding Means with the Geomagnetic Dst Index (http://swdcdb.kugi.kyoto-u.ac.jp/dstdir/).

It is interesting to see that the topside ionosphere/plasmasphere considerably blows up in the growing phase of the storm whereas it reduces in the recovery phase. This behavior even repeats during a sub-storm starting around 12 UT on 22 November confirming the conclusion. Although we are aware of some remaining constraints of the reconstruction technique, e.g. due to incomplete data coverage, we believe that the basic observation results are correct.

Conclusions on the principal behavior of the plasmaspheric dynamics during geomagnetic storms are more reliable if several storms are superposed.

3.4.4 Summary and Conclusions

The large data base of IRO-derived electron density profiles and reconstructions of the topside ionosphere/plasmasphere electron density distribution is a valuable data source for the international scientific community studying ionospheric phenomena or investigation ionospheric impact on radio systems. The obtained space based GPS measurements contribute to a better understanding of solar-terrestrial relationships, and are valuable for developing and improving global ionospheric models such as IRI (e.g. Bilitza, 2003).

Due to the near-real-time processing of the satellite data the CHAMP satellite provides operational space weather information. To make this information available as fast as possible, DLR has established a permanent space weather service which provides both ground as well as space based GPS measurements and corresponding ionospheric data products.

Validation of IRO data has revealed that the F_2 layer peak electron density f_oF_2 and the corresponding height h_mF_2 agree quite well within 20% deviation. The standard deviation of vertical sounding derived electron density profiles is in the order of 1 MHz plasma frequency throughout the entire vertical IRO profile from 100-400 km height.

Although the good agreement between IRO measurement data and other types of independent measurements has proved the quality of the IRO retrieval technique, the validation process must continue because more knowledge is required in particular if the spherical symmetry assumption is violated. Further validation is also required for the topside reconstructions being capable imaging large scale structures of severe ionospheric perturbations.

To enhance the resolution of 3D reconstruction of the global ionospheric electron density distribution, space based GNSS sounding should be combined with ground based GNSS measurements.

The launch of new occultation satellites such as Formosat-3 / COSMIC (http://www.nspo.org.tw/2005e/projects/project3/hot.shtml) and in future also SWARM and TerraSAR-X offers great promise for establishing a huge data base well suited for modeling and monitoring the electron concentration in the near-Earth-space for scientific studies and continuous space weather monitoring.

3.4.5 Acknowledgements

This work has been financially supported by the German State Government of Mecklenburg-Vorpommern under Grant V230-630-08-TIFA-334. The authors are grateful to the international CHAMP team for maintaining the operation of the CHAMP satellite since 2000.

3.4.6 References

D. Bilitza, International Reference Ionosphere 2000: Examples of improvements and new features, Adv. Space Res. 31, #3, 757-767, 2003.

Bird, M.K., R. Dutta-Roy, S.W. Asmar, and T.A. Rebold, Detection of Titan's Ionosphere from Voyager 1 Radio Occultation Observations, ICARUS, 130, pp. 426-436, 1997.

Breus, T.K., K.Y. Pimenov, J.G. Luhmann, A. Krymsky, T. Hagfors, and W.I. Axford, Application of VIKING Radio Occultation Data to the Future Studies of the Martian Ionosphere, Adv. Space Res. , 22, No. 3, pp. 463-470, 1998.

Daniell, R.E, L.D. Brown, D.N. Anderson, M.W. Fox, P.H. Doherty, D.T. Decker, J.J. Sojka, R.W. Schunk, Parameterized ionospheric model: a global ionospheric parameterization based on first principles models. Radio Sci., 30, 1499-1510, 1995.

Escudero, A., A.C. Schlesier, A. Rius, A. Flores, F. Rubek, G.B. Larsen, S. Syndergard, and P. Hoeg, Ionospheric tomography using Oersted GPS measurements – Preliminary results, Physics and Chemistry of Earth, A26(3), pp. 173-176, 2001.

Fjeldbo, G.A., J. Kliore, and V.R. Eshleman, The neutral atmosphere of Venus as Studied with the Mariner V Radio Occultation Experiments, The Astronomical Journal, 76, 2, pp. 123-140, 1971.

Garcia-Fernandez, M., M. Hernandez-Pajares, J.M. Juan, J. Sanz, Improvement of ionospheric electron density estimation with GPSMET occultations using Abel inversion and VTEC information, J. Geophys. Res., 108(A9), 1338, doi: 10.1029/2003JA009952, 2003.

Hajj, G.A., L.J. Romans, Ionospheric electron density profiles obtained with the Global Positioning System: Results from the GPS/MET experiment, Radio Sci., 33(1), 175-190, 1998.

Heise, S., N. Jakowski, A. Wehrenpfennig, C. Reigber, H. Luehr, Sounding of the Topside Ionosphere/Plasmasphere Based on GPS Measurements from CHAMP: Initial Results, Geophysical Research Letters, 29, No. 14, 10.1029/2002GL014738, 2002.

Hocke, K. and K. Igarashi, Electron density in the F-region derived from GPS/MET radio occultation data and comparison with IRI, Earth Planets Space, 54, pp. 947-954, 2002.

Jakowski N. and H.-D. Bettac, Proposal for an ionosphere/plasmasphere monitoring system, Ann. Geophys. 12, 431-437, 1994.

Jakowski, N., B. Fichtelmann, and A. Jungstand, Solar activity control of ionospheric and thermospheric processes, J. Atmos. Terr. Phys., 53, 1125-1130, 1991.

Jakowski, N., TEC Monitoring by Using Satellite Positioning Systems, Modern Ionospheric Science, in H. Kohl, R. Rüster, K. Schlegel (eds.), *Modern Ionospheric Science*, EGS, Katlenburg-Lindau, ProduServ GmbH Verlagsservice, Berlin, pp. 371-390, 1996.

Jakowski, N., A. Wehrenpfennig, S. Heise, C. Reigber, H. Luehr, L. Grunwaldt, T. Meehan, GPS radio occultation measurements of the ionosphere from CHAMP: Early results. Geophys. Res. Lett. 29(10), doi: 10.1029/2001GL014364, 2002.

Jakowski, N., R. Leitinger, M. Angling, Radio Occultation technique for probing the ionosphere, Annals of Geophysics, 47(2/3), 1049-1066, 2004.

Jakowski, N., K. Tsybulya, J. Mielich, A. Belehaki, D. Altadill, J.C. Jodogne, B. Zolesi, Validation of GPS Ionospheric Radio Occultation results onboard CHAMP by Vertical Sounding Observations in Europe, in: C. Reigber, H. Luehr, P. Schwintzer, J. Wickert (Eds.): Earth Observation with CHAMP, Results from Three Years in Orbit, Springer, Berlin, 447-452, 2005a.

Jakowski, N., V. Wilken, S. Schlueter, S.M. Stankov, S. Heise, Ionospheric space weather effects monitored by simultaneous ground and space based GNSS signals, JASTP, 67, 1074-1084, 2005b.

Kliore, A.J., D.L. Cain, G.S. Levy et al., Occultation experiment: Results of the first direct measurement of Mars' atmosphere and ionosphere, Science, 149, pp. 1243-1248, 1965.

Kursinski, E.R., G.A. Hajj, J.T. Schofield, R.P. Linfield, and K.R. Hardy, Observing Earth's atmosphere with radio occultation measurements using the Global Positioning System, Journal of Geophysical Research, 102, D19, pp. 23429-23465, 1997.

Reigber, C., H. Luehr, P. Schwintzer, CHAMP mission status and perspectives, EOS Transactions - American Geophysical Union, 81 (Suppl. to No.48), F307, 2000.

Schreiner, W.S., S.V. Sokolovskiy, C. Rocken, Analysis and validation of GPS/MET radio occultation data in the ionosphere, Radio Sci., 34, 949-966, 1999.

Stankov, S.M. and N. Jakowski, Topside ionospheric scale height analysis and modeling based on radio occultation measurements, J. Atmos. Solar-Terr. Phys. 68, 134-162, 2006.

Semeter, J., C.J. Heinselman, J.P. Thayer, R.A. Doe, H.U. Frey, Ion upflow enhanced by drifting F-region plasma structure along the nightside polar cup boundary, Geophys. Res. Lett., 30, 22, 2139, doi:10.1029/ 2003/2003GL017747, 2003.

Tsybulya, K. and N. Jakowski, Medium- and small-scale ionospheric irregularities detected by GPS radio occultation method, Geophys. Res. Lett., 32, L09103, doi:10.1029/2005GL022420, 2005.

Ware, R., M. Exner, D. Feng, M. Gorbunov, K. Hardy, B. Herman, Y. Kuo, T. Meehan, W. Melbourne, C. Rocken, W. Schreiner, S. Sokolovskiy, F. Solheim, X. Zou, A.R. Anthes, S. Businger, and K. Trenberth, GPS soundings of the atmosphere from low earth orbit: Preliminary results, Bull. American Meteorological Society, 77, pp. 19-40, 1996.

Wehrenpfennig, A., N. Jakowski, J. Wickert, A dynamically configurable system for operational processing of Space Weather Data. Physics and Chemistry of the Earth (C), 26(8), 601-604, 2001.

Wilson, B.D., A.J. Mannucci, C.D. Edwards, Subdaily northern-hemisphere maps using an extensive network of GPS receivers, Radio Sci., 30, 639-648, 1995.

Yunck, T.P., F. Lindal, and C.H. Liu, The role of GPS in precise Earth observation, in IEEE PLANS '88 Position Location and Navigation Symposium Record – 'Navigation into the 21st Century', IEEE Cat. No.88CH2675-7, pp. 251-258, 1988.

3.5 BROAD BAND HF MONITORING

(Stefan Hawlitschka, FGAN Germany)

3.5.1 Introduction

Historically, the military use of the HF range was expected to decrease in favour of satcoms. But with the advent of communication techniques for large symbol rate transmissions in the HF range (NATO standard STANAG 4539) military communication via HF saw a renaissance. This trend was supported by the fact that communication via HF has further advantageous features such as independence from any relay medium other than the ionosphere, potential to establish long range data or voice transmission links at rather low cost and complexity etc. Because of the growing importance of new waveforms and communication systems which continuously adapt to the quality of the transmission path present-day signal scenarios in the HF range are so complex that it is indicated for the unauthorized user to intercept frequency bands of interest with broadband equipment.

At present first HF broadband systems with bandwidths up to 5 MHz – 6 MHz are being offered by the industry worldwide. These systems however are not generally appropriate to receive signals separately which overlap in frequency and time, a signal situation which often occurs in HF. Furthermore these systems are not able to estimate the bearing values of the individual signals, but only yield a rough estimate of the true bearing of the strongest of the overlapping signals, and no estimates of the weaker

signals. And even if it would be possible to determine bearing values of the individual signals bearing errors resulting from disturbances in the transmission medium ionosphere would remain.

The aim at FGAN is to find out whether the situation just described can be significantly enhanced by resorting to advanced hardware and algorithms for separate direction finding (DF) and reception of signals overlapping in time and frequency. In order to be able to test promising approaches an experimental broadband system for this purpose, called BRAHMS (**BR**oadband **A**utomatic **H**F **M**onitoring **S**ystem) had to be realized [1,2]. The underlying concept will be sketched in section 1.2. The focus will be on the smart antenna of BRAHMS and its ability to separate signals overlapping in time and frequency via spatial filtering. This ability will be demonstrated for a live HF signal scenario in section 1.2.3. It is shown in section 1.3 that Brahms estimates the incidence angles of the arriving HF-waves very precisely but that the angles of arrival do not necessarily match the true bearings. That is due to the fact that ionospheric disturbances such as ionospheric tilts and TIDs (**T**raveling **I**onospheric **D**isturbances) for example deviate the incident waves from great circle propagation. But vice versa, because the bearing values of HF-sources estimated by BRAHMS are highly affected by ionospheric irregularities, BRAHMS is an excellent tool for observing the ionosphere. Ionospheric effects onto the direction finding with BRAHMS will be shown. By analysing the deviations of the estimated bearings from the true ones by observation of known emitters such as radio stations or weather services, TIDs and other ionospheric irregularities could be detected. As a broadband system BRAHMS receives signals of many sources at once and by the combination of the bearings of many sources with known location a spatial survey of ionospheric “distortions” shall be generated. In this way dynamic processes like TIDs shall be tracked. Finally in section 1.4 a summary as well as an outlook on the future will be given. The outlook encompasses a coming development where the spatial survey and the tracking of plasmawaves shall be used to correct for the ionospherically induced DF errors.

3.5.2 Direction Finding in the HF Range

The DF error sources in HF may be divided into five major categories: Instrumental errors are due to imperfections concerning the used hardware such as amplifiers etc. Observational errors occur at the operator interface.. Site errors are for example due to reradiators and reflectors in the vicinity of the direction finder or discontinuities in the ground characteristic etc. These errors can be minimized by proper choice of the hardware components and scrupulous choice of the receiving site. Contrary to these ‘man made’ DF errors, those belonging to the remaining 2 categories are due to effects occurring on the propagation path. These errors can be divided into two categories, where one category comprises those DF errors which result from multipath propagation and/or intra channel interference, while the other category includes all errors, which result from ionospheric irregularities such as tilts and TIDs.

Particularly susceptible to DF errors due to interference of HF waves are conventional HF direction finders such as NADFs (**N**arrow **A**perture **D**irection **F**inders) which are based on standard DF principles. Such NADFs are ‘single-wave’ systems because they interpret an incident multicomponent wave field as a single component field. They yield one bearing value which tends towards the bearing value of the strongest wave field component. This approximate bearing may have a large bias. Our approach to solve the problem of DF errors due to multipath and/or intra channel interference consists in using ‘multi-wave’ direction finders. Required is a synchronous multi channel data processing chain consisting of an antenna array, each element being connected to one channel of synchronous signal processing. This enables one to resolve a multicomponent wave field into the single components and to calculate a bearing value for each component.

But even if the problem of DF errors in the HF range due to multipath propagation and/or intra channel interference can be solved by applying advanced DF principles, DF errors due to ionospheric irregularities are immune against such measures. Therefore we embark on a strategy to model the ionospheric irregularities by estimating bearing values for sources with known locations such as broadcast stations and

by comparing them to the true bearings. The idea is thus to gather information for the correction of propagation induced DF errors in the case of sources with unknown locations.

3.5.3 The Experimental Broadband System BRAHMS

At present BRAHMS is being realized as an offline system, to keep the hardware effort within limits and at the same time to preserve a high degree of flexibility. This however is by no means a restriction because for the evaluation of the approach suggested in section 1.1 to improve the bearing accuracy in HF, it doesn't matter whether the tests are performed online or offline.

3.5.3.1 Concept of BRAHMS

The concept of BRAHMS is shown in Figure 3-34. Contrary to off-the-shelf conventional broadband systems for HF monitoring, BRAHMS is equipped with a 10-element array antenna, whose 10 antenna output signals are processed separately. The signal coming from an antenna element passes through an analogue bandpass filter with a bandwidth between 4 MHz and 6 MHz. Then it is A/D (**A**nalogue/**D**igital) converted and stored on a pack of hard drives. From this disk pack the 10 signals can be simultaneously fed into 10 overlap-and-add analysis FFT (**F**ast **F**ourier **T**ransform) filterbanks [1], where the frequency band to be monitored is split up into a large number of narrowband frequency channels (the number of the frequency channels corresponds to the FFT length). For each channel with signal activity super-resolution direction finding together with segmentation is performed. That means that for each signal of interest centre frequency, bandwidth, power, duration and azimuth and elevation are determined. If necessary, with this information spatial filters can be calculated to filter out the single signals. If the bandwidth of a signal of interest is larger than the bandwidth of the FFT-channels, those analysis filterbank channels, which are occupied by the signal are identified and their outputs are joined together in a synthesis IFFT (**I**nverse **FFT**) filterbank [1]. That means that by the application of analysis/synthesis filterbanks in combination with spatial filters it becomes possible, to separately extract signals, overlapping in time and frequency, from the monitored frequency band and thus to make them available for further individual signal processing, a task which will not be gone into detail here. The super-resolution bearing values themselves furthermore serve the task of DF error correction, the principal topic focused on in this paper.

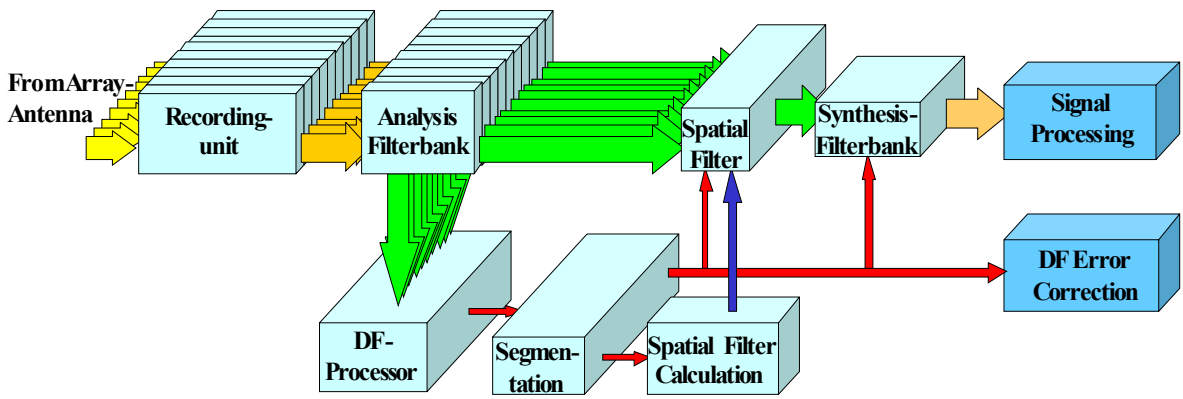

Figure 3-34: Block Diagram of BRAHMS.

At present BRAHMS can handle 2 frequency bands, one from 5,75 MHz to 10 MHz and the other from 9,085 MHz to 15,8 MHz. They have been chosen because they incorporate a number of broadcast bands and because it is our aim to use broadcast stations as calibration sources for the correction of propagation induced DF errors in the HF range. It is no problem however to add additional frequency bands by

adapting the software and by complementing the sets of analogue bandpass filters at the input of the recording unit by additional sets.

3.5.3.2 Smart Antenna of BRAHMS

The antenna elements of the 10-element array antenna are active monopoles, which are currently arranged as a double pentagon as depicted in Figure 3-35.

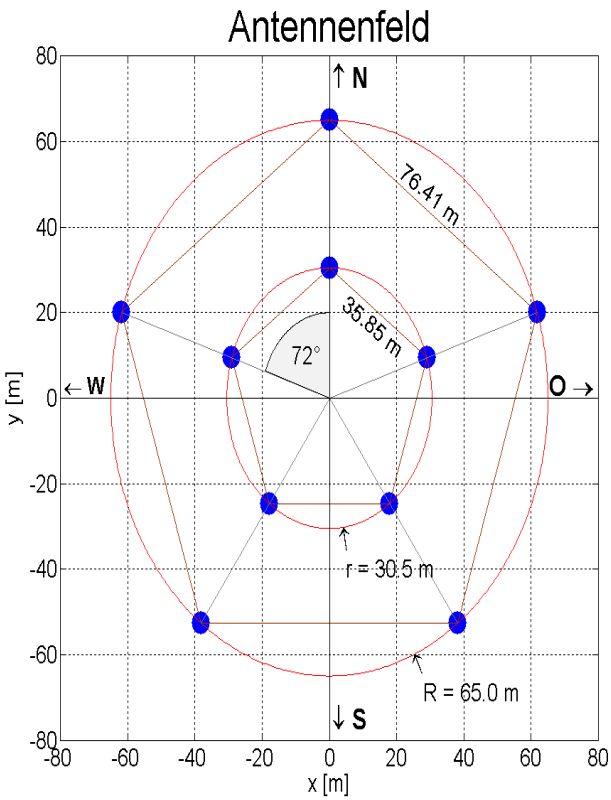

Figure 3-35: Optimized Array Geometry for Omni Directional Reception.

This geometry is optimized for omni directional reception in terms of maximum main lobe to side lobe ratio. In combination with super-resolution DF algorithms azimuth and elevation of the single components of the incoming wave field can be estimated. If a certain sector has to be reconnoitred, other array geometries such as a sparse V-shaped array geometry are preferable and if elevation is of no importance even ULAs (**U**niform **L**inear **A**rrays) may be a good choice, especially because this geometry has considerable advantages concerning the application of super-resolution DF algorithms.

Let's come back to the double pentagon array geometry. The dimensions of the array antenna shown in Figure 3-35 together with the properties of the broadband active monopoles allow to intercept HF frequency bands between 4 MHz and 15 MHz. As depicted in Figure 3-36, the beam width of the main lobe depends on the diameter of the double pentagon as well as on the frequency. As can be seen, the larger the frequency and the larger the diameter of the array, the smaller the beam width. The lower limit shown here for the beam width is the value from which on ambiguities for the array antenna arise. That means for example that a double pentagon with 10 antenna elements and a diameter of 130 m (red line) is limited to frequencies below about 15 MHz because of purely geometrical reasons.

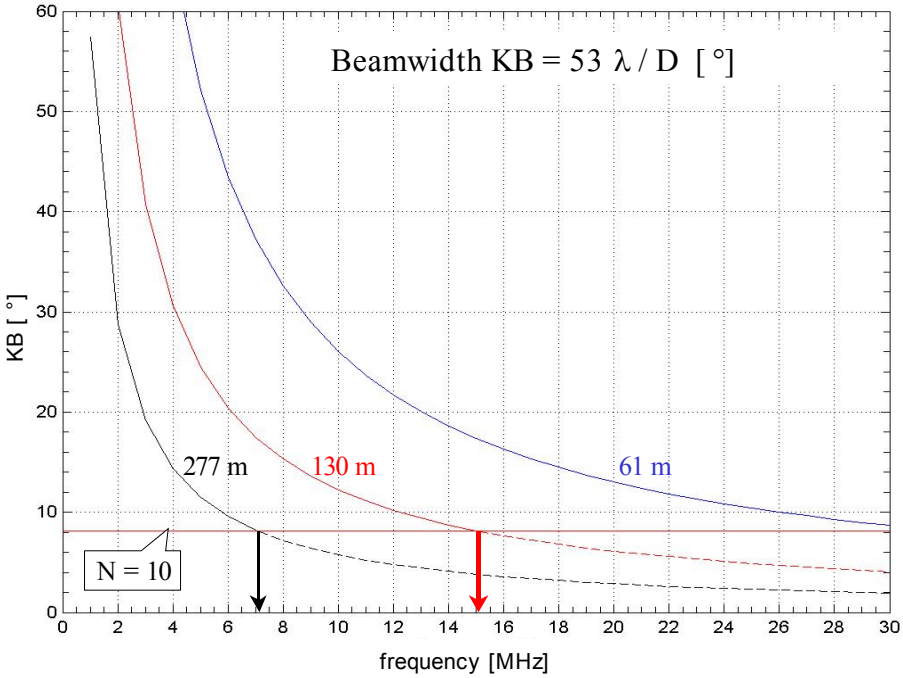

Figure 3-36: 3 dB-Beam Width versus Array Diameter and Frequency.

Next the different behaviour of conventional beamforming direction finding compared to super-resolution direction finding will be demonstrated. Figure 3-37 shows an AOA (Angle of Arrival) – diagram, where in radial direction we have the cosine of the elevation Φ, in circular direction the azimuth Θ.

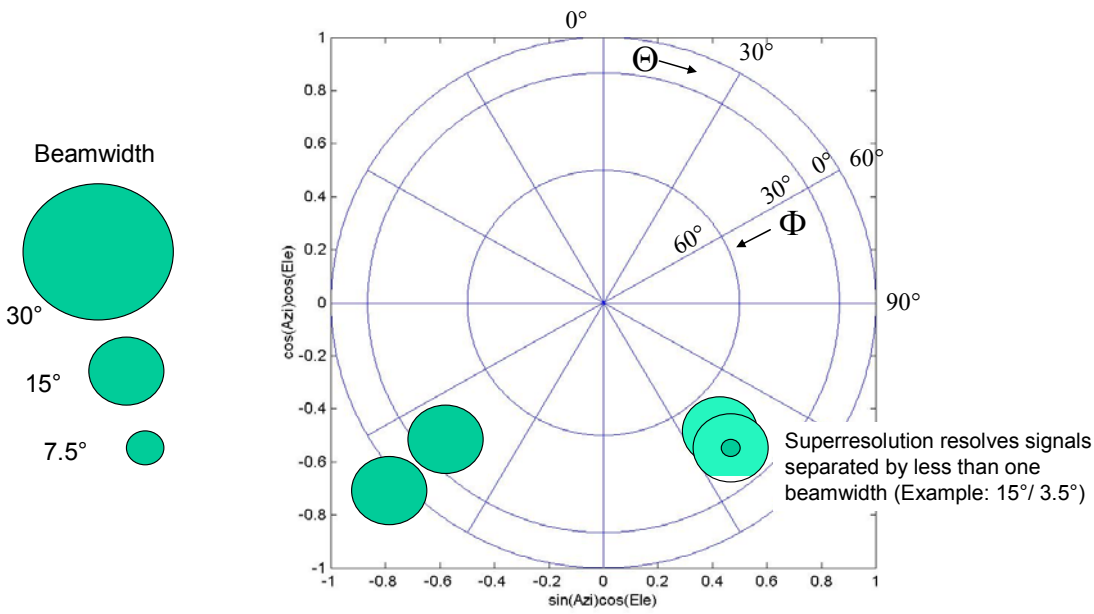

Figure 3-37: AOA (Angle-of-Arrival)-Diagram, Beam Width and Super-Resolution.

On the left side the dependence of the beam width of the main lobe on the frequency is shown: At a frequency of about 4 MHz the main lobe has a beam width of 30°, at a frequency of about 8 MHz a beam

width of 15° and at a frequency of about 16 MHz a beam width of 7.5°. Using conventional beamforming the resolution of the direction finder is about one beam width, with super-resolution and assuming a realistic HF-scenario it is about 20% of the beam width.

3.5.3.3 Algorithms

DF algorithms currently implemented on the processing unit of BRAHMS are:

- Conventional Beamforming;
- Capon or MVDR (**M**inimum **V**ariance **D**istortionless **R**esponse) [3];
- MUSIC (**M**ultiple **S**ignal **C**lassification) [4];
- Sequential MUSIC [5];
- ML (**M**aximum **L**ikelihood) [6]; and
- ML for moving sources [7].

The last one has been developed in order to take into account the ionospheric motion during the measurement interval of the AOA of an incoming HF wave. Beside these algorithms others exist which yield an analytic solution of the DF problem and for which the overall computational load is therefore much lower. Examples are:

- root-MUSIC [8]; and
- ESPRIT (**E**stimation of **S**ignal **P**arameters via **R**otational **I**nvariance **T**echniques) [9].

These algorithms have advantages over those of the first group but they presuppose certain array geometries such as ULAs for example. Therefore they are not implemented on BRAHMS at present. But BRAHMS is so flexible that it is no problem to complement its software accordingly if reasonable for example due to the use of array geometries other than the double pentagon.

Concerning the algorithms for spatial filtering, first a simple null-steering algorithm was implemented on BRAHMS. As the name suggests, this algorithm positions signals to be suppressed in nulls of the filter function. The null-steering algorithm needs bearing values to calculate the steering matrix **A** from the array manifold which is supposed to be known. Such an approach, however, requires a very good calibration of the array antennas. Furthermore the algorithm is very sensitive even to small changes of the AOAs, because the nulls of the filter are very sharp. Therefore, in a realistic HF scenario spatial filters based on the null-steering algorithm are of limited value.

Better suited is a time-frequency blind null-broadening algorithm developed at the department FE of FKIE [10]. Here also the steering matrix is used. This algorithm doesn't need either bearing estimates nor calibrated antenna arrays. It estimates the steering matrix from the output signals of the antenna array. The wave field components have to be partially non-overlapping either in frequency or time, a condition met by the HF live scenario shown on the left panel of Figure 3-38: Above estimates of the PSD (Power Spectral Density) for the time intervals [0 sec, 6 sec] and [6 sec, 8 sec] are shown in blue respectively green. Below a spectrogram of the scenario is shown. Based on the time-frequency null-broadening algorithm a spatial filter was calculated to extract the signal with the large bandwidth (green arrow) and to suppress the two others (black and blue arrows). The result is a spatial filter with broadened nulls for the robust suppression of the interfering signals which is immune against ionospherically induced slight AOA changes. Application of the null-broadening filter is depicted in Figure 3-38: The filter function is shown in the centre panel and the filtered signal on the right panel. It can be seen that the interferers are attenuated by 30-35 dB. At present work is in progress on a deterministic blind beamforming approach which even allows to separate completely overlapping signals [10].

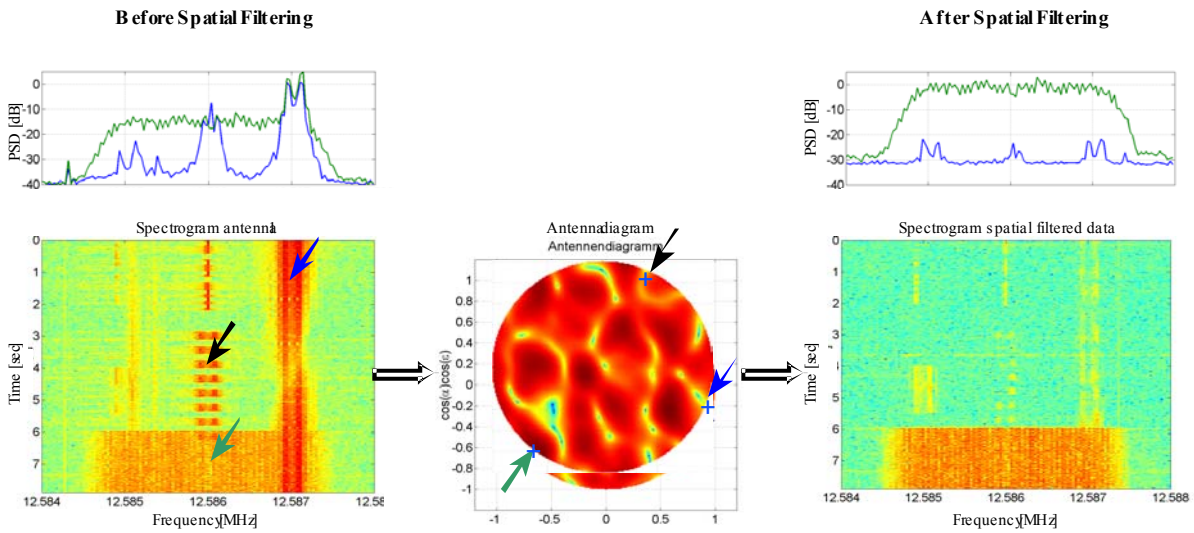

Figure 3-38: Filtering with Spatial Filter Based on Time Frequency Blind Null-Broadening.

3.5.4 Sensing the Ionosphere

So far we have presented an experimental system to obtain precise estimates of bearing angles of HF-waves onto the array antenna. By analysing the time series of the bearing angles of many emitters, information about the *actual* state of the ionosphere can be retrieved. Thus the different sources and their propagation modes (reflection on different layers) have to be separated. The approach is shown in Figure 3-39 and Figure 3-40 or an example from a live scenario. Assignment of the incidence angles of sequential measurements to a certain source and propagation mode is done by building a histogram (Figure 3-39) in the so called *u,v* plane (*u*=sin(azimuth)*cos(elevation) *v*=cos(azimuth)*cos(elevation)) which is segmented by applying a watershed transformation [11,12]. The result of the segmentation is shown in Figure 3-40. The different sources and their propagation modes can then be analysed individually. Limited performance may be given when the elevation angles of the two propagation modes of a single source tend to overlap. This can be minimized by reducing the sampling time down to 10 min for a histogram and it has proven to work correctly on our data. Each segment is given a number and the estimated directions are assigned to the respective segment. Then a new histogram is being sampled and segmented. The new segments, whose areas in the histogram may differ slightly are assigned to the existing ones or if a new source or mode has been detected, a new number is given. In this way data of up to three days duration have been processed.

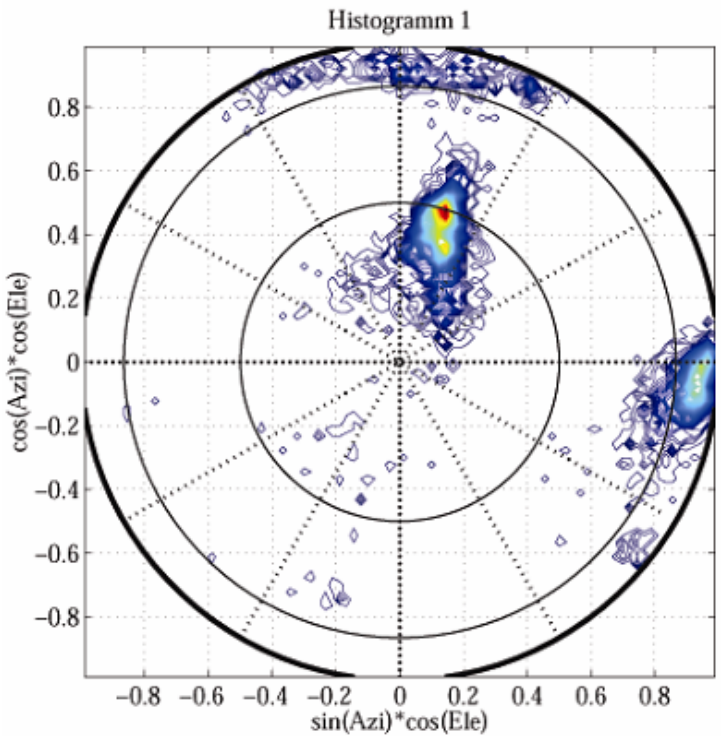

Figure 3-39: Histogram of Several Minutes of a Recording of two Main Sources, DLF Berlin with a True Bearing of 19.3° from Greding near Nuremberg and a Second Unknown Station with a True Bearing of Approximately 90°. DLF Berlin shows two peaks indicating two way propagation.

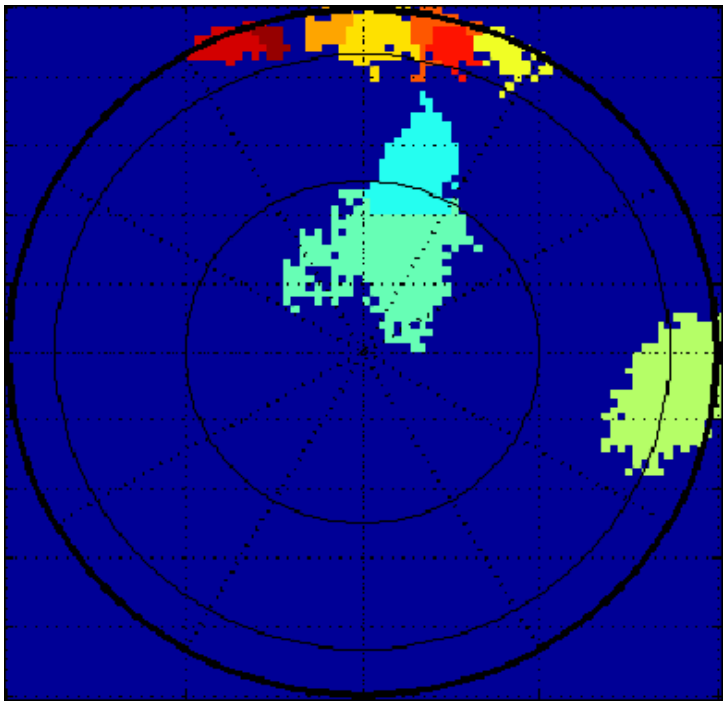

Figure 3-40: Segmentation of the Histogram of Figure 3-39. The two peaks of DLF Berlin are assigned to different segments and will be analysed separately. Also the unknown station with 90° bearing is assigned to an own segment as well as the signals coming from northerly directions.

As example a recording from the evening of 14th to the morning of 15th May 2002 is chosen which suffers from high impact of the ionosphere onto the bearing angles. In Figure 3-41 the time series of the estimated bearing angle of a transmission from the radio station DLF at Berlin is shown. It exhibits two different characteristics, being different before 23 h local summer time and after. We begin the analysis with the evening and early night part of the recording until 23 h. From 19 h to 21 h the passage of traveling wave packages (TWP) [13] can be seen. They consist of a MSTID with several periods. At 21:30 a LSTID passes through the "reflection point" of the HF wave. The corresponding first part of the signal has been segmented as one mode. The second one starts at 23 h and exhibits about 10 degrees higher elevation angles. The reason can be seen on the ionograms from Juliusruh (Figure 3-42). From 23.00 h (21:00 h UT) on spread F occurs accompanied by a second stratification 100 km above. The spread F causes higher spread of the bearing angles of the HF wave passing through it. There may still exist some LSTID action covered by the scattering in the spread F layer.

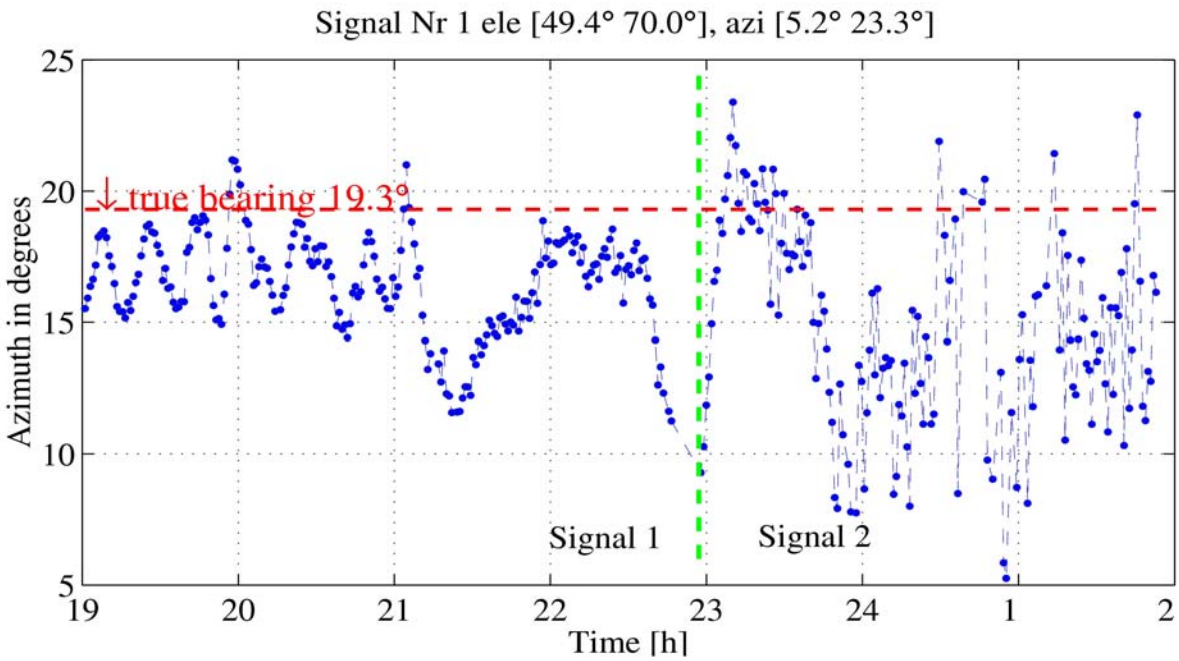

Figure 3-41: Temporal Profile of the Azimuth from the Evening into the Night. F-Region reflection of DLF Berlin on 6.005 kHz 14.05.02. The diagram is composed of Signal 1 (left of the green line) and Signal 2 (right of the green line) which has larger elevation angles. All times are local summer time (UT+2).

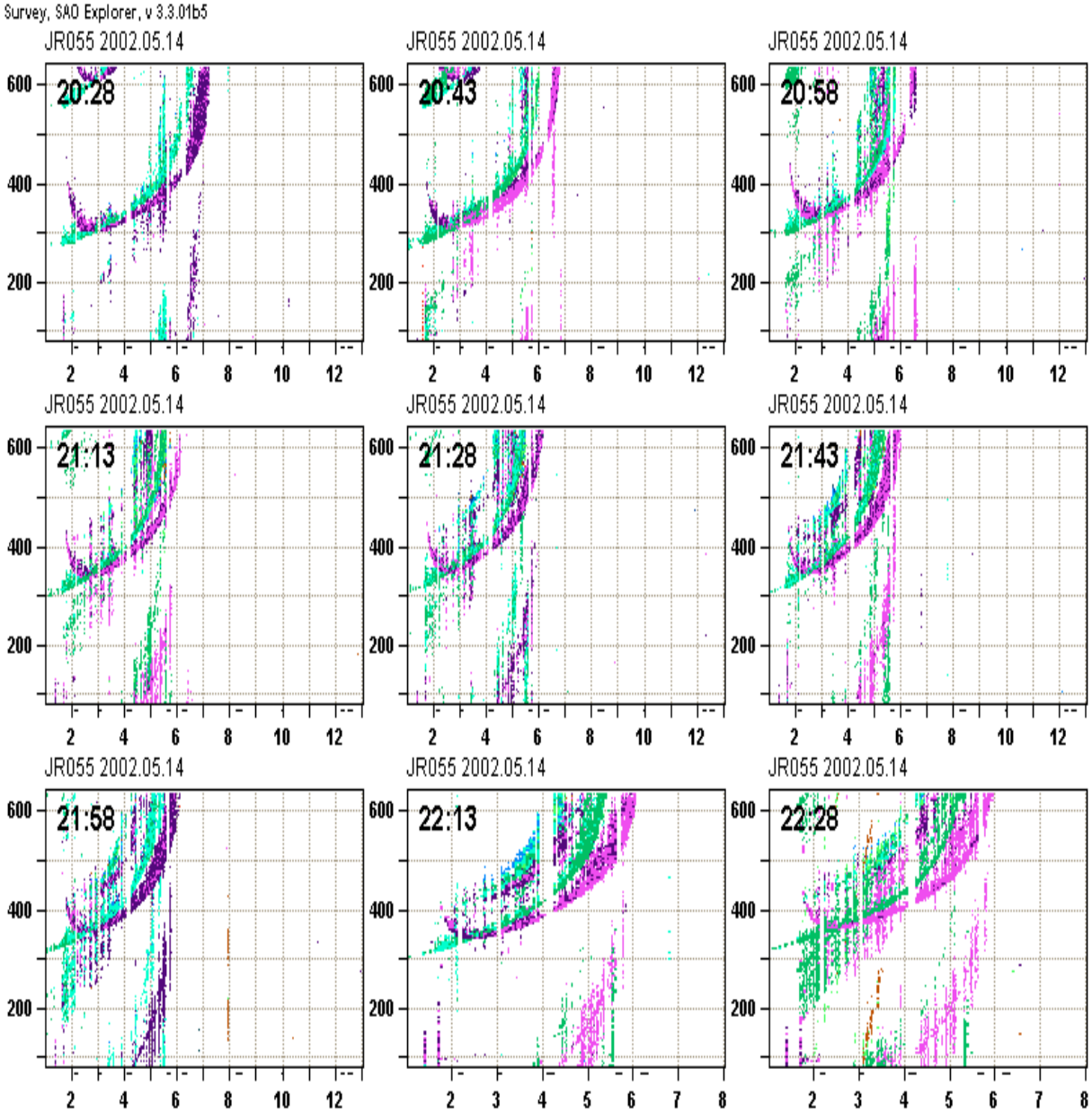

Figure 3-42: Ionograms from the Station Juliusruh / Germany for the Evening of 14.05.02. All times are UT. Shown are traces of the ordinary wave (green) and extraordinary wave (magenta).

On the next morning no more spread in the F-region propagation is detected, but TID action can be recognized (Figure 3-43). Additionally there exists a second propagation mode enabled by reflection on the E-layer (Figure 3-44). Again these two modes have been discriminated because of different elevation angles. In Figure 3-45 the mean absolute bias (blue) and the standard deviation (red) around the (biased) mean value of the data of Figure 3-44 are shown. Thanks to appropriate signal processing the spread around the mean value is quite small. The standard deviation is as in most cases smaller than the bias.

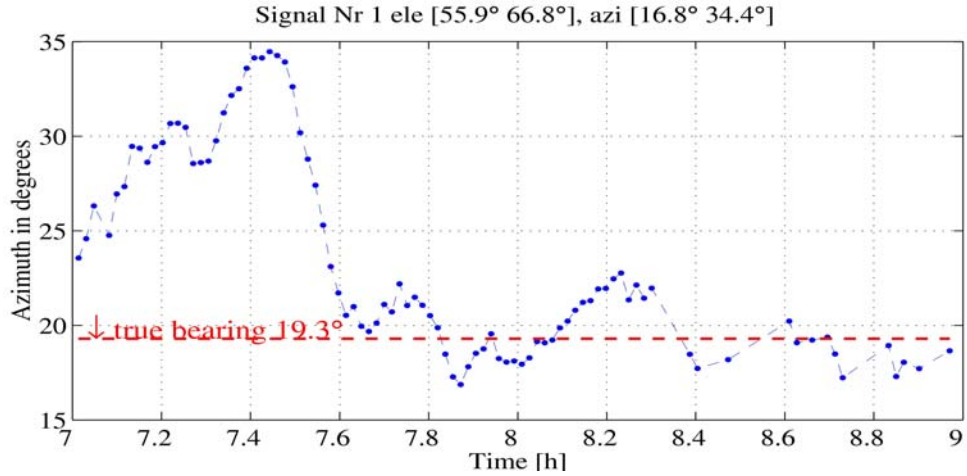

Figure 3-43: F-Region Bearing Angles on the Morning of 15.05.02 for DLF Berlin.

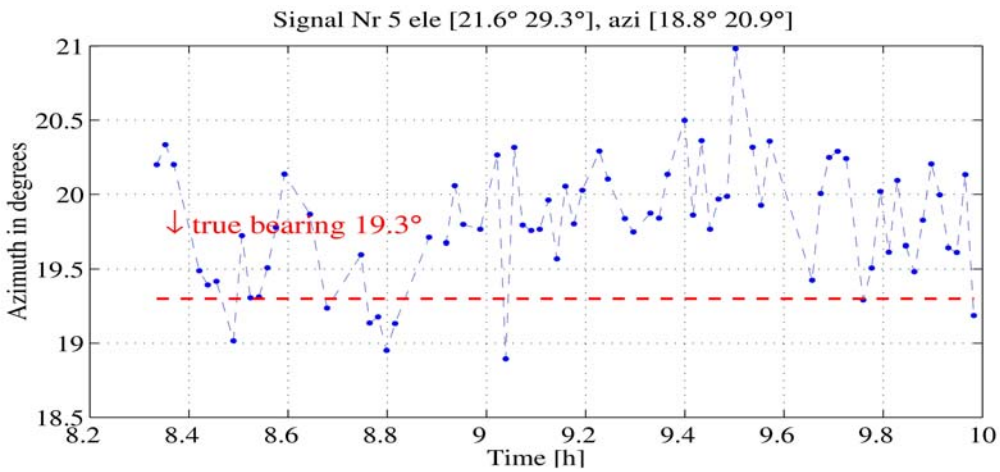

Figure 3-44: E-Region Bearing Angles on the Morning of 15.05.02 for DLF Berlin.

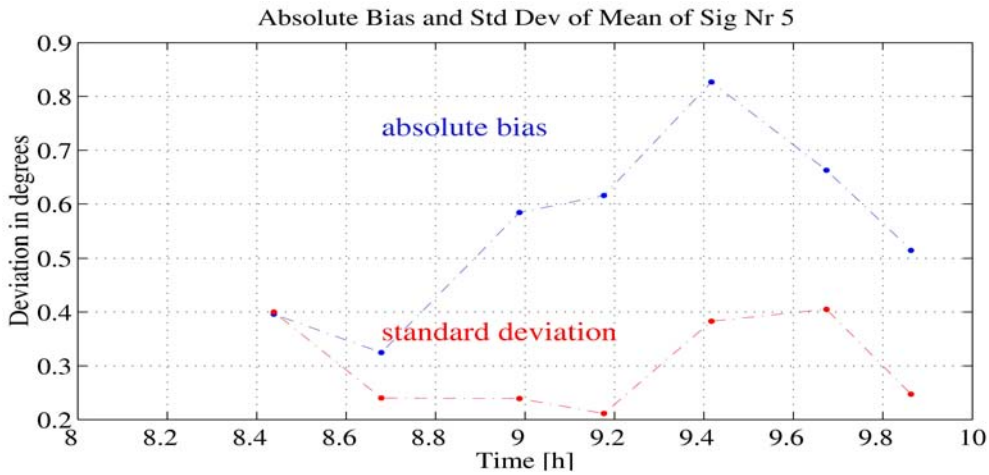

Figure 3-45: Mean Absolute Deviation (Absolute Bias) Each with 10 Samples and Standard Deviation Around the (Biased) Mean Value of the Data of Figure 3-44.

3.5.5 Summary and Outlook

The experimental system BRAHMS and its technical properties as well as its advantages for surveillance of HF have been described. It is a system for simultaneous and continuous surveillance of 4 or 6 MHz bandwidth. Unique are essentially two topics: Separate direction finding and reception of signals overlapping in time and frequency. This has been successfully demonstrated for HF signals from live scenarios.

Another highlight shall consist in a correction of DF estimation errors. As shown the short term errors have already considerably been reduced through the development of MLMS direction finding algorithms. The reduced spread of bearing angles is an indispensable prerequisite for a successful correction of the remaining DF errors. The long term DF deviations are mainly ionospherically induced. To cope with them a correction method is under development which shall be based on the actual measurement of the ionospheric state by the analysis of ionospheric irregularities as shown in Section 1.3. Many scientific analyses have been performed to characterise their effect onto DF [14,15]. Beley et al. [16] have developed a geometrical and a statistical approach to reconstruct the parameters of a TID. A similar formalism could be chosen to "translate" the deviations of the estimated bearings from the true bearings of emitters with known location, mainly from the radio bands into the shape of the ionospheric irregularities. By observation of many radio stations an image of the "undulations" of the ionosphere shall be constructed. The aim is to use this image and the knowledge about its development to correct the bearing angles of unknown sources, which have to be reconnoitred.

3.5.6 References

[1] Hißen, H. & Baum, D. (2004). *Automatische Breitbanderfassung mit intelligenten Antennen im Kurzwellenbereich*. FKIE-Report No. 75.

[2] Baum, D. & Foerster, W. (2006). *BRAHMS – Ein breitbandiges automatisches HF-Monitoring-System*. FKIE-Report to be published.

[3] Capon, J. (1969). *High-Resolution Frequency-Wavenumber Spectrum Analysis*. Proc. IEEE., vol. 57, pp. 1408-1418.

[4] Schmidt, R.O. (1986). *Multiple Emitter Location and Signal Parameter Estimation*. IEEE Trans. AP, vol. 34, pp. 276-280.

[5] Oh, S.K. & Un, C.K. (1993). *A Sequential Estimation Approach for Performance Improvement of Eigenstructure based Methods in Array Processing*. IEEE Trans. SP, vol. 41, pp. 457-463.

[6] Ksienski, A.A. & McGhee, R.B. (1968). *A Decision Theoretic Approach to the Angular Resolution and Parameter Estimation Problem for Multiple Targets*. IEEE Trans. AES, vol. 4, pp. 443-455.

[7] Baum, D., Foerster, W. Hawlitschka. S. (2007): *BRAHMS Broadband Automatic HF-Monitoring System*, RTO IST-056 / RSM002 Symposium on Characterising the Ionosphere, 12-16 June 2006, Fairbanks USA.

[8] Barabell, A.J. (1983). *Improving the Resolution Performance of Eigenstructure based DF Algorithms.* Proc. ICASSP, pp. 336-339.

[9] Paulraj, A., Roy, R. & Kailath, T. (1986). *A Subspace Rotation Approach to Signal Parameter Estimation*. Proc. IEEE, vol. 74, pp. 1044-1045.

[10] Demissie, B. (2006). *Verfahren zur Raumfilterung für das Breitbanderfassungssystem BRAHMS*. FKIE-Report to be published.

[11] Vincent, L. & Soille, P. (1991): *Watersheds in Digital Spaces: An Efficient Algorithm Based on Immersion Simulations.* IEEE Trans. PAMI, vol. 13, pp. 583-598.

[12] Najman, L. & Schmitt, M. (1996): *Geodesic Saliency of Watershed Contours and Hierarchical Segmentation.* IEEE Trans. PAMI, vol. 18, pp. 1163-1173.

[13] Afraimovich, E.L., N.P. Perevalova and S.V. Voyeikov (2003): *Traveling wave packages of total electron content disturbances as deduced from global GPS network data*. JASTP 65, 1245-1262.

[14] Hawlitschka, S. (2006): *TIDs and Tides observed by a super-resolution Direction Finding System.* JASTP 68, 568-577.

[15] Hawlitschka, S. (2007): *Plasmawaves observed by a super-resolution DF system*. RTO IST-056 / RSM002 Symposium on Characterising the Ionosphere, 12-16 June 2006, Fairbanks USA.

[16] Beley V. S., Galushko, V. G., Yampolski, Y., M. (1995): *Traveling ionospheric disturbance diagnostics using HF signal trajectory parameter variations*. Radio Science, Vol. 30, 1739-1752.